

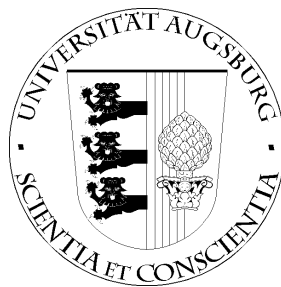
Synthesis, properties and applications
of $AB(O,N)_3$ oxynitride perovskites

Dissertation
zur Erlangung des Doktorgrades
der mathematisch-naturwissenschaftlichen Fakultät der
Universität Augsburg

vorgelegt von

Rosiana Aguiar

Augsburg, Oktober 2008



Erstgutachter: Prof. Dr. Armin Reller
Zweitgutachter: Prof. Dr. Achim Wixforth

Tag der mündlichen Prüfung: 5. Dezember 2008

Index

Abstract	5
Zusammenfassung	7
1. Introduction	9
2. Experimental Methods	17
2.1 X-ray Diffraction (XRD).....	18
2.2 Neutron Diffraction (ND).....	20
2.3 Rietveld Refinement	21
2.4 UV-vis Spectroscopy.....	23
2.5 Colorimetry.....	25
2.6 Specific Surface Area by N ₂ Physisorption (BET)	26
2.7 O/N Analysis.....	27
2.7.1 Hot Gas Extraction.....	28
2.7.2 Secondary Ion Mass Spectrometry (SIMS).....	28
2.7.3 Elastic Recoil Detection Analysis (ERDA).....	30
2.8 Thermogravimetry (TG) and Mass Spectrometry (MS).....	31
2.9 Atomic Force Microscopy (AFM).....	33
2.10 Electron Microscopy (EM).....	33
2.10.1 Scanning Electron Microscopy (SEM).....	34
2.10.2 Transmission Electron Microscopy (TEM).....	36
3. Syntheses, Crystal Structure and Morphology of Polycrystalline Oxynitride Perovskites	39
3.1 Ammonolysis.....	39
3.1.1 Conventional Ammonolysis.....	39
3.1.2 Microwave Induced Ammonia Plasma Nitridation.....	40
3.2 Synthesis Methods for Polycrystalline Oxide Precursors.....	46
3.2.1 Solid-State Reaction.....	46
3.2.2 Pechini Synthesis.....	48
3.2.3 Spray Pyrolysis.....	50
3.2.4 Polyol Assisted Coprecipitation.....	52
4. Oxynitride Perovskites as Pigments	57

5. Thermal Oxidation of Selected Oxynitride Perovskites.....	67
6. The system $\text{La}_x\text{Sr}_{(1-x)}\text{Ti}(\text{O},\text{N})_3$	81
6.1 Polycrystalline Samples: Crystal Structure Refinement.....	81
6.2 Thin films.....	87
7. Oxynitride Perovskite as Photocatalysts.....	103
7.1 Decomposition of Methylene Blue in Aqueous Solution.....	108
7.2 H_2 and O_2 Evolution from Aqueous Solutions	111
7.3 Gas Phase Decomposition of Acetone.....	115
8. Thick Oxynitride Perovskite Layers.....	127
9. Summary and Outlook.....	145
Acknowledgments.....	149
List of publications.....	153
Curriculum vitae.....	157

Abstract

Perovskites are a highly interesting class of materials. Their physical and chemical properties can be tailored by varying the cationic/anionic stoichiometries. While cationic substitutions have been intensively studied, substitutions in the anionic sublattice are by far less well examined. This work describes the different synthesis routes to prepare oxynitride perovskites of the general composition $AB(O,N)_3$ with $A = \text{Ca, Ba, Sr, La, Nd}$ and $B = \text{Ti, Nb, Ta}$, as well as their properties and possible applications. The oxynitrides were either obtained directly from mixtures of binary oxides/carbonates or from complex perovskite-related oxides of composition $ABO_{3.5}$ or ABO_4 . The oxide precursors were prepared as polycrystalline samples by different synthesis techniques such as solid-state reaction, Pechini method, spray pyrolysis and polyol assisted coprecipitation. Thin films of these oxides were deposited by spin coating and pulsed laser ablation. Single crystals have been obtained using a floating zone furnace with radiation heating. The corresponding oxynitrides were synthesized by reaction with ammonia gas at high temperatures, commonly denoted as ammonolysis, in conventional tube furnaces or by a microwave induced ammonia plasma. The compositions, crystal structures and the physical properties of the samples were analyzed by a variety of different techniques such as x-ray and neutron diffraction, atomic force microscopy, transmission and scanning electron microscopy, O/N hot gas extraction, secondary ion mass spectrometry, thermogravimetry and mass spectrometry, UV-vis spectroscopy, etc. The introduction of nitrogen in the oxide lattice results in a reduction of the band gap, because N^{3-} is less electronegative than O^{2-} . As a consequence the oxynitride compounds start to absorb light in the visible range. The possibility to use the samples as non-toxic pigments and photocatalysts have been studied. The thermal stability of the oxynitride samples under different oxygen concentrations was also analyzed. Finally, the physical properties of the oxynitride single crystalline layers prepared by ammonolysis of oxide crystal slices were investigated. The oxynitride layers presented electrical conductivity ca. 5 orders of magnitude higher than the corresponding oxide slices. It was verified that the oxynitride perovskites could be in the near future used as environmental friendly pigments, substituting some toxic dyes that contain heavy metals. The samples also

showed significant photocatalytic efficiency for the decomposition of organic molecules and for evolution of H₂ and O₂ from aqueous solutions.

Zusammenfassung

Perowskite stellen eine hoch interessante Materialklasse dar. Ihre physikalischen und chemischen Eigenschaften können mit der Variation der kationischen/anionischen Stöchiometrie maßgeschneidert werden. Während kationische Substitutionen sehr intensiv untersucht worden sind, sind Substitutionen im anionischen Untergitter sehr viel weniger erforscht. Diese Arbeit beschreibt die verschiedenen Synthesemethoden um Oxidnitride des Typs $AB(O,N)_3$ mit $A = Ca, Ba, Sr, La, Nd$ und $B = Ti, Nb, Ta$ herzustellen, darüberhinaus ihre Eigenschaften und mögliche Anwendungen. Die Oxidnitride wurden entweder direkt aus Mischungen von binären Oxiden/Karbonaten oder mit aufwendigen Perowskit-verwandten Oxiden der Zusammensetzung $ABO_{3,5}$ oder ABO_4 gewonnen. Die Ausgangsperowskite des Typs $ABO_{3,5}$ wurden als polykristalline Materialien mit verschiedenen Synthesemethoden wie der Festkörpersynthese, der Pechini-Methode, der Spraypyrolyse und Polyol unterstützten Fällungsreaktionen hergestellt. Dünne Filme wurden mit Spin-Coating und Pulsed Laser Deposition erzeugt. Oxidische Einkristalle konnten mittels eines optischen Zonenschmelzverfahrens gewonnen werden. Die entsprechenden Oxidnitride wurden durch eine Reaktion mit gasförmigem Ammoniak bei hohen Temperaturen, der sogenannten Ammonolyse, in handelsüblichen Röhrenöfen oder mit einem Mikrowellen-Ammoniakplasma hergestellt. Die Stöchiometrien, Kristallstrukturen und physikalischen Eigenschaften der Proben wurden mit verschiedenen Methoden wie Röntgen- und Neutronendiffraktion, Rasterkraftmikroskopie, Transmissions- und Rasterelektronenmikroskopie, Thermogravimetrie verbunden mit Massenspektrometrie, UV-vis Spektroskopie und mehr bestimmt. Die Stickstoff-Substitution in das Oxidgitter bewirkt eine Verkleinerung der Bandlücke, da das N^{3-} Ion weniger elektronegativer als das O^{2-} Ion ist. Als Konsequenz absorbieren die Oxidnitride schon im sichtbaren Wellenlängenbereich des Lichtes. Außerdem wurden die Möglichkeiten zum Einsatz der Proben als ungiftige Pigmente und zur Fotokatalyse untersucht. Dazu wurde auch die thermische Stabilität der Oxidnitride bei unterschiedlichen Sauerstoffkonzentrationen analysiert. Schließlich wurden die physikalischen Eigenschaften einkristalliner Oxidnitrid-Schichten, die durch Ammonolyse von Kristallscheibchen hergestellt werden, betrachtet. Dabei erwies es sich, dass die

Oxidnitrid Schichten eine um etwa fünf Größenordnungen höhere elektrische Leitfähigkeit besitzen, als entsprechende Oxidschichten. Es konnte zudem gezeigt werden, dass die Oxidnitride in naher Zukunft als umweltverträgliche Pigmente, als Ersatz für einige giftige Farben, die Schwermetalle enthalten, zum Einsatz kommen könnten. Außerdem besitzen die Proben für die Zersetzung von organischen Molekülen und die Entwicklung von H_2 und O_2 aus wässrigen Lösungen eine deutliche photokatalytische Effizienz.

1. Introduction

The family of Perovskites can be represented by the composition ABX_3 . A denotes a relatively large cation of usually low charge, such as rare earth, alkaline earth or alkali metal, while the smaller B cations are normally transition metals. X is most often a simple anion as oxide or fluoride. The ideal cubic perovskite structure can be exemplified by $SrTiO_3$ (space group $Pm\bar{3}m$), with $\mathbf{a} = \mathbf{b} = \mathbf{c} = 3.905 \text{ \AA}$ and $\alpha = \beta = \gamma = 90^\circ$, as shown in Figure 1.1a. The oxygen ions are positioned on the middle of each edge of the cubic cell. The Ti cations are located on each corner and are 6-fold coordinated by oxygen, forming TiO_6 octahedra (Fig. 1.1b), Sr is placed at the center of the unit cell and is 12-fold coordinated by O, forming a SrO_{12} cuboctahedron (Fig. 1.1c).

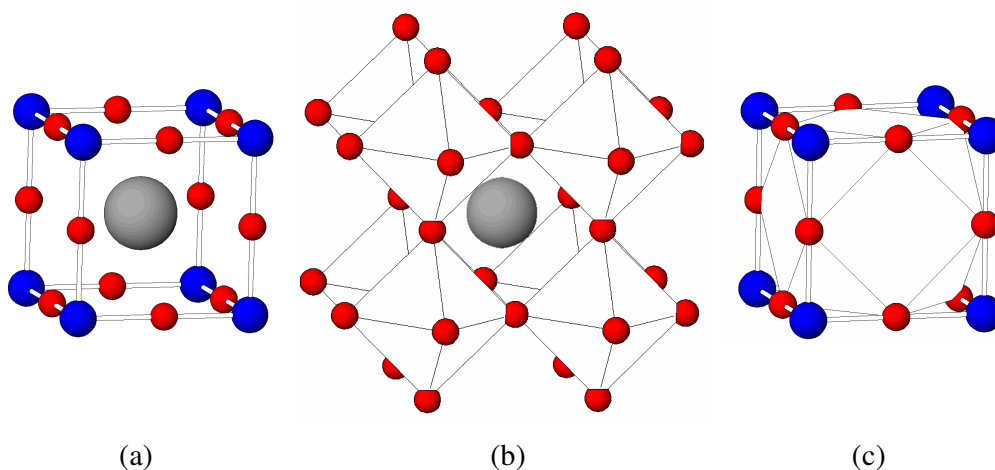


Figure 1.1: Cubic unit cell of $SrTiO_3$. Sr: gray big spheres, Ti: blue medium size spheres, O: red small spheres. (The radii of the cations do not correspond to their real sizes)

The perovskite structure can support a large variety of cations on the A and B positions. Around 90% of the natural metallic elements of the Periodic Table are known to be stable in a perovskite type oxide structure. This structure configuration also opens the possibility to synthesize multicomponent perovskites by partial substitution of cations on the A and B positions, giving rise to solid solutions with the general formula of $A_{1-x}A'_xB_{1-y}B'_yX_3$ [1]. Because of this flexibility to accommodate such a wide variety of ions in their structure, perovskites have extensive variable physical and chemical properties. As example, $(Ba,Sr)TiO_3$ and $Pb(Zr,Ti)O_3$ exhibit outstanding dielectric properties and are suited for capacitor applications, particularly

decoupling and tunable microwave capacitors [2]. $(\text{La,Sr})(\text{Ga,Mg})\text{O}_3$ is used as electrolyte of solid oxide fuel cells (SOFC) because of its oxide ion conductivity [3]. LaCoO_3 and $\text{LaMnO}_{3+\delta}$ have catalytical properties and are able to decompose chlorinated volatile organic compounds. These substances are the main pollutants in the low atmosphere of the cities and responsible for the destruction of the ozone layer in the stratosphere [4]. $\text{YBa}_2\text{Cu}_3\text{O}_{7-\delta}$ (YBCO) has an oxygen deficient perovskite structure and was the first material to become superconducting above 77 K, the boiling point of nitrogen [5]. LaMnO_3 has attracted attention because of its interesting magnetic properties [6]. This list of examples could easily be extended but it is not the objective of this thesis.

One of the pre-requisites to synthesize solid state solutions and to avoid phase separation in the perovskite structures is the Goldschmidt tolerance factor [$t = (r_A + r_X) / \sqrt{2}(r_B + r_X)$, where r_A , r_B , and r_X are the ionic radii of the A, B-type cations and X-anions, respectively] that should vary between 0.75 and 1.05. For values different from unity, structural distortions are observed, resulting from two different mechanisms [7]:

1. Cation displacements within the octahedra, as in the tetragonal dielectric BaTiO_3 with $t = 0.986$ at room temperature [8, 9].
2. Tilting of the octahedra, as in the orthorhombic CaTiO_3 and CdTiO_3 that have $t = 0.986$ and 0.978 respectively [10].

These structural distortions result in a lower symmetry than the ideal cubic unit cell. The corresponding compounds can have tetragonal, orthorhombic, monoclinic or triclinic structures depending on the deviation from unit of the tolerance factor.

There exist a large variety of layered perovskite-related structures, composed of BO_6 corner-sharing octahedra. As example are the well-known Ruddlesden-Popper phases $\text{A}_{m+1}\text{B}_m\text{O}_{3m+1}$. The thickness of the layers rises with m. Lichtenberg *et al* extensively examined the crystallographic structure of the oxide perovskites studied in this thesis [11]. These oxides are represented by the composition $\text{A}_n\text{B}_n\text{O}_{3n+2}$, and is only found for $B = \text{Ti, Nb or Ta}$. For both series m and n is the octahedra thick of the layers and when $m = n = \infty$ the simple cubic perovskite ABO_3 is formed. The difference between the Ruddlesden-Popper and the perovskite related $\text{A}_n\text{B}_n\text{O}_{3n+2}$ is the arrangement of the corner-shared BO_6 octahedra within the layers and the cationic ratio A/B . Figure 1.2 illustrates three of the $\text{A}_n\text{B}_n\text{O}_{3n+2}$ layered structures with $n = 2, 5$

and ∞ . Possible values for n and some examples of perovskite-related compositions ABO_x with variable oxygen content x are described in Table 1.1.

While cationic substitutions have been thoroughly studied for many years, substitutions in the anionic perovskite sublattice are by far less examined. There are some reports on carbides [12-14], halides [15-17] and nitrides, such as the paramagnetic perovskite type γ' -(Fe_{1-x}Ni_x)₄N [18], the semiconductor TaThN₃ [19], the metallic anti-perovskites Mn₃BN ($B = \text{Ga, Zn}$) [20] and Ca₃MN ($M = \text{P, As, Sb, Bi, Ge, Sn, Pb}$) [21] and the negative thermal expansive Ge-doped Mn₃AN ($A = \text{Cu, Zn, Ga}$) [22].

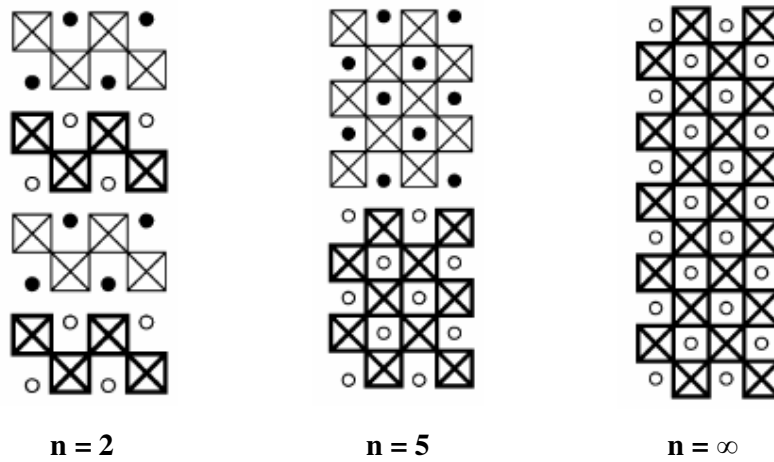


Figure 1.2: $A_nB_nO_{3n+2}$ Perovskite-related structures with octahedral layers $n = 2, 5$ and ∞ [11].

Table 1.1: Examples of perovskite-related ABO_x and respective n values.

Structure $A_nB_nO_{3n+2}$	n	ABO_x	Examples
ABO_3	∞	$x = 3.00$	SrNbO ₃ [23], LaTiO ₃ [24]
$A_6B_6O_{20}$	6	$x = 3.33$	La _{0.67} Ca _{0.33} TiO _{3.33} [25], CaNb _{0.67} Ti _{0.33} O _{3.33} [26]
$A_5B_5O_{17}$	5	$x = 3.40$	SrNbO _{3.41} [27], CaNbO _{3.4} [28], LaTiO _{3.40} [29]
$A_{4.5}B_{4.5}O_{15.5}$	4.5	$x = 3.44$	LaTiO _{3.44} [25], SrNbO _{3.45} [30], CaNbO _{3.44} [28]
$A_{4.33}B_{4.33}O_{15}$	4.33	$x = 3.47$	LaTiO _{3.47} [30], NdTiO _{3.47} [31]
$A_4B_4O_{14}$	4	$x = 3.50$	LaTiO _{3.5} , NdTiO _{3.5} [32], CaNbO _{3.5} [30]
$A_3B_3O_{11}$	3	$x = 3.67$	Ca _{0.67} La _{0.33} NbO _{3.67} [11], LaTi _{0.67} Nb _{0.33} O _{3.67} [30]
$A_2B_2O_8$	2	$x = 4.00$	LaTaO ₄ [33]

The focus of this thesis is on a special field of anionic substitution, namely the partial replacement of oxygen by nitrogen, leading to the perovskite oxynitrides. Nitrogen is an appropriate candidate for replacing oxygen in ternary oxides because both anions have close electronic configurations and ionic radii [34]. When O^{2-} is substituted for N^{3-} in ternary oxides three possible mechanisms can compensate the additional negative charge of the nitride ion to give charge neutrality in the specific systems:

1. Change of the oxidation state of the *B*-site cation e.g. $LaV^{3+}O_3 \rightarrow LaV^{3+/4+}(O,N)_3$ [35].
2. Simultaneous *A*- and/or *B*- site substitution with cations of higher valence (cross-substitution) e.g. $Sr^{2+}TiO_3 \rightarrow La^{3+}_xSr^{2+}_{1-x}TiO_{3-x}N_x$ [36] or $CaZrO_3 \rightarrow CaZr^{4+}_{1-x}Ta^{5+}_xO_{3-x}N_x$ [37].
3. Reduction of the number of anions as in $LaTiO_{3.5} \rightarrow LaTiO_2N$ or $SrTaO_{3.5} \rightarrow SrTaO_2N$ [38].

These possibilities of charge compensation can be accompanied by changes in the crystallographic and electronic structure of the comprising materials. For example the ammonolysis of the layered perovskite-related oxide $Sr_2Nb_2O_7$, which possesses a (pseudo-) 2D structure (octahedra thick of the layers, $n = 4$), leads to the 3D perovskite-type oxynitride $SrNbO_2N$ ($n = \infty$) [39].

The oxynitride perovskites can present diverse symmetries, depending on the deviations from the cubic unit cell. Different factors can influence the distortions in the structures, such as the Goldschmidt tolerance factor deviation, cationic/anionic ordering and structural tensions due to non-ideal ionic packing. Table 1.2 gives some examples of perovskite oxynitride structures.

The electronic structure of the oxynitrides is influenced by the nitrogen 2p-orbitals that have higher energy than the ones from oxygen. In general, the band structure of the formed oxynitrides is similar to the respective perovskite type oxides: the top of the valence band is represented by the 2p-orbitals of the anions and the bottom of the conduction band is formed by the d-orbitals of the transition metals. Despite of this general similarity, the incorporation of N^{3-} results in a pronounced change of the energy of the frontier orbitals. Since the 2p-orbitals of nitrogen have a higher energy than the 2p-orbitals of oxygen, nitrogen insertion into the oxygen sublattice is leading to a band gap reduction. As an example the ab initio calculations for $BaTaO_2N$ are shown in Figure 1.3.

Table 1.2: Different symmetries of oxynitride perovskites.

Structure	Space Group	Parameters*	Example
Cubic	$P m \bar{3} m$	$\mathbf{a} = \mathbf{b} = \mathbf{c},$ $\alpha = \beta = \gamma = 90^\circ$	BaTaO ₂ N [40]
Tetragonal	$I 4 / m c m$	$\mathbf{a} = \mathbf{b} \neq \mathbf{c},$ $\alpha = \beta = \gamma = 90^\circ$	SrNbO ₂ N [39]
Orthorhombic	$P n m a$	$\mathbf{a} \neq \mathbf{b} \neq \mathbf{c},$ $\alpha = \beta = \gamma = 90^\circ$	NdTiO ₂ N, LaZrO ₂ N [41]
Monoclinic	$C 2 / m$	$\mathbf{a} \neq \mathbf{b} \neq \mathbf{c},$ $\alpha = \gamma = 90^\circ, \beta \neq 120^\circ$	LaTaON ₂ [42]
Triclinic	$\bar{1}$	$\mathbf{a} \neq \mathbf{b} \neq \mathbf{c},$ $\alpha \neq \beta \neq \gamma \neq 90^\circ$	LaTiO ₂ N [41]

* not the necessary conditions, but the general cases.

The upper part of the valence band is dominated by N 2p-states while the O 2p-states are mainly in the lower part. The bottom of conduction band is dominated by Ta 5d states. With the shrinking of the band gap, the oxynitrides of transition metal with d^0 electronic configuration start to absorb light in the visible range and in turn many of them show bright colors. This intrinsic property of the oxynitride perovskite makes them good candidates to be employed as electrical conductor, environmental friendly pigments [43, 44] and photocatalysts [45, 46]. These properties will be discussed in Chapters 4 and 7.

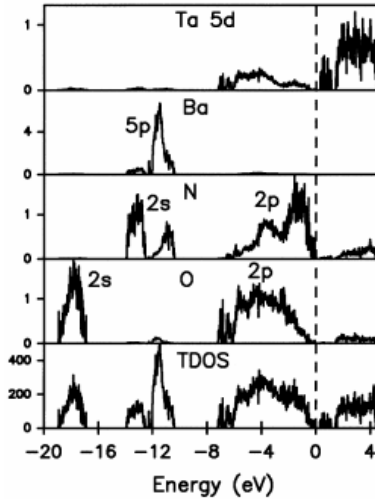


Figure 1.3: Partial and total density of states for BaTaO₂N assuming O and N randomly distributed in the structure. The unit of Y-axis is states/(eV unit cell) [47].

This thesis is divided in nine chapters. Chapter 2 describes the analysis techniques used to characterize the oxide/oxynitride perovskite samples. Chapter 3 explains the methods to synthesize the polycrystalline precursor oxides and the furnace set-ups used to ammonolyse the oxide perovskites. The morphological differences between samples synthesized by different techniques are discussed. Chapter 4 reports on how the oxynitride perovskites could be applied as non-toxic pigments and how their color can be tailored by cationic/anionic substitutions. Chapter 5 describes the thermal oxidation of the oxynitrides under different oxygen concentrations. In Chapter 6 the crystallographic structure refinement of the series $\text{Sr}_{1-x}\text{La}_x\text{Ti}(\text{O},\text{N})_3$ is given. The oxynitride compounds were also grown as thin layers by spin coating and pulsed laser deposition. The physical properties of the films prepared by the two techniques were compared. Chapter 6 reports about the photocatalytic efficiency of the oxynitride samples. Three different set-ups were used. First, the decomposition of methylene blue in aqueous solutions was investigated. Second, water splitting in H_2 and O_2 was examined and finally the gas phase decomposition of acetone was studied. Chapter 8 is a discussion about the structural, optical and electrical properties of the oxynitride single crystalline layers, obtained by ammonolysis of the respective oxide single crystals grown by floating zone technique. As a final point Chapter 9 is a summary associating properties, morphologies and applications of oxynitride perovskites. Some out look were also given including possible experiments using the oxynitride samples.

References

- [1] M. A. Pena, J. L. G. Fierro, *Chem. Rev.* 101 (2001) 1981.
- [2] D. Dimos, C. H. Mueller, *Annu. Rev. Mater. Sci.* 28 (1998) 397.
- [3] T. Ishihara, T. Shibayama, H. Nishiguchi, Y. Takita, *J. Mat. Sci.* 36 (2001) 1125.
- [4] G. Sinquin, C. Petit, J. P. Hindermann, A. Kiennemann, *Catalysis Today* 70 (2001) 183.
- [5] B. G. Hyde, J. G. Thompson, R. L. Whitlers, J. G. Fitzgerald, A. M. Stewart, J. S. Anderson, J. Bitmead, M. S. Paterson, *Nature* 327 (1987) 402.
- [6] G. Matsumoto, *J. Phys. Soc. Japan* 29 (1970) 606.
- [7] P. M. Woodward, *Acta Crystallogr. B* 53 (1997) 32.
- [8] W. F. A. Su, *Mat. Chem. Phys.* 62 (2000) 18.
- [9] G. Arlt, D. Hennings, G. de With, *J. Appl. Phys.* 58 (1985) 1619.
- [10] S. Sasaki, T. C. Prewitt, J. D. Bass, *Acta Cryst. C* 43 (1987) 1668.
- [11] F. Lichtenberg, A. Herrnberger, K. Wiedenmann, J. Mannhart, *Prog. Solid State Chem.* 29 (2001) 1.
- [12] S. Mollah, *J. Phys. : Condens. Matter* 16 (2004) P1237–P1276.
- [13] T. M. Gesing, K. H. Wachtmann, W. Jeitschko, *Z. Naturforsch. B* 52 (1997) 176.

- [14] C. Greaves, Slater C.R., *Phys. C.* 175 (1991) 172.
- [15] J. O. Rubio, *J. Phys. Chem. Solids* 52 (1991) 101.
- [16] O. T. Antonyak, A. S. Voloshinovskii, E. N. Mel'chakov, S. Mikhailik, M. S. Pidzrailo, I. V. Stefanskii, P. A. Rodnyi, *Opt. Spektrosk.* 84 (1998) 861.
- [17] R. L. Narayan, S. V. Suryanarayana, *Mater. Lett.* 11 (1991) 305.
- [18] X. G. Diao, A. Y. Takeuchi, F. Garcia, R. B. Scorzelli, H. R. Rechenberg, *J. Appl. Phys.* 85 (1999) 4485.
- [19] N. E. Brese, S. J. DiSalvo, *J. Solid State Chem.* 120 (1995) 378.
- [20] J. García, J. Bartolomé, D. González, *J. Chem. Thermodyn.* 15 (1983) 1041.
- [21] M. Y. Chern, D. A. Vennos, S. J. DiSalvo, *J. Solid State Chem.* 96 (1992) 425 .
- [22] K. Takenaka, H. Takagi, *Appl. Phys. Lett.* 87 (2005) Art. No. 261902.
- [23] D. Ridgley, R. Ward, *J. Am. Chem. Soc.* 77 (1955) 6132.
- [24] M. Kerstigian, R. Ward, *J. Am. Chem. Soc.* 77 (1955) 6199.
- [25] O.S. Becker, PhD Thesis, Universität Augsburg, Germany (2000).
- [26] M. Nanot, F. Queyroux, J. C. Gilles, *J. Solid State Chem.* 28 (1979) 137.
- [27] S. C. Abrahams, H. W. Schmalke, T. Williams, A. Reller, F. Lichtenberg, D. Widmer, J. G. Bednorz, R. Spreiter, Ch. Bosshard, P. Günter, *Acta Crystallogr. B* 54 (2008) 399.
- [28] M. Hervieu, F. Studer, B. Raveau, *J. Solid State Chem.* 22 (2008) 273.
- [29] F. Lichtenberg, T. Williams, A. Reller, D. Widmer, J. G. Bednorz, *Z. Phys. B: Condens. Matter* 84 (1991) 369.
- [30] T. Williams, F. Lichtenberg, D. Widmer, J. G. Bednorz, A. Reller, *J. Solid State Chem.* 103 (1993) 375.
- [31] J. G. Bednorz, *Physica C* 282 (1997) 37.
- [32] J. Galy, A. Carpy, *Phil. Mag.* 29 (1974) 1207.
- [33] R. J. Cava, R. S. Roth, *J. Solid State Chem.* 36 (1981) 139.
- [34] R. D. Shannon, C. T. Prewitt, *Acta Crystallogr. B* 25 (1969) 925.
- [35] P. Antoine, R. Assabaa, P. L'Haridon, R. Marchand, Y. Laurent, *Mater. Sci. Eng. B5* (1989) 43.
- [36] F. Cheviré, F. Tessier, R. Marchand, *Eur. J. Inorg. Chem.* 2006 (2006) 1223.
- [37] J. Grins, G. Svensson, *Mat. Res. Bull.* 29 (1994) 801.
- [38] R. Marchand, Y. Laurent, J. Guyader, P. L'Haridon, P. Verdier, *J. Eur. Ceram. Soc.* 8 (1991) 197.
- [39] S. G. Ebbinghaus, A. Weidenkaff, A. Rachel, A. Reller, *Acta Crystallogr. C* 60 (2004) i91-i93.
- [40] F. Pors, R. Marchand, Y. Laurent, P. Bacher, G. Roult, *Mater. Res. Bull.* 23 (1988) 1447.
- [41] S. J. Clarke, B. P. Guinot, C. W. Michie, M. J. C. Calmont, M. J. Rosseinsky, *Chem. Mater.* 14 (2002) 288.
- [42] E. Günther, R. Hagenmayer, M. Jansen, *Z. Anorg. Allg. Chem.* 626 (2000) 1519.
- [43] M. Jansen, H. P. Letschert, *Nature* 404 (2000) 980.
- [44] R. Aguiar, D. Logvinovich, A. Weidenkaff, A. Rachel, A. Reller, S. G. Ebbinghaus, *Dyes Pigm.* 76 (2008) 70.
- [45] A. Kasahara, K. Nukumizu, G. Hitoki, T. Takata, J. N. Kondo, M. Hara, H. Kobayashi, K. Domen, *J. Phys. Chem. A* 106 (2002) 6750.
- [46] S. M. Ji, P. H. Borse, G. K. Hyun, D. W. Hwang, J. S. Jang, S. W. Bae, J. S. Lee, *Phys. Chem. Chem. Phys.* 7 (2005) 1315.
- [47] C. M. Fang, G. A. de Wijs, E. Orhan, G. de With, R. A. de Groot, H. T. Hintzen, R. Marchand, *J. Phys. Chem. Solids* 64 (2003) 281.

2. Experimental Methods

Most characterization methods in solid-state chemistry or materials science are based on the interaction of radiation with matter. The radiation used in materials analyses can be divided in two categories: electromagnetic waves and particle beams [1]. The *electromagnetic waves* consist of an electromagnetic field, which is characterized by its frequency ν and wavelength λ . Their energy can be calculated by $E = h\nu$, where h is the Planck constant. The electromagnetic waves are differently classified, depending on their energy/frequency/wavelength, as shown in Fig. 2.1. The interaction between the waves and matter depends on the wavelength. As example infrared light interacts with the molecular vibrations and the characteristic atomic bonds can be identified while x-rays are scattered in the solid material and/or excite electrons and the characteristic atomic structure/composition can be recognized [2].

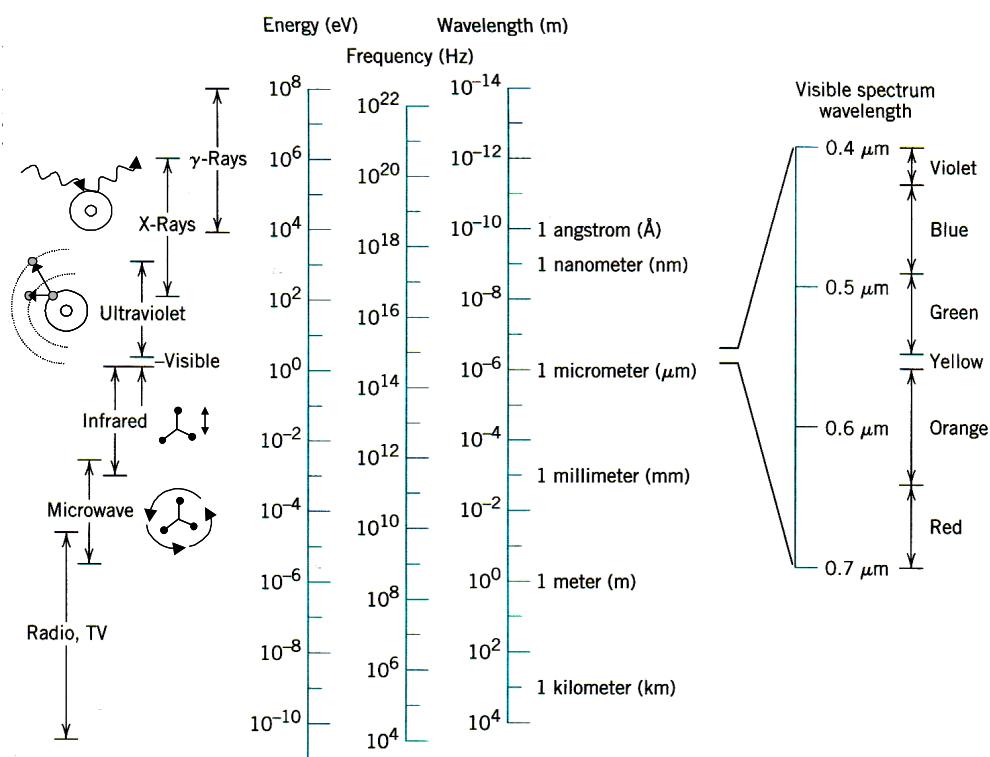


Figure 2.1: Classification of different electromagnetic waves [1].

The *particle beams* are characterized by particles moving with a characteristic velocity v and wavelength λ . The de Broglie equation correlates these parameters with the particle mass m , based on the wave-particle duality: $\lambda = h / mv$. Examples of

matter waves are neutron, electron and ion beams. Their interactions with the samples are described in the following chapters 2.2, 2.7.2, 2.7.3 and 2.10.

2.1 X-Ray Diffraction (XRD)

Crystals consist of a periodic arrangement of atoms or molecules that form a crystal lattice. Regularly spaced atoms in a crystal structure can diffract x-rays. In x-ray diffraction the sample is usually excited with monochromatic radiation of a known wavelength in order to determine the lattice planes (hkl) of the analyzed compound. When x-rays hit a pair of parallel lattice planes at an angle of θ , every atom within the planes acts as a scattering center and emits a secondary wave. The radiations that are reflected with an angle equal to θ reach the detector, as shown in Figure 2.2. All the reflected waves interfere with each other. Constructive interferences occur only when the path length difference between rays scattered from neighboring crystal planes is an integer number of wavelengths of the radiation. The same occurs on the parallel lattice planes within distance, d . When the crystal planes are separated by d , the path length difference is $2d \sin\theta$. As a result, for constructive interference to occur the Bragg law must be obeyed.

$$n \lambda = 2 d \sin\theta \quad (2.1)$$

Consequently for a given d plane spacing and λ wavelength, the first order peak ($n = 1$) will occur at a particular θ value. A powder diffractometer with the most commonly used Bragg-Brentano geometry is schematically represented in Figure 2.3. The x-ray diffractometer works in step scan mode and is operated with $\theta/2\theta$. The result is a diffraction pattern $I(2\theta)$ with peaks corresponding to the hkl reflections. The position of these peaks provides the Bragg reflection angles (i.e. corresponding interplanar spacing) and the intensity of the reflections, which are the fingerprint of the structural phase, allowing the identification of the sample.

Most crystalline species can be identified by their three strongest diffraction peaks. The identification is done comparing the obtained diffraction pattern with those stored in a database. XRD is the most applied analysis method in solid-state chemistry, because it identifies the crystalline structure, also quantitatively.

Additionally, it is non-destructive, fast, simple and only a small amount of sample is required [1].

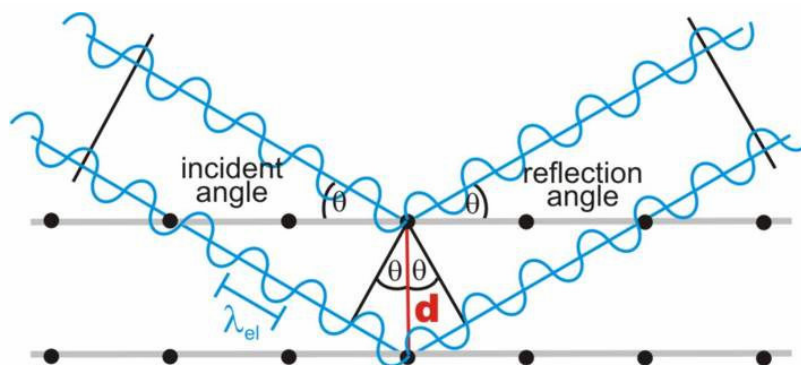


Figure 2.2: Scheme of x-ray diffraction in a crystal [3].

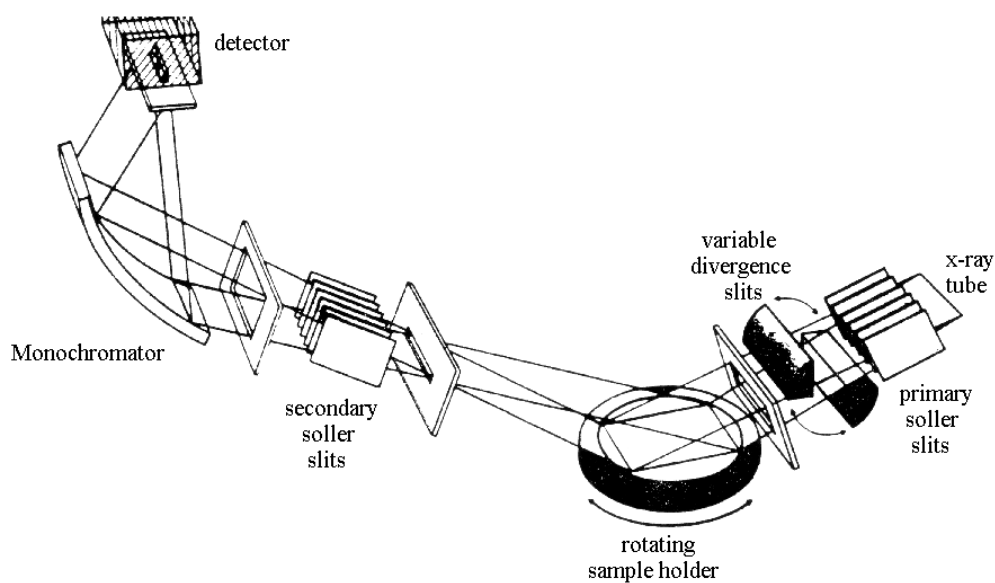


Figure 2.3: Powder diffractometer scheme adapted from [4].

In this work, the samples were characterized by x-ray diffraction using a Seifert θ/θ 3000, diffractometer operating with Cu $K_{\alpha 1,2}$ radiation ($\lambda_1 = 1.54056\text{\AA}$, $\lambda_2 = 1.54439\text{\AA}$). Different scan routines were used depending on the analyzed sample. The polycrystalline compounds (chapter 3.2) were checked in an angular range from 10 to 60° of 2θ , with an increment of 0.02° and a counting time of 1 s/point. For the phase analysis quantification (chapter 5) the same parameters as described before were used but the counting time was increased to 4 s/point. The single crystalline

oxynitride layers (chapter 8) have been examined between 10-70° of 2θ, with an increment of 0.02° and a counting time of 2 s/point. For the Rietveld refinements of Sr_(1-x)La_xTi(O,N)₃ compounds (chapter 6.1) and the samples ammonolyzed by microwave induced plasma (chapter 3.1.2) a broader angular range of 10-150°, a smaller increment of 0.015° and a counting time of 6 s/point were used. The thin films deposited by spin coating and by pulsed laser deposition (chapter 6.2) were checked in an angular range from 10 to 60° of 2θ and were also analyzed in grazing angle configuration, where θ was fixed at 2.5°, in the 2θ range of 22.5-62.5°, with step of 0.02° and 10 s/point. These two configurations were used to verify the relation between film and substrate because the grazing angle configuration minimizes the contribution of substrate peaks on the diffraction pattern but do not shows the diffraction peaks of the films if they are epitaxially grown on the substrate. The database used in the peak analysis was JCPDS powder diffraction file (release 2000, datasets 1-50 plus 70-88).

2.2 Neutron Diffraction (ND)

Neutron diffraction is a complementary method to XRD for atomic structure studies, because certain investigations are difficult or impossible using x-rays. For example, the localization of atomic nuclei or atoms having only few electrons and the observation of magnetic moments are impossible using XRD. X-ray analysis cannot distinguish between oxygen and nitrogen, because they are neighbors in the periodic table and scatter the x-rays approximately with the same intensity. In addition, when heavy atoms are also presented in the crystalline structure the scattering contributions of oxygen/nitrogen are too weak to be detected. Neutron diffraction, in contrast, determines the position of the atomic nucleus and not the maximum of the electron density distribution and it is able to distinguish between O and N. The scattering factor (scattering length) for nitrogen and oxygen are $5.803 \cdot 10^{-15}$ m and $9.360 \cdot 10^{-15}$ m, respectively. The differentiation between O and N is of great importance for oxynitride perovskite structure analysis. Using ND small distortions in the crystalline structure due to anionic dislocations from their ideal positions can be determined and the correct space group of the analyzed phase can be solved. It is also possible to verify if nitrogen is preferentially positioned on a specific atomic position.

Neutron diffraction data were recorded with the high-resolution powder diffractometer for thermal neutrons (HRPT) located at the Swiss Neutron Spallation Source (SINQ) of the Paul Scherrer Institute in Villigen, Switzerland. A picture of the set-up is shown in Figure 2.4. The neutrons originate from a H₂O scatterer close to the SINQ target and pass through a liquid nitrogen cooled Si filter. The diffractometer has scattering angles of 90° or 120° of the monochromator and a position-sensitive detector ³He was used [5]. Samples were placed in cylindrical vanadium sample holders with diameters varying between 6-10 mm depending on the amount of sample. The measurements were performed with a neutron wavelength of $\lambda = 1.494 \text{ \AA}$ in the 2θ angular range of 4.6-164.9° and with a step size of 0.1°.

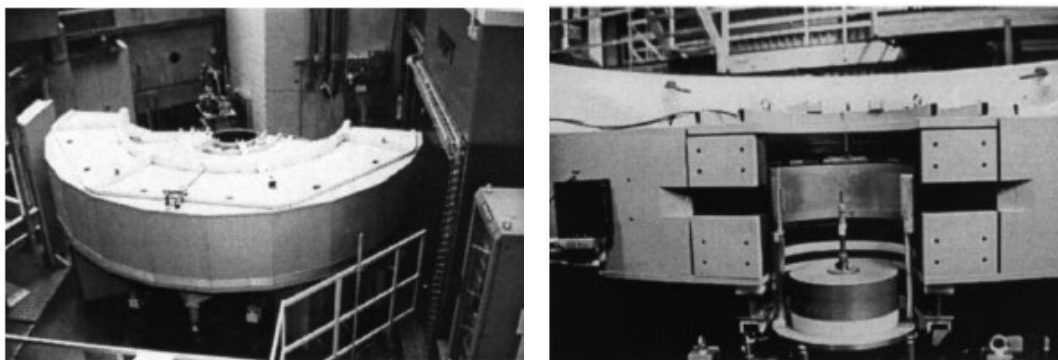


Figure 2.4: Picture of the HRPT at SINQ Paul-Scherrer-Institute in Switzerland [5].

2.3 Rietveld Refinement

The objective of the Rietveld refinement method is to obtain the exact crystal structure of the analyzed powder sample. It is the analog to single crystal structure analysis but for polycrystalline materials. Computer programs are used to fit the measured (x-ray/neutron) diffraction pattern of the sample and performs cyclic calculations to minimize the difference between a given structure model and the experimental data. The refined variables are profile shape, background and structural parameters as lattice constants, atomic positions, (isotropic) atomic displacements, occupation factors and the instrument characteristics. [6-8].

The quality of a Rietveld refinement can be quantified by the calculation of R-factors, as example the profile factor (Rp) and weighted profile factor (Rwp):

$$Rp = \frac{100 \sum_i |y_i^{\text{obs}} - y_i^{\text{cal}}|}{\sum_i y_i^{\text{obs}}} \quad (2.2)$$

$$Rwp = \sqrt{\frac{\sum_i w_i (y_i^{\text{obs}} - y_i^{\text{cal}})^2}{\sum_i w_i (y_i^{\text{obs}})^2}} \quad (2.3)$$

where w_i is a weighting factor ($w_i = 1/\sigma_i^2$, σ_i^2 is the variance assigned to y_i^{obs}),

y_i^{obs} is the measured intensity for each point of the diffraction pattern,

y_i^{cal} is the calculated intensity for each point of the diffraction pattern.

The y_i^{cal} is the resulting intensity (in counts) of the summation of the Bragg reflections contributions at the measured point i .

$$y_i^{\text{cal}} = S \sum_k L_k |F_k|^2 \Phi(2\theta_i - 2\theta_k) P_k A + y_i^{\text{back}} \quad (2.4)$$

where S is the scale factor,

k are the Bragg reflections with the Miller indices (hkl) contributing to the intensity at point i ,

L_k is Lorentz, polarization and multiplicity factor,

F_k is the structure factor for the Bragg reflection k ,

Φ is a function describing the profile,

P_k is the preferred orientation factor,

A is an absorption factor,

y_i^{back} is the background intensity at point i .

In this work the Rietveld refinements were performed using the program FullProf [9]. The aim was to solve the crystal structures of the oxynitrides, to quantify the O/N ratios and to check for possible ionic ordering. The FullProf program was also useful to make quantitative analyses when more than one phase was present in the analyzed samples [10].

2.4 UV-vis Spectroscopy

An UV-vis spectrophotometer measures the intensity of light passing through a sample (I), in comparison to its incident intensity (I_0), as sketched in Figure 2.5. The ratio I/I_0 is called the transmittance, and is usually expressed as a percentage (%T).

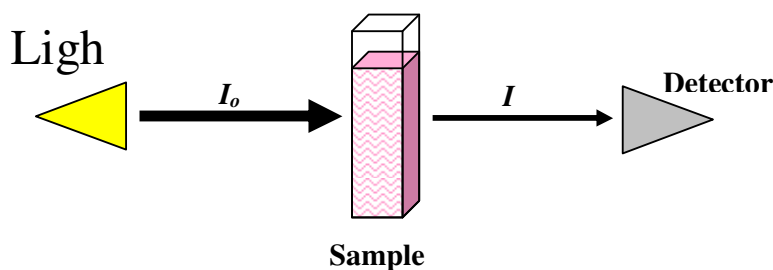


Figure 2.5: Sketch of transmission measurement by UV-vis spectroscopy.

The basic parts of a spectrophotometer are: spectrometer for generating light (often an incandescent bulb for the visible wavelengths and a deuterium arc lamp in the ultraviolet), a holder for the sample, a monochromator to separate the different wavelengths, and a detector. The detector is typically a photodiode [11]. A spectrophotometer can be either single beam or double beam. In a single beam instrument (such as the used Cary 50, shown in Figure 2.6), the whole light passes through the sample cell. I_0 must be measured by removing the sample. In a double-beam instrument, the light is split into two beams before it reaches the sample. One beam is used as the reference while the other beam passes through the sample. Samples are typically placed in a transparent cell, known as a cuvette.

For the measurements of the thin films single and crystalline layers (chapters 6.2 and 8) a Varian UV-vis spectrophotometer model Cary 50 was used in transmittance mode. The optical spectra were recorded in the wavelength range of 200-1100 nm, with scan speed of 240 nm/min. The polycrystalline oxynitride samples described in Chapters 6.1, 7.1 and 7.2 were measured in reflectance mode, in the wavelength range of 250-750 nm, using a Gretag Macbeth colorimeter model Color-Eye 2180. The $\text{LaTi}(\text{O},\text{N})_3$ nanoparticles synthesized by the polyol assisted coprecipitation method (chapter 7.3) have been analyzed using a Perkin Elmer Lambda 19 UV/Vis/NIR spectrometer in diffusive reflectance mode in the range 250-1100 nm.

To enhance the quality of the spectra, the samples were diluted with LiF, which also served as white standard.

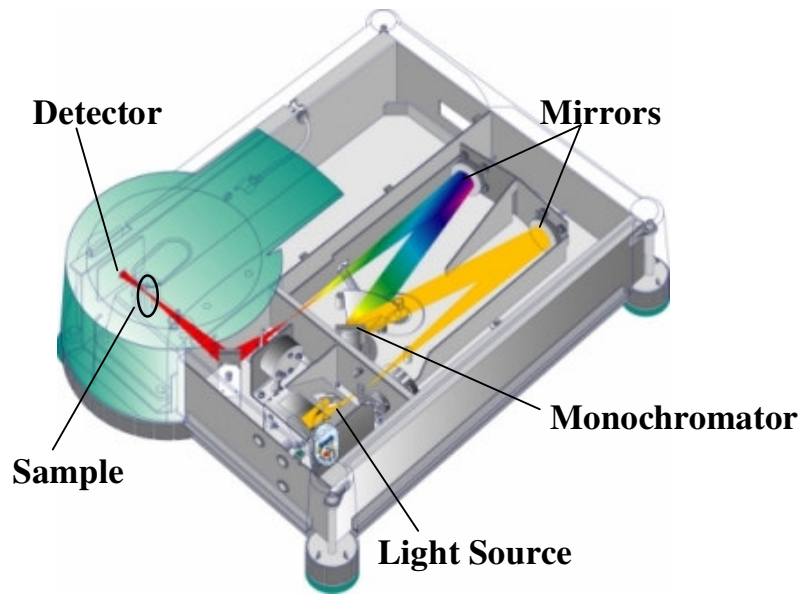


Figure 2.6: Scheme of the UV-vis spectrometer Cary 50 [12].

Data evaluation for band gap calculations was carried out according to Kubelka-Munk theory [13]. Absorbance values (A) are used instead of transmittance (T), the calculation can be done by the following equation:

$$A = \log (1/T) \quad (2.5)$$

The light can also be reflected when passing through the cuvette and the reflectance contribution A_R has to be added to the calculation.

$$A = \alpha d + A_R \quad (2.6)$$

Where α is the absorption coefficient and d is the thickness of the cuvette.

The absorption coefficient α can be calculated, using the band gap energy (E_g)

$$\alpha^r \approx hv - E_g \quad (2.7)$$

Where $h\nu$ is the photon energy and $r = 2$ for direct transition and $r = \frac{1}{2}$ for indirect transition. The difference between direct and indirect band gap is illustrated in Figure 2.7. The distinction concerns the relative positions of the minimum of the conduction band (CB) and the maximum of the valence band (VB) in the Brillouin zone (k). In a material with direct E_g both occur for $k = 0$, while in an indirect E_g the minimum of the CB is for $k \neq 0$ [14].

It is not yet known if the oxynitride perovskites have direct or indirect band gap transition. The two models have therefore been tested. For all measured samples a direct transition ($r = 2$) gave better results, i.e. the plotted lines were sharper with less noise. In any case both models give almost the same values for the band gaps. The direct band gap was determined from a plot of $[(A-A_R) \cdot h\nu]^2$ versus the photon energy $h\nu$ (eV), by extrapolating the linear part of the plot. The intercept with the x-axis is taken as the band gap of the sample [15].

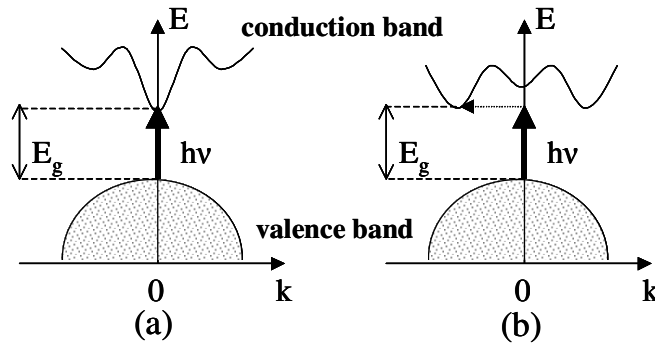


Figure 2.7: (a) direct band gap (b) indirect band [14].

3.5 Colorimetry

CIELab is a 3D graphic system that describes colors with fidelity. This color classification was proposed by the CIE (Commission Internationale de l'Éclairage - International Commission on Illumination). Its three axes L^* , a^* and b^* create a space which can assign a particular color as a point in the 3D coordinate space. The CIELab scheme is illustrated in Figure 2.8. The three basic coordinates represent the lightness of the color ($L^* = 0$ yields black and $L^* = 100$ indicates white), its position between red and green (a^* , negative values designate green while positive values point to red) and its position between yellow and blue (b^* , negative values indicate blue and positive values yield yellow) [16]. The CIELab color parameters of the oxynitride perovskite samples were measured at room temperature in reflectance mode in the

wavelength range of 250-750 nm, using a Gretag Macbeth colorimeter model Color-Eye 2180.

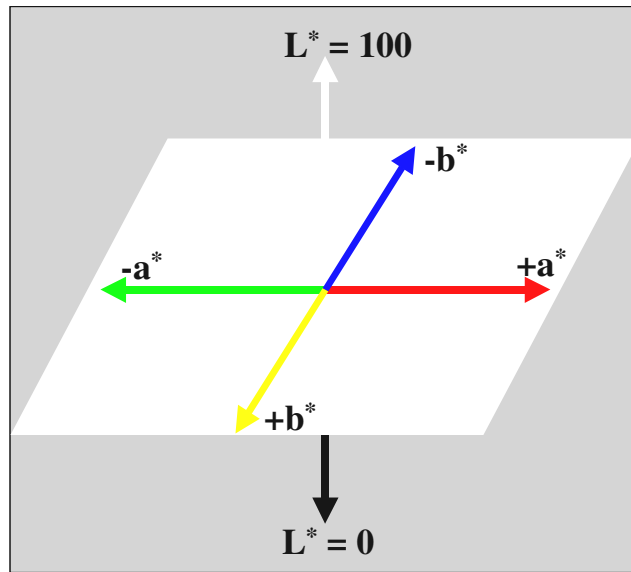


Figure 2.8: Representation of the 3D CIELab system.

2.6 Specific Surface Area by N₂ Physisorption (BET)

The surface area of the samples were measured by the BET method [17] using a Quanta Chrome Nova 2000 system. The measurement is based on physical adsorption of gas molecules on a solid surface. The BET equation is:

$$\frac{1}{v} \left(\frac{P}{P_0} \right) - 1 = \left(\frac{c-1}{v_m c} \right) \left(\frac{P}{P_0} \right) + \frac{1}{v_m c} \quad (2.8)$$

P and P_0 are the equilibrium and the saturation pressure of the adsorbed gas at the temperature of adsorption, v is the adsorbed gas quantity and v_m is the volume of gas adsorbed when the entire adsorbent surface is covered with a complete unimolecular layer. c is the BET constant, which is expressed by:

$$c = e^{\left(\frac{E_1 - E_L}{RT} \right)} \quad (2.9)$$

where E_1 is the heat of adsorption for the first layer, and E_L is that for the second and higher layers and is equal to the heat of liquefaction. Equation 2.8 is an

adsorption isotherm and can be plotted as a straight line with $1 / v[(P_0 / P) - 1]$ on the y-axis and P / P_0 on the x-axis using the experimental results. The linear relationship of this equation is maintained only for low pressures, i.e. roughly in the range of $0.05 < P / P_0 < 0.35$. The values of the slope and the y-intercept of the line are used to calculate v_m and the BET constant c .

The specific surface area S is calculated using the following equation:

$$S = \frac{v_m N s}{M a} \quad (2.10)$$

Where N is Avogadro's number, s adsorption cross-section, M molecular weight of the adsorbed gas and a is the weight of the solid sample.

As an example the BET adsorption isotherm curve for BaTaO_2N , synthesized by solid-state reaction, is plotted in Figure 2.9. The calculated surface area was $2.55 \text{ m}^2/\text{g}$.

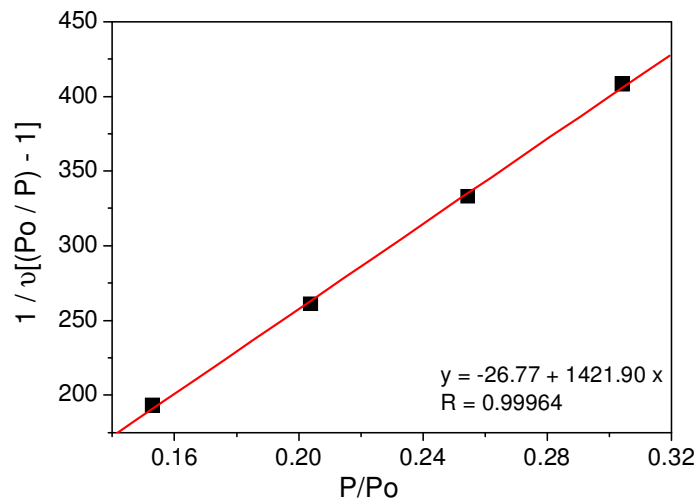


Figure 2.9: Adsorption isotherm curve for BaTaO_2N .

2.7 O/N Analysis

Neutron diffraction is a powerful analysis technique together with a refinement program as FullProf (2.2 and 2.3) can distinguish between oxygen and nitrogen. Additionally it is possible to determine the exact positions, (anisotropic) displacement parameters and site-occupation factors of these anions. Small distortions in the crystalline structure due to anionic dislocations can also be solved. But a

disadvantage of neutron diffraction is the poor accessibility of the neutron scattering facilities. For these reason not all samples can be analyzed during the measurement campaign. As a consequence, preliminary analysis should be performed using other techniques to confirm the presence of nitrogen in the samples and for the quantification of its amount. Alternative methods to measure the nitrogen content in the samples are also required for compounds that are not going to be analyzed by ND (because their small amounts), as for example thin films and the samples synthesized by polyol assisted coprecipitation.

2.7.1 Hot Gas Extraction

A small quantity of sample (approx. 15mg) was placed in a tin container, which is positioned in a double graphite crucible pre-heated at 300°C. Then, the system is heated up to 3000°C, using an inductive furnace, resulting in fusion and carbothermal reduction of the sample. The oxygen presented in the samples reacts with the carbon from the crucible and forms CO/CO₂ while the nitrogen is released as N₂. A flowing helium gas stream carries the released gases over heated rare earth copper oxide that converts CO to CO₂ and hydrogen to water. The nitrogen passes unchanged. The gases flow through an infrared cell where the oxygen is measured as CO₂. A Lecosorb/Anhydrone trap removes water and carbon dioxide, and N₂ is quantified with a thermal conductivity detector [18]. The hot gas extraction is a good technique since it only takes a few minutes to determine the O/N content of a sample. The studied samples were analyzed using a LECO TC500. Silicon nitride and silicon oxide were used as calibration standards for nitrogen and oxygen, respectively. The disadvantage of this technique is that it measures the total amount of oxygen and nitrogen in the sample. If the sample is composed of more than one phase it is not possible to distinguish the anionic content between the phases. X-ray analysis would be a good complementary technique to confirm the phase purity of the sample.

2.7.2 Secondary Ion Mass Spectrometry (SIMS)

In the SIMS a beam of positive ions (generally noble gas ions such as He⁺ and Ar⁺) irradiates the surface of the sample, causing the emission of a variety of secondary particles, including Auger electrons, secondary electrons, neutrons, photons, and positive/negative secondary ions. In SIMS analysis only the secondary ions are concerned [19]. The interaction between the applied ionic beam and the

sample resulting in ionic sputtering of surface is shown in Figure 2.10. The ions leave the sample when the kinetic energy transferred by the ionic beam exceeds the bonding energy of the respective atoms/ions and they are analyzed in a mass spectrometer. The emitted secondary negative/positive ions have mass to charge ratios characteristic for the corresponding elements. Figure 2.11 is a representation of the basic set-up. SIMS analysis is a powerful technique to identify the surface elements and in some cases determine their concentration as function of depth, without any lower atomic number limit as in the case of X-ray spectroscopy [1]. For quantitative analysis it is necessary to investigate standards with similar density as the samples. Depth resolved profiles of secondary ions ($^{14}\text{N}^+$, $^{46}\text{Ti}^+$ and $^{139}\text{La}^+$) were measured by dynamic SIMS from Atomika Instruments model Ion Microprobe 4100. Scanned and focused O^{2+} (enhances secondary ion intensity by 2 to 3 orders of magnitude compared to the use of noble gas ions) primary sputter ion beam of 5 keV energy and current of 65 nA at an incidence angle of 45° were used. The difference between static and dynamic SIMS is that the energy (beam current density) used in the first one is smaller (ca. 1 nA/cm^2) and it is dedicated to the analysis of the top monolayer of the sample, giving molecular information. Since the energy in dynamic SIMS is higher (ca. 10^4 nA/cm^2) it can analyze elemental and isotopic information from the surface and from bulk of the sample [22].

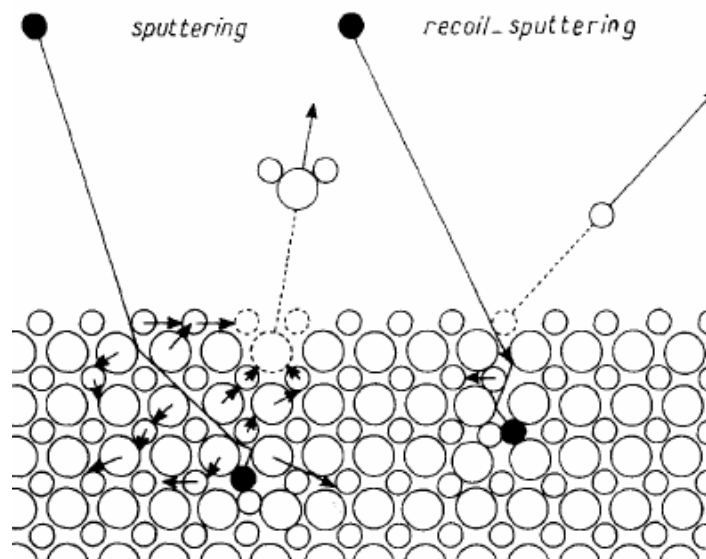


Figure 2.10: Emission process induced by the bombardment of a target by an ion beam [20].

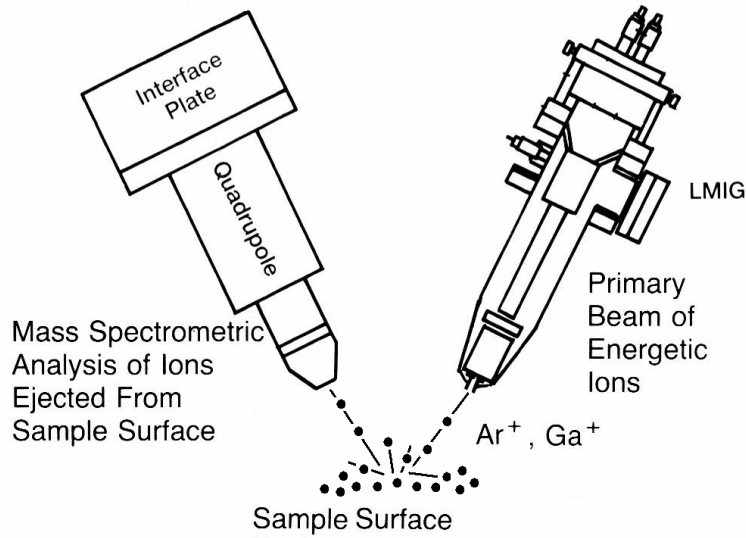


Figure 2.11: Schematic representation of a basic SIMS set-up, adapted from [21].

2.7.3 Elastic Recoil Detection Analysis (ERDA)

The work principle of ERDA is similar to the one of SIMS. SIMS is mainly used for qualitative analyses because it requires a lot of standards to perform a quantification of elements. With ERDA, on the other hand, one can easily quantify O/N due to its specific detection system. In ERDA high energetic heavy ions penetrate the sample at a grazing incident angle. A number of atoms leave the sample as ions and can be detected. The recoiled ions reach the magnetic spectrometer. In the magnetic field the ions are separated according to their momentum [23]. An example for the plot time of flight (TOF) *versus* the energy is shown in Figure 2.12. The high dispersion of the spectrometer leads to a good energy resolution. In the detector four parameters of each ion are measured, the position X , an energy loss ΔE in a gas filled drift chamber, the residual energy E at the scintillator and the time of flight TOF of the particle, which is proportional to the mass number and the total energy of the particle. In the first step of the analysis the different isotopes are identified in a plot ΔE - E , where every isotope forms a separated signal. Then, only one isotope is extracted for the further analysis. Subsequently the spectrum t_0 -TOF is projected on the X -axis, which is proportional to the momentum of the ion and can be transformed in an energy scale.

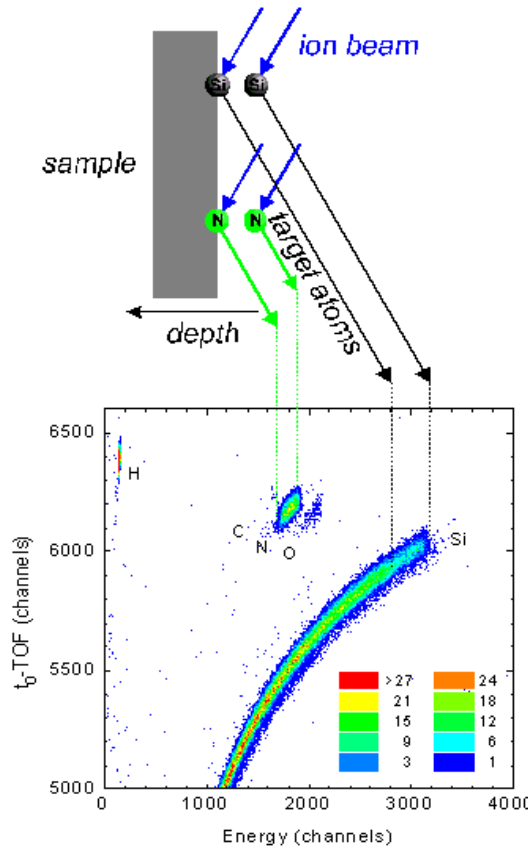


Figure 2.12: Example of ERDA analysis in SiN thin film [24].

Due to the element specific energy loss in material it is possible to calculate the depth-dependent concentration distributions for all components of a sample from the measured energy spectra. The N/O ratios of the oxynitride samples were obtained by ERDA. For the measurements a 12 MeV ^{127}I beam was used under 18° incident angle. The scattered recoils were identified by the combination of a time-of-flight spectrometer with a gas ionization chamber.

2.8 Thermogravimetry (TG) and Mass Spectrometry (MS)

TG is a technique that measures the changes in weight as function of temperature and/or time. The obtained data provides information about the thermal stability and decomposition behavior of the samples [19]. MS can be applied to qualify and quantify molecules evolving during the thermal treatment. Volatile molecules or gases can be examined using electron impact or chemical ionization to give positive or negative ion mass spectra. Compounds with molecular weight up to 300 amu can be analyzed by MS. When TG and MS are combined it is possible to

investigate the products from reactions such as dehydration and thermal decomposition. The samples can be heated up to 1450°C (when Al₂O₃ is used as furnace refractory) and only small amounts of material are required (between 20-1000 mg).

In this work TG/MS was mainly used to investigate the reaction between the oxynitride perovskites and oxygen. The thermal reoxidation studies were performed on a NETZSCH STA 409C thermobalance connected to a Balzers QMS quadrupole mass spectrometer by a skimmer coupling system. Figure 2.13 gives a scheme of the used set-up. The oxidation reactions of the oxynitrides were carried out in the range of 25–1200°C with a heating rate of 10 °C/min in Ar/O₂ mixtures with O₂ contents varying between 0-20% (both gases from Linde with 99.999% purity). The experiments were done in gas flow of 40 ml/min. To allow the detection of N₂ (m/e = 28) evolving during the reaction, mixtures of oxygen/argon instead of oxygen/nitrogen were used.

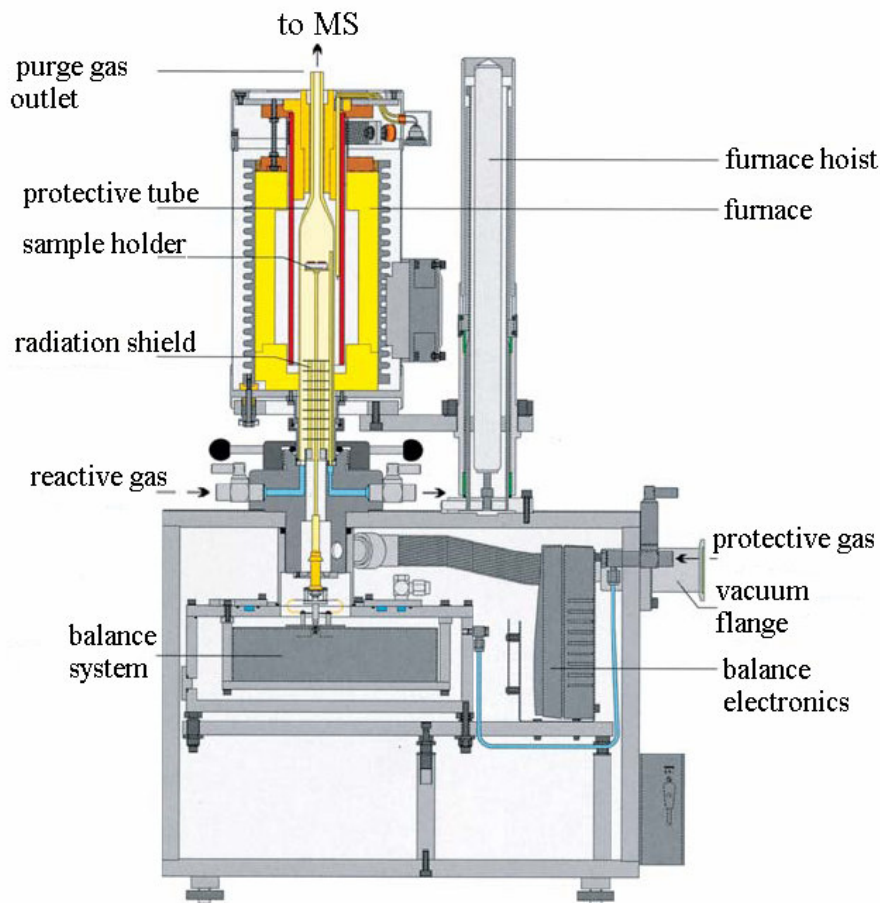


Figure 2.13: Scheme of the used thermo balance [25].

2.9 Atomic Force Microscopy (AFM)

AFM is a scanning technique used to gain topographical information of the sample surfaces as three-dimensional images. A cantilever with a very fine tip almost in contact with the surface applies extremely small forces (10^{-13} - 10^{-6} N) and its interaction with the sample results in tip deflection that is monitored. The tip-surface interactions appear from electrostatic, van der Waals, magnetic and other weak forces, i.e. atomic forces that give the method name [19]. The measurement of the tip movement is done by optical deflection. A laser beam is focused on the top of the cantilever and a photodiode detector quantifies the light reflection, as illustrated by Figure 2.14. The roughness of the spin-coated and PLD thin films (chapter 6.2) were measured by a Thermo Microscopes AFM, model Autoprobe CP-research, on a scanned area of $15 \mu\text{m}^2$ with a scanning velocity of 1 line per sec. The used tip size was around 10 nm and the cantilever was made of silicon covered with gold.

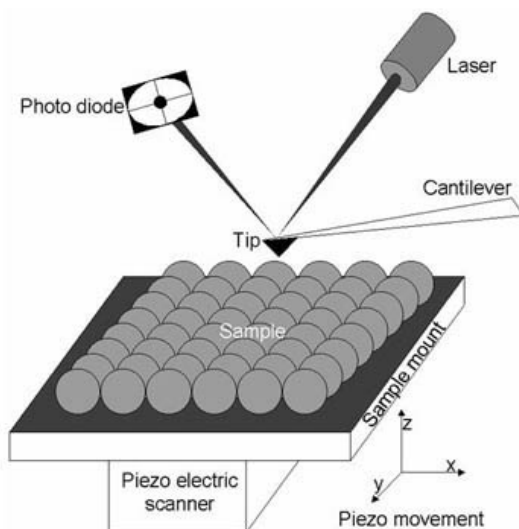


Figure 2.14: Illustration of an atomic force microscopy set-up [26].

2.10 Electron Microscopy (EM)

The resolution of light microscopes is around 500 nm and is directly correlated with the visible light wavelength. Electron microscopes were developed to achieve better resolutions [27]. Electrons have an associated wavelength λ that can be calculated by the De Broglie equation:

$$\lambda = h / m_e v \quad (2.11)$$

where v is the particle velocity, $h = 6.63 \times 10^{-34}$ Js is the Planck constant and $m_e = 9.11 \times 10^{-31}$ kg is the mass of an electron. As example, for obtaining a resolution of 1 nm the necessary velocity of an electron is ca. 100 km/s. To accelerate an electron to this speed, a voltage of around 100 kV is required. The knowledge about glass lenses in light microscopy is completely dominated. On the other side to focalize an electronic beam using magnetic coils is quite complicated. There are two main kinds of electron microscopy: Scanning electron microscopy (SEM) and transmission electron microscopy (TEM). SEM essentially analyses the surface of the sample while in TEM the electron beam passes through the sample. A scheme of an electron microscopy with the basically differences between SEM and TEM is shown in Fig. 2.15.

The electrons are generated with a so-called electron gun. They are accelerated through the anode plate and focused with a system of electrical and magnetic field lenses. The electron gun in the used JEOL TEM is a field-emission gun. It consists of a pointed tungsten cathode tip and two anodes. A positive voltage U_1 of few kV at the first anode generates field strength at the cathode tip. The electric field strength in the tip is so high that the emission occurs by quantum-mechanical tunneling effect. The electrons are accelerated by the voltage U between the cathode tip and the second anode [29]. The main parts of a field-emission gun are shown in Figure 2.16.

2.10.1 Scanning Electron Microscopy (SEM)

The maximum achievable resolution of SEM is about 10 nm and the used voltage varies between 10-40 kV. The scanning coils force the electron beam to rapidly scan over an area of the specimen. The current of electrons reflected from the surface is collected, amplified, and plotted as a two-dimensional micrograph image of the signal intensity. The sample can be viewed in the secondary and backscattered electron mode. Chemical analysis can be performed using energy dispersive spectrometry.

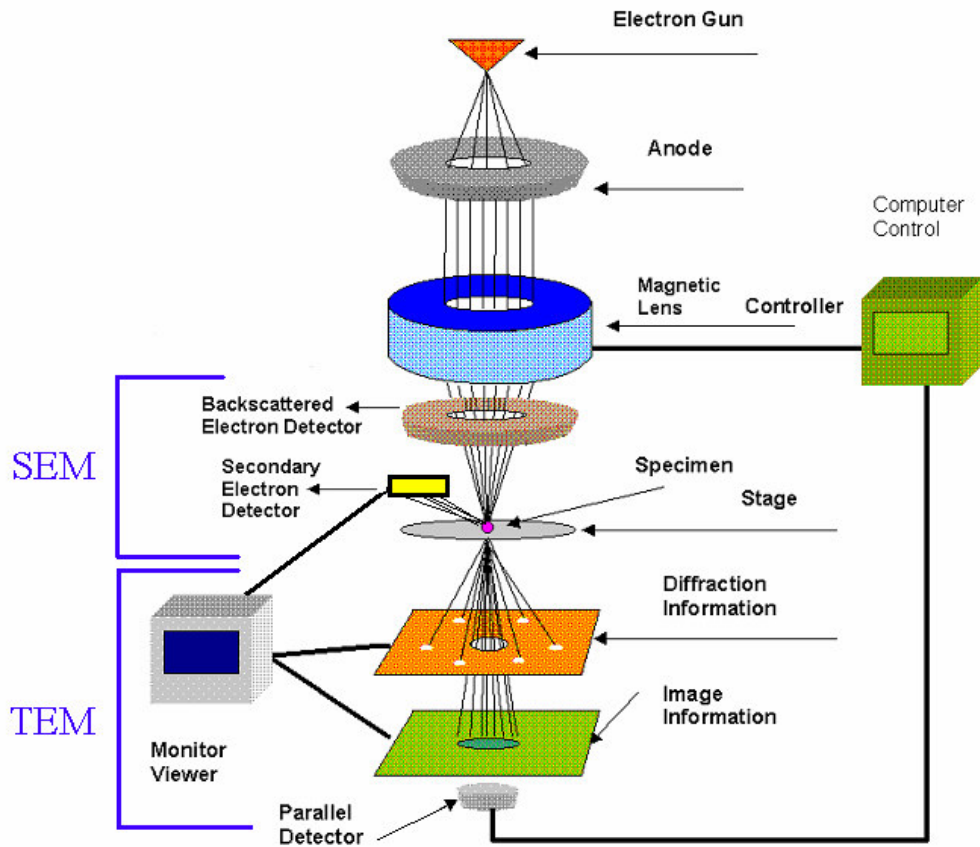


Figure 2.15: Scheme of an electron microscope, showing the basically differences between SEM and TEM (adapted from [28]).

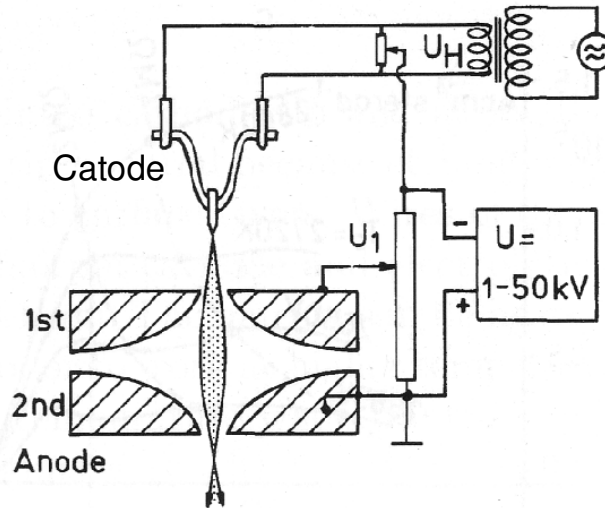


Figure 2.16: Sketch of a field-emission electron gun [29].

Secondary electron mode: The most common imaging mode monitors low energy (≤ 50 eV) secondary electrons (SE). Due to their low energy, these electrons originate within a few nanometers from the surface. The brightness of the signal is proportional to the number of secondary electrons that reach the detector. The SE are differently reflected depending on the tilt angle of the surface of the analyzed sample. The emission at edges and small particles are higher and the shadow contrast that results from incomplete collection can be used to image the surface topography. Thus steep surfaces and edges tend to be brighter than flat surfaces, which result in well-defined topographical images with a three-dimensional appearance [30].

Backscattered electron mode: Backscattered electrons (BSE) are high-energy electrons (typically greater than 50 eV) that have undergone multiple elastic scattering events within the specimen. The most important contrast mechanism of BSE is the dependence of the backscattering coefficient on the mean atomic number. It can be used to detect contrast between areas with different chemical compositions, since the brightness of the BE image tends to increase with the atomic number [30].

Energy dispersive spectroscopy (EDX): Using the high energy of the electron beam that reaches the sample, the atoms radiate characteristic x-rays that can be detected by EDX. The x-rays photons generated by atomic ionization reach the Si(Li) detector, where electron-hole pairs are formed. The created charge pulse is proportional to the energy to the incoming x-ray. The charge is amplified and can be correlated to the atomic element according to its energy. EDX is able to identify the chemical elements presented in the analyzed sample. The EDX technique has the disadvantages of relatively poor energy resolution (approx. 150 eV) that cannot distinguish neighboring elements in the periodic table. Another disadvantage is the inability to detect lighter elements below sodium ($Z = 11$) [31].

A Philips FEI-XL 30 ESEM FEG was used for the microstructure characterization of the oxynitride samples. To avoid a charging of the samples, a thin layer of gold was sputtered on the surface before the microscopy examination.

2.10.2 Transmission Electron Microscopy (TEM)

While SEM works with low voltages (ca. 40kV) the values in TEM varies between the different models from 100 kV to 400 kV. Given that the resolution in TEM is much higher than for SEM and can achieve 0.5nm. The energy of the electrons determines the relative degree of their penetration in a specific sample from

which useful information may be obtained. Electrons are accelerated in the same way as in the SEM, but pass through the specimen. The sample must be very flat and thin (5-100 nm) to do not block the electron beam [29]. The transmitted electrons strike a phosphor screen positioned below the specimen (green surface in Figure 2.15) and light is generated, showing the image. The darker areas of the image represent those regions of the sample that fewer electrons were transmitted, e.g. they are thicker or denser. Diffraction information is obtained adjusting the intermediated lenses and imaged on a higher plane (orange surface in Figure 2.15) [31]. Because of the high spatial resolution obtained, TEM is often employed to determine the detailed crystallography of materials. It is a complementary tool to other crystallographic methods such as x-ray diffraction.

LaTi(O,N)₃ nanoparticles and LaTaO₄/LaTaON₂ crystals (chapters 7.3 and 8, respectively) were analyzed by transmission electron microscopy, using JEOL 2100F at 200 kV field emission electron microscope. The images were taken using a Gatan CCD camera. The LaTiO_{3,5}/LaTiO₂N single crystals (chapter 8) were examined using a Philips CM30 TEM operating at 300kV.

References

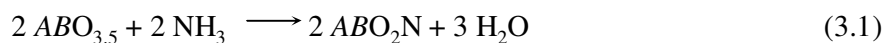
- [1] J.P.Eberhart, Structural and Chemical Analysis of Materials, John Wiley & Sons, 1991.
- [2] <http://hyperphysics.phy-astr.gsu.edu/hbase/mod3.html>. 2008.
- [3] http://www.microscopy.ethz.ch/images/bragg_welle.jpg. 2008.
- [4] H.Krischner, B.Koppelhuberbitschnau, Röntgenstrukturanalyse und Rietveldmethode, 5th.ed.Vieweg & Sohn, 1994.
- [5] P. Fischer, G. Frey, M. Koch, M. Könnecke, V. Pomjakushin, J. Schefer, R. Thut, N. Schlumpf, R. Bürge, U. Greuter, S. Bondt, E. Berruyer, Physica B: Condens. Matter 276-278 (2000) 146.
- [6] R.A.Young, The Rietveld Method, Oxford University Press, 1993.
- [7] W.Massa, Crystal Structure Determination, Springer-Verlag, 2004.
- [8] H. M. Rietveld, J. Appl. Cryst. 2 (1969) 65.
- [9] J. Norwig, H. Weitzel, H. Paulus, G. Lautenschläger, J. Rodríguez-Carvajal, H. Fuess, J. Solid State Chem. 115 (1995) 476.
- [10] J. Rodríguez-Carvajal. Abstracts of the Satellite Meeting on Powder Diffraction of the XV Congress of the IUCr, 127, 1990.
- [11] <http://www.ruf.rice.edu/~bioslabs/methods/protein/spectrophotometer.html>. 2008.
- [12] http://www.varianinc.com/cgi-bin/nav?products/spectr/uv/cary50/cary50_design&cid=KHLLPNNJFI. 2008.
- [13] P. Kubelka, J. Opt. Soc. Am. 38 (1948) 448.
- [14] M.Fox, Optical Properties of Solids, Oxford University Press, USA, 2002.
- [15] S. Locmelis, C. Brünig, A. Börger, M. Binnewies, K. D. Becker, T. Homann, T. Bredow, J. Mat. Sci. 42 (2007) 1965.
- [16] http://en.wikipedia.org/wiki/Lab_color_space. 2008.

- [17] S. Brunauer, P. H. Emmett, E. Teller, *J. Am. Chem. Soc.* 60 (1938) 309.
- [18] Leco Corporation, Form. no. 209-141-003 9/07 REV1 *and* 203-821-202 8/07-REV2 (2007) .
- [19] H.Günzler, A.Williams, *Handbook of Analytical Technique*, WILEY-VCH Verlag GmbH, 2001.
- [20] J. C. Pivin, *J. Mat. Sci.* 18 (1983) 1267.
- [21] J.P.Sibilia, *A Guide to Materials Characterization and Chemical Analysis*, VCH Publishers, Inc., 1988.
- [22] P. Jean-Claude, *J. Mat. Sci.* 18 (1983) 1267.
- [23] W. Bohne, J. Röhrich, G. Röscher, *Nucl. Instrum. Methods Phys. Res. B* 139 (1998) 219.
- [24] http://www-zeuthen.desy.de/technisches_seminar/texte/hmi2002.pdf. 2008.
- [25] <http://www.netzsch-thermal-analysis.com/en/products/detail/pid,34,t,4.html>. 2008.
- [26] <http://sahussain.files.wordpress.com/2007/11/fig-1.jpg>. 2008.
- [27] S.Amelinckx, D.van Dyck, J.van Landuyt, G.van Tengeloo, *Handbook of Microscopy: Application in Materials Science, Solid-State Physics and Chemistry*, VCH Verlagsgesellschaft mbH, 1997.
- [28] <http://www.rpi.edu/dept/materials/COURSES/NANO/shaw/Page5.html>. 2008.
- [29] L.Reimer, *Transmission Electron Microscopy*, Springer Series in Optical Sciences, Springer-Verlag, 1997.
- [30] L.Reimer, *Scanning Electron Microscopy*. Springer Series in Optical Sciences, Springer-Verlag, 1985.
- [31] D.C.Joy, A.D.Romig, J.I.Goldstein, *Principles of Analytical Electron Microscopy*, Plenum Press, 1986.

3. Syntheses, Crystal Structure and Morphology of Polycrystalline Oxynitride Perovskites

3.1 Ammonolysis

Oxynitride samples are prepared by heat treatments of the precursor oxides described in chapter 3.2 (or mixtures of binary carbonates/oxides) under NH_3 . Oxygen is progressively substituted by nitrogen in the compounds to obtain the respective oxynitrides. The ammonolysis reaction for a general $\text{ABO}_{3.5}$ perovskite is given by:



All oxynitrides studied in this work are stable in air, water and diluted acids at room temperature. Depending on the *A* and *B* cations different temperatures and reaction times are necessary to synthesize the oxynitrides. The size of the oxide precursor particles has also a pronounced influence on the ammonolysis time. In general bigger particles need higher temperature and longer time to be completely reacted. In this thesis two different ammonolysis set-ups have been used: conventional furnaces and microwave induced plasma.

3.1.1 Conventional Ammonolysis

In a conventional experiment, the oxide powders are placed in alumina boats and ammonolyzed in a tube furnace with a NH_3 flow of 20-150ml/min. Normally several runs of 18h each and intermediate grindings are necessary to obtain homogeneous and pure phase oxynitrides. This procedure takes a significant time, considering that the furnace has to cool down and heat up again to continuous with the ammonolysis.

A rotating tube furnace was developed to mix the powder during the ammonolysis because the gas-solid reaction mainly happens at the surface of the powder layer. A quartz tube is rotated inside a tube furnace. The intermediate grinding takes much less time than in the static tube furnace because the furnace itself remains hot and only the quartz tube is heated/cooled. Figure 3.1 shows pictures of the described furnaces.



Figure 3.1: Pictures of static (left) and rotating (right) tube furnaces used for ammonolysis.

3.1.2 Microwave Induced Ammonia Plasma Nitridation (MIP)

In this section the fast synthesis of oxynitride perovskites using a modified domestic microwave apparatus is described. Basically, the reaction of the oxide precursors with the ammonia plasma promotes the partial substitution of oxygen by nitrogen, forming the oxynitride perovskite. Differently from the hot ammonia used in the tube furnace ammonolysis, the ammonia plasma contains highly reacting excited nitrogen and hydrogen ions, what increases the ammonolysis kinetics and decreases the necessary reaction time to obtain the oxynitrides.

The scheme and photography of the microwave set-up are shown in Figure 3.2. A commercial microwave oven (CLATRONIC MWG 733, 800W, 50Hz) was modified to promote the oxynitride perovskites synthesis. A circular hole (d ~ 5 cm) was cut in the microwave wall opposite to the magnetron. A Faraday cage was built around the hole with metallic net to avoid microwave radiation leakage. A wave guide(1) of 8 cm x 3.5 cm x 17 cm was built at the exit of the magnetron using 3 mm thick brass plates. It was screwed together with the magnetron wall using a brass plate of 14 cm x 11 cm. A teflon tube with water running was used at the end and around the wave guide as dummy load. The water absorbs the microwaves that were not used in the ammonolysis reaction and is also used to cooling since the hot plasma heats up the device. A quartz reactor tube(2) (d ~ 4 cm) with a closed end was inserted through the wall opening inside the wave-guide. The gases were transported through a smaller quartz tube(3) (d ~ 1 cm) placed in the middle of the reactor that end above the samples, placed around 1 cm from the end of the reactor. The end of the small quartz tube that is outside the microwave was connected to a valve(4), which transports the gases NH₃(5), N₂ and air. The exit of the quartz reactor was joined

through a T-connection to an over pressure valve and to a cold trap(6) cooled down with liquid nitrogen. The cold trap freezes the ammonia avoiding that it corrodes the vacuum pump. Behind the cold trap, a second T-connection attaches the gases lines to the vacuum pump or to the gas exit of the laboratory hood. The gases pass through two acidic water solutions to assure that ammonia is not disposed in the environment.

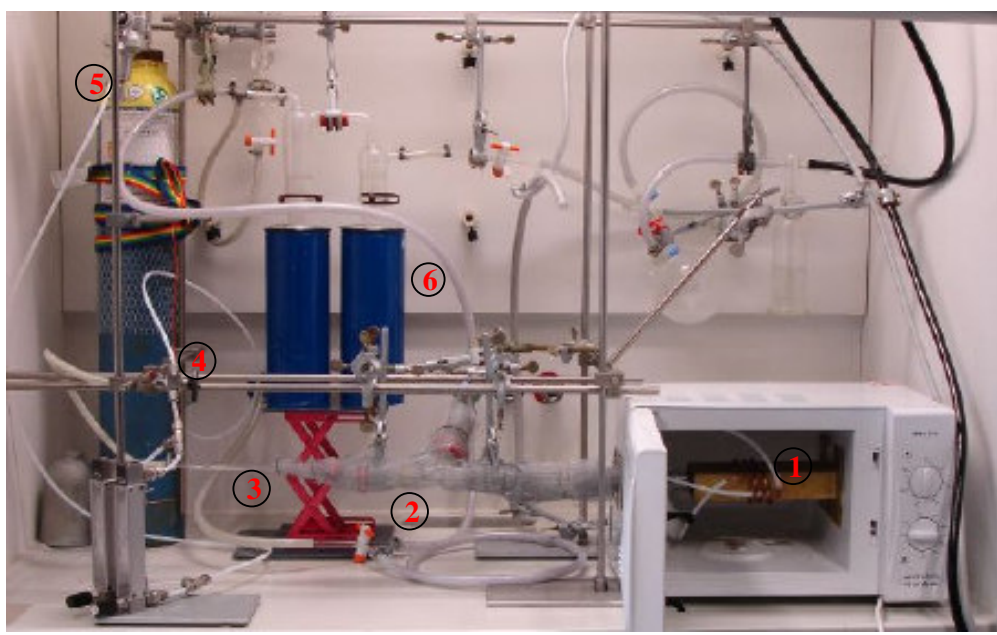
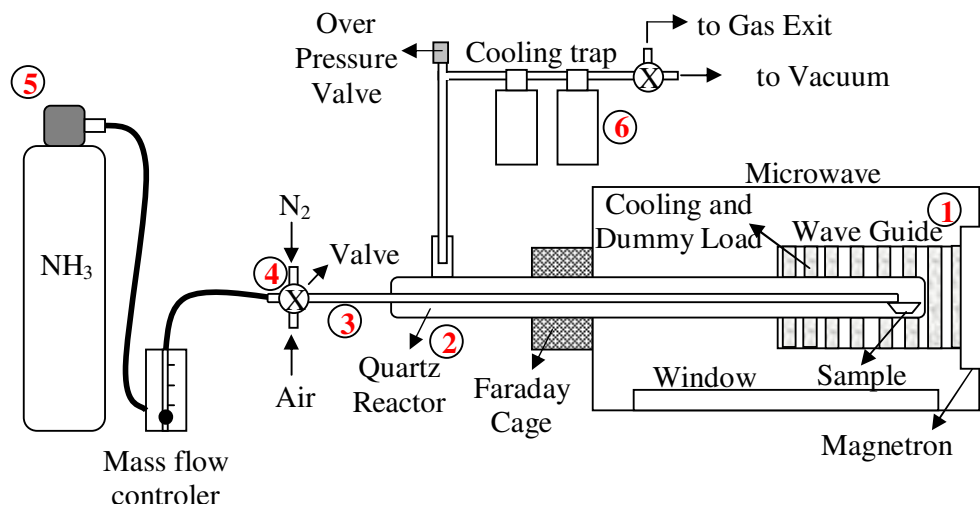


Figure 3.2: Scheme and photography of the used microwave set-up.

To verify if the MIP was suited for the ammonolysis of different compounds, crystalline oxide perovskite and oxide/carbonate precursors were used as starting materials. For the formation of LaTiO_2N the polycrystalline $\text{La}_2\text{Ti}_2\text{O}_7$ was used as

educt while for SrTaO₂N stoichiometric mixture of SrCO₃ with Ta₂O₅ was used. Both reactions were completed within 3h. The oxide Sr₂Nb₂O₇ was also ammonolyzed by MIP. The obtained main compound was SrNbO₂N with Sr_{0.86}NbO₃ and Sr₅Nb₄O₁₅ as impurity phases. Several experiments parameters were modified to try to eliminate the impurity phases, but they were not successful. Figure 3.3 shows the reaction progress for LaTiO₂N. With increasing reaction time the intensity of the oxide peaks decreases while the peaks corresponding to the oxynitride phase grow. After 180 minutes the oxide phase has completely disappeared and the material is composed of almost pure LaTiO₂N.

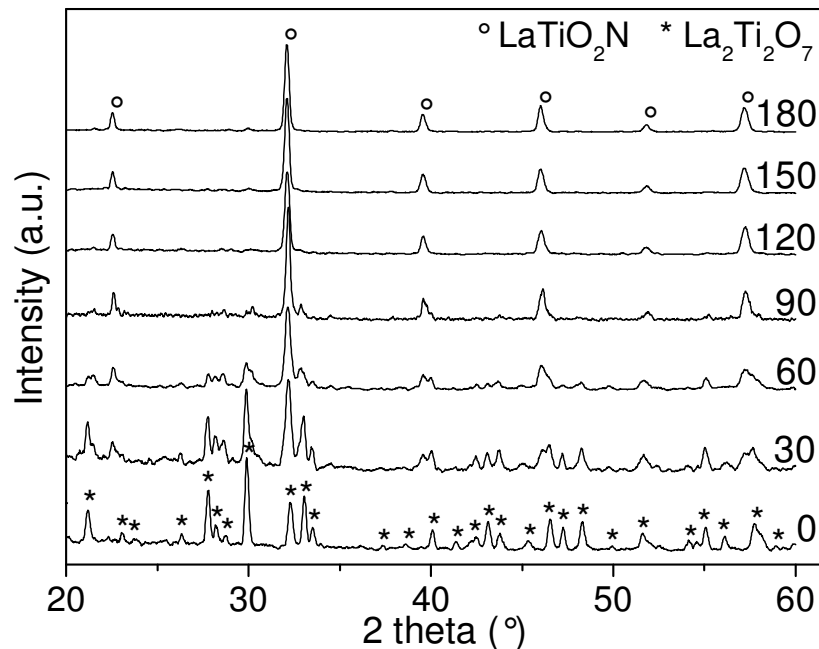


Figure 3.3: X-ray analysis of LaTiO_{3.5} reacted in the ammonia plasma. The reaction time is given in minutes on the right side of each diffraction pattern.

Normally the oxynitrides ammonolyzed in conventional furnaces show a random distribution of nitrogen in the structure. Maybe the different reaction conditions by MIP result in an anionic ordering. The structure of the final reaction products LaTiO₂N and SrTaO₂N were analyzed by neutron diffraction. The Rietveld refinement results are shown in Figures 3.4 and 3.5, and the structural data are summarized in Tables 3.1 and 3.2. The standard deviations are given in parentheses in front of the refined parameters. The initial values were taken from the reference papers [1, 2] and the not refined parameters do not have the corresponding standard deviation values.

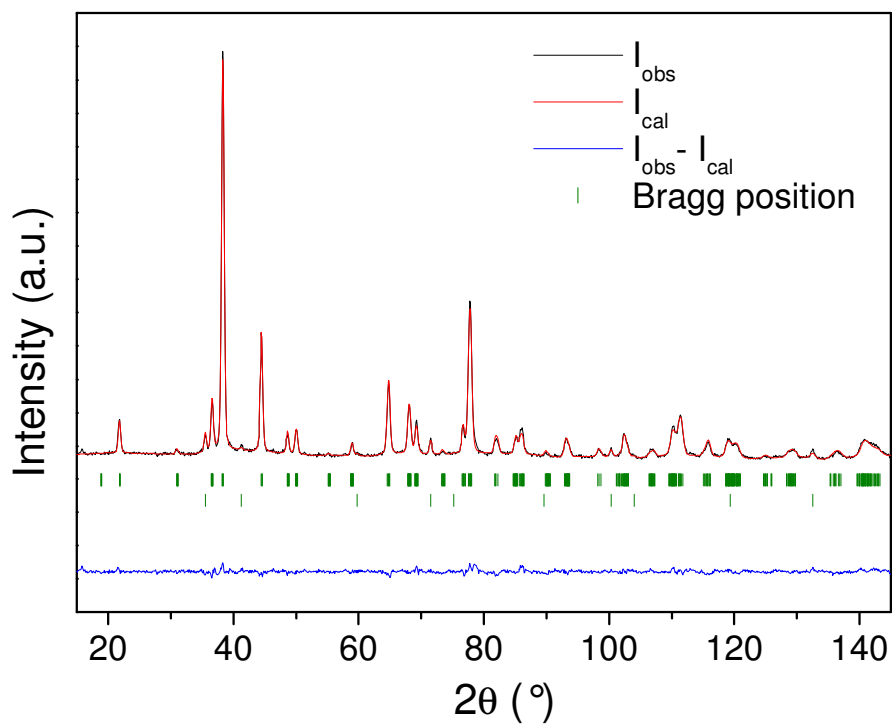


Figure 3.4: Rietveld refinement of LaTiO_2N from MIP assisted nitridation. The top line of Bragg peak positions corresponds to the LaTiO_2N and the bottom line to TiN .

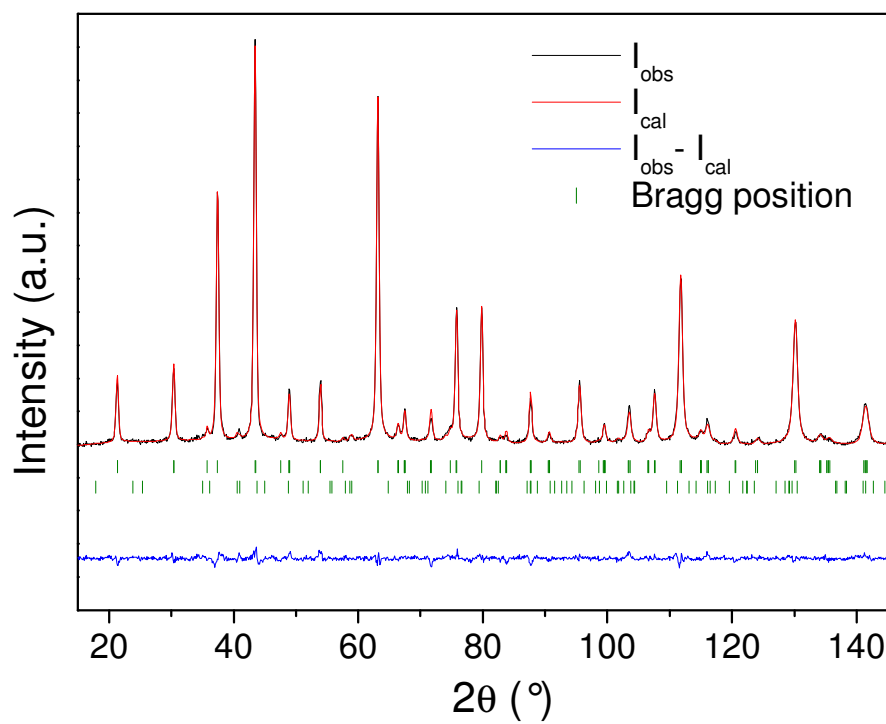


Figure 3.5: Rietveld refinement of SrTaO_2N from MIP assisted nitridation. The top line of Bragg peak positions corresponds to SrTaO_2N and the bottom line to Ta_4N_5 .

Table 3.1: Powder neutron diffraction refinement results for LaTiO₂N and SrTaO₂N from MIP assisted nitridation ($\lambda = 1.494 \text{ \AA}$) at room temperature.

Formula	LaTiO₂N	SrTaO₂N
Space group	$\bar{1}$	I 4/m c m
Crystal system	Triclinic	Tetragonal
$a, \text{ \AA}$	5.5995 (2)	5.7027 (1)
$b, \text{ \AA}$	7.8753 (4)	5.7027 (1)
$c, \text{ \AA}$	5.5728 (2)	8.0788 (4)
$\alpha, ^\circ$	90.181 (4)	90
$\beta, ^\circ$	89.90 (1)	90
$\gamma, ^\circ$	89.96 (1)	90
O/N	2.14(8) / 0.86(8)	2.05(9) / 0.95(9)
%wt second phase	1.62 (5)	1.3 (2)
χ^2	2.06	2.28
R_{wp}	4.41	3.71
R_{exp}	3.07	2.46

Table 3.2: Atomic positions for LaTiO₂N and SrTaO₂N calculated by powder neutron diffraction refinements.

Atom	x	y	z	Biso*	Occ⁺
La	0.49890	0.25160	0.00100	0.89(4)	1.00000
Ti1	0.00000	0.00000	0.00000	0.21(6)	0.50000
Ti2	0.00000	0.50000	0.00000	0.21(6)	0.50000
O1	-0.06200	0.24950	-0.00060	0.7(1)	0.86(5)
N1	-0.06200	0.24950	-0.00060	0.7(1)	0.14(5)
O2	0.26000	0.03580	0.24300	1.69(9)	0.60(8)
N2	0.26000	0.03580	0.24300	1.69(9)	0.40(8)
O3	0.25500	0.47300	0.75700	1.69(9)	0.67(7)
N3	0.25500	0.47300	0.75700	1.69(9)	0.33(7)

Atom	x	y	z	Biso*	Occ⁺
Sr	0.00000	0.50000	0.25000	0.48(2)	1.00000
Ta	0.50000	0.50000	0.00000	0.13(3)	1.00000
O1	0.00000	0.00000	0.25000	0.7(2)	0.77(8)
N1	0.00000	0.00000	0.25000	0.7(2)	0.22(8)
O2	0.7665(4)	0.2665(4)	0.00000	1.26(9)	1.28(9)
N2	0.7665(4)	0.2665(4)	0.00000	1.26(9)	0.72(9)

* Isotropic displacement parameter ⁺ Occupancy factor

The results obtained by Rietveld refinements agree with the published crystal data with triclinic and tetragonal symmetry for LaTiO₂N and SrTaO₂N, respectively [1, 2]. Nitrogen is randomly distributed in both crystal structures. A small quantity of

binary nitride phases was found as impurity in both compounds. For LaTiO_2N 1.6 wt% of TiN was present while for SrTaO_2N 1.3 wt% of Ta_4N_5 was observed.

SEM pictures of the ammonolyzed samples can be seen in Figure 3.6. LaTiO_2N is composed of irregular particles with sizes varying between 0.6-1.8 μm while the SrTaO_2N is formed of smaller particles with diameter of 0.1-0.4 μm . The BET surface area of the samples show high values of 16 m^2/g and 58 m^2/g for LaTiO_2N and SrTaO_2N , respectively.

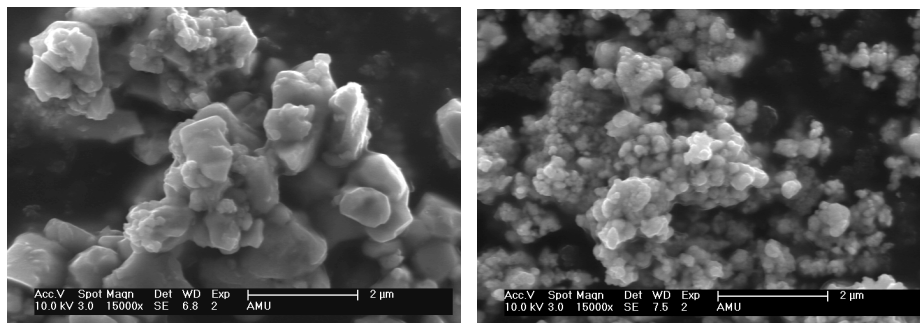


Figure 3.6: SEM of LaTiO_2N (left) and SrTaO_2N (right) after 3 hours of plasma ammonolysis.

In summary it can be stated that microwave induced ammonia plasma was successfully applied to synthesize oxynitride perovskite. As demonstrated, it is possible to start with the respective oxide as $\text{La}_2\text{Ti}_2\text{O}_7$ or with the binary oxide/carbonate mixtures e.g. Ta_2O_5 and SrCO_3 in the case of SrTaO_2N . The ammonolysis reaction in MIP is much faster than in conventional furnaces. As example, to synthesize LaTiO_2N in a tube furnace under flowing ammonia at 950°C it takes 32 h [1] while SrTaO_2N is fully ammonolyzed in 24 h at the same temperature [3]. In the studied MIP set-up it took only 3 h to ammonolyze the same oxides. The microwave nitridation is thus around ten times faster than the conventional ammonolysis and a big amount of ammonia can be saved. Electrical energy is also economized not only because of the shorter time of reaction, but also for the substitution of high energy consuming laboratory furnaces (0.6 - 7 kW/h) [4, 5] by a domestic microwave (ca. 0.8 kW/h). Except the two samples (LaTiO_2N and SrTaO_2N) described in this section, all the other oxynitrides discussed in the following chapters were ammonolyzed in conventional furnaces. Because the building of MIP set-up was one of the last experiments performed during the thesis.

3.2 Synthesis Methods for Polycrystalline Oxide Precursors

As discussed before the way to prepare the oxynitride perovskites is reacting the oxide/carbonate precursors or $ABO_{3.5}$ and ABO_4 perovskites with ammonia. There are different methods to synthesize the $ABO_{3.5}$ and ABO_4 perovskites either as crystalline or amorphous material. Depending on the used synthesis technique different crystallinities, morphologies and particle sizes are obtained. These various synthesis routes are described in the following sections.

3.2.1 Solid-State Reaction

Solid-state synthesis is the most often used method to prepare poly-cationic oxides because it is quite simple and easy to perform. The oxide/carbonate educts are well ground using mortar and pestle or ball mills. Normally some liquid (water or an alcohol) is added to help the grinding. After drying, the powder is submitted to high temperatures to trigger the ionic diffusion. In general, with this method the obtained particles are rather big (several μm in diameter), show a small surface area, good crystallinity and in some case a poor homogeneity, which can be improved by additional regrinding/heating cycles. In most cases, quite high temperatures and long reaction times are required for a complete reaction.

The oxides $\text{NdTiO}_{3.5}$, $\text{LaTiO}_{3.5}$, $\text{SrTaO}_{3.5}$ and $\text{SrNbO}_{3.5}$ used to produce the stabs for the single crystal growth (chapter 8) as well as the BaTaO_2N , BaNbO_2N , SrNbO_2N , SrTaO_2N and LaTiO_2N oxynitrides used in the photocatalysis experiments (chapter 6) and in the thermal oxidation study (chapter 5) were prepared by solid-state reactions. Stoichiometric quantities of BaCO_3 (99.9% Aldrich), SrCO_3 (99.9% Aldrich), Ta_2O_5 (99% Aldrich), TiO_2 (99.9% Aldrich), Nb_2O_5 (99.9% Aldrich) and pre-dried Nd_2O_3 (99.9% Aldrich) and La_2O_3 (99.9% Chempur) were mixed. The oxides were well ground under iso-propanol in an agate mortar. The mixtures were reacted between 1000-1400°C, depending on the chemical composition, for several cycles of 24 h with intermediate grinding in a box furnace under air. Approximately 1g of each oxide was reacted with ammonia to yield the respective oxynitrides. The ammonolysis of the samples was done in a tube furnace with an ammonia flow of 25 ml/min. The respective reaction time and temperature are shown in Table 3.2. Figure 3.7 shows the x-ray diffraction patterns of the studied oxynitride compounds. All compounds were found to be single phase. BaNbO_2N and BaTaO_2N show cubic unit cell while SrNbO_2N and SrTaO_2N possess tetragonal distorted perovskite structures.

In contrast LaTiO_2N is reported to be triclinic structure [1, 6-8]. Figure 3.8 shows scanning electron micrographs from different oxynitrides synthesized by solid-state technique. The samples have quite large particles in the range of 10-100 μm and small BET surface areas around 3 m^2/g .

Table 3.2: Temperature and time of ammonolysis for the oxynitrides synthesized by solid-state reaction.

Sample	T ($^{\circ}\text{C}$)	Time (h)
BaTaO_2N	1000	54
BaNbO_2N	950	72
SrNbO_2N	950	54
SrTaO_2N	1000	36
LaTiO_2N	950	126

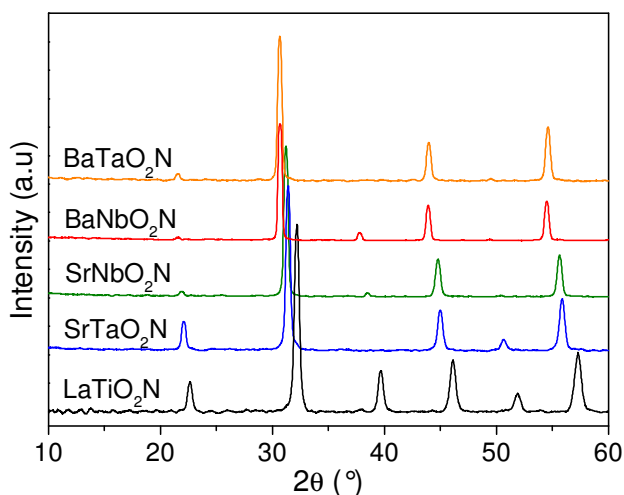


Figure 3.7: XRD patterns of the studied oxynitride perovskites LaTiO_2N , SrNbO_2N and SrTaO_2N .

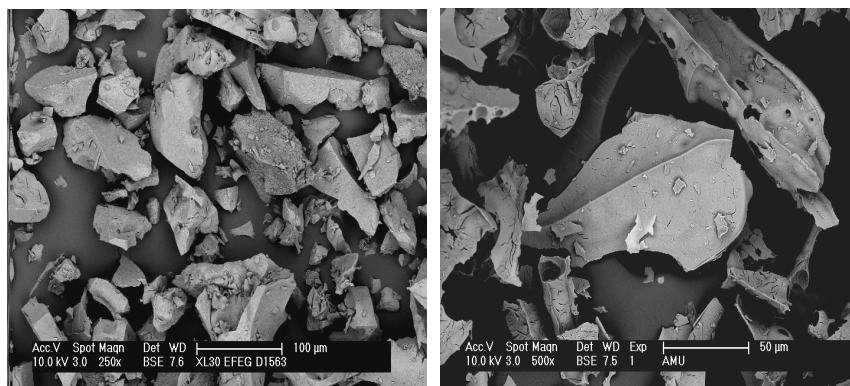


Figure 3.8: SEM pictures of SrTaO_2N (left) and LaTiO_2N (right) synthesized by solid-state reaction.

3.2.2 Pechini Synthesis

The Pechini method is one variation of the so-called soft chemistry (*Chimie Douce*) methods. The soft chemistry syntheses usually start from dissolving stoichiometric quantities of the desired cations (e.g. nitrates, chlorides or alcoholates) in an aqueous solution. In the Pechini process citric acid promotes the chelation of the cations. The citric acid stabilizes the dissolved cations in solution avoiding their precipitation for example as hydroxides [9]. The reaction of the salts with the organic compound to give stable complexes is schematically shown in Figure 3.9. This technique has the advantage to yield homogeneous oxides and to decrease the necessary time and temperature of synthesis [10].

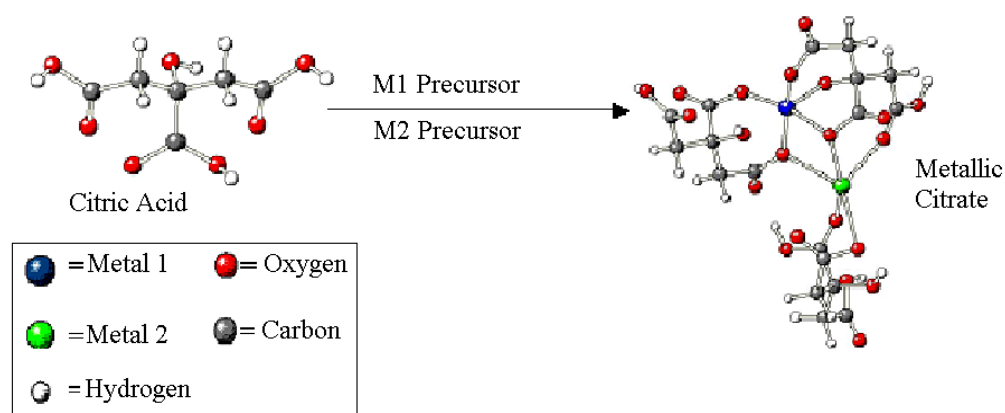


Figure 3.9: Scheme demonstrating the stabilization of the metallic cations in solution by citric acid [11].

The oxynitride compounds CaNbO_2N , CaTaO_2N , SrNbO_2N , BaNbO_2N , SrTaO_2N , NdTaO_2N , and LaTiO_2N , used as pigments (chapter 4) and in the thermal oxidation/photocatalysis studies (chapters 5 and 6) were synthesized by the ammonolysis of the respective oxide precursors. The oxide educs were prepared by Pechini method. The used chemicals reagents were $\text{Ca}(\text{NO}_3)_2 \cdot 4\text{H}_2\text{O}$ (p.a. - Fluka), $\text{Sr}(\text{NO}_3)_2$ (p.a. - Fluka), $\text{Ba}(\text{NO}_3)_2$ (99% - Aldrich), NbCl_5 (98% - Riedel-de Haen), $\text{La}(\text{NO}_3)_3 \cdot 6\text{H}_2\text{O}$ (p.a. - Fluka), TaCl_5 (p.a. - Merck), $\text{ZrC}_{12}\text{H}_{28}\text{O}_4$ (70wt.% solution in 1-propanol - Aldrich), $\text{Yb}(\text{NO}_3)_3 \cdot 5\text{H}_2\text{O}$ (p.a. - Serva), $\text{TiC}_{12}\text{H}_{28}\text{O}_4$ (97% - Aldrich) and citric acid (99% - Fluka). The used citric acid: total amount cations ratio was 2:1. For the chlorides TaCl_5 and NbCl_5 , it is necessary to dissolve them in a solution of anhydrous citric acid and dry ethanol, in order to avoid the formation of oxide/hydroxide precipitation. The solutions were heated to around 70°C and kept at

this temperature under constant stirring until completely dissolution of the cationic precursors. Afterwards, the temperature was increased up to ca. 150°C. After evaporation of the solvent, the organic component formed a stable gel, embedding the cations. In a subsequent reaction step the organic matrix was burned out at 650°C for 2h. Amorphous powders were obtained, which contained the different cations mixed on the atomic scale. The amorphous oxide powders were placed in alumina crucibles and reacted in a tube furnace with a NH₃ flow of 50-150 ml/min to result in well-crystallized oxynitrides. Different heating temperatures and reaction times were necessary for complete ammonolysis of the diverse oxynitride compounds as listed in Table 3.2. The oxynitride samples showed a well-defined perovskite structures without preferential orientation, as displayed in Figure 3.10. Impurities were only found for CaTaO₂N, which shows a small quantity (< 1 %wt) of Ta₂O₅ as second phase.

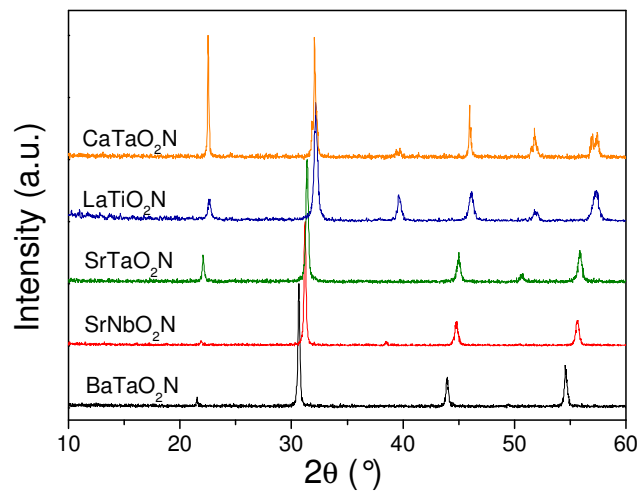


Figure 3.10: X-ray diffraction pattern of the oxynitrides prepared by the Pechini method.

Table 3.2: Temperature and time of ammonolysis for the oxynitrides synthesized by the Pechini method.

Sample	T (°C)	Time (h)
CaTaO ₂ N	950	18
SrTaO ₂ N	950	18
BaTaO ₂ N	1000	54
NdTaO ₂ N	1000	54
SrNbO ₂ N	950	36
CaNbO ₂ N	950	60
LaTiO ₂ N	950	24

Figure 3.11 shows SEM pictures of several samples prepared by the Pechini method. The samples consist of foamy agglomerated irregular small particles with diameters around 200 nm and BET surface area of ca. 10 m²/g.

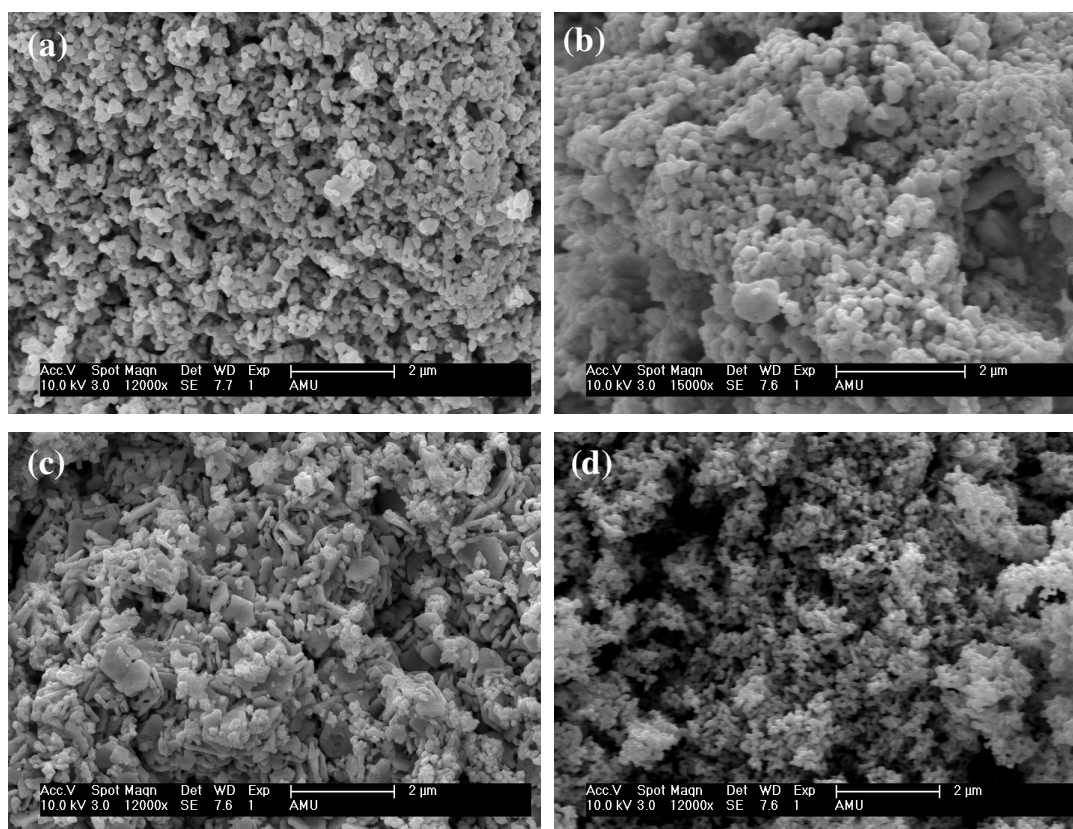


Figure 3.11: SEM pictures of (a) SrNbO₂N, (b) BaTaO₂N, (c) SrTaO₂N and (d) LaTiO₂N synthesized by the Pechini method.

3.2.3 Spray Pyrolysis

The basic idea of the spray pyrolysis is to use droplets of an aerosol as micro-reactors, which results in non-agglomerated individual particles. An aqueous solution containing stoichiometric ratios of the desired cations is nebulized, generally by means of an ultra-sonic vapor generator. A flowing gas transports the aerosol through a hot tube reactor [12, 13]. After drying of the small droplets the corresponding solid-state reaction takes place, forming the desired phase. These reactions are quite fast because the particles are relatively small. The time it takes for a droplet to pass through a vertical tube furnace kept at around 1000°C (in the order of some seconds) usually is enough to complete the reaction. The formed particles are collected at the end of the quartz tube. Small and chemically homogeneous particles are usually obtained. Spray pyrolysis is a good technique to prepare large quantities of powders

because it is a continuous process. Figure 3.12 shows a spray pyrolysis apparatus in detail.

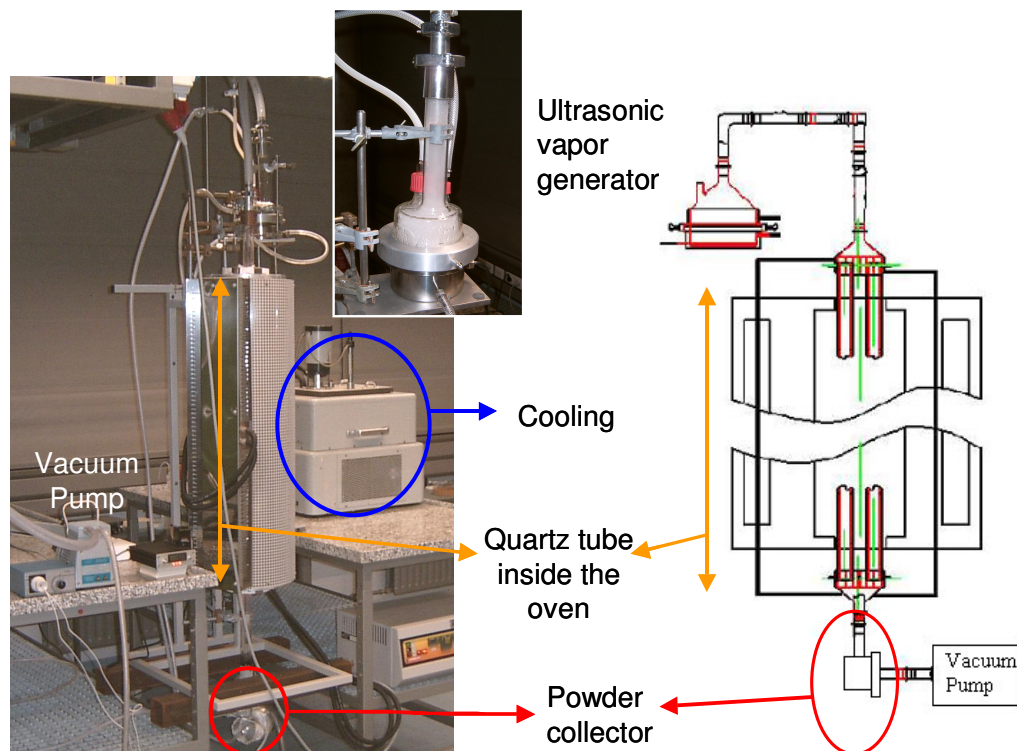


Figure 3.12: Photograph and schematic sketch of spray pyrolysis set-up.

LaTiO₂N prepared by spray pyrolysis was used in the photocatalysis study (chapter 6). LaTiO_{3.5} was synthesized using the same solution as for the Pechini approach, described in the previous section. The solution was placed in an ultrasonic bath and the liquid molecules were carried by oxygen flow of 100 cm³/min through the tube furnace at 1000°C. Oxygen was used to assure the complete burning of the organic matrix and to avoid titanium reduction. Afterwards, the particles were ammonolyzed at 1000°C during 24 h. The sample is composed of single phase LaTiO₂N. The typical morphology of the particles is shown in Figure 3.13.

In general the obtained particles have homogeneous spherical shape and an average diameter around 1 μm. After ammonolysis the particles maintained the spherical shape but the surface became rough. Figure 3.14 shows the x-ray diffraction pattern of the ammonolyzed product. It is almost pure LaTiO₂N with small quantity of LaTiO₃.

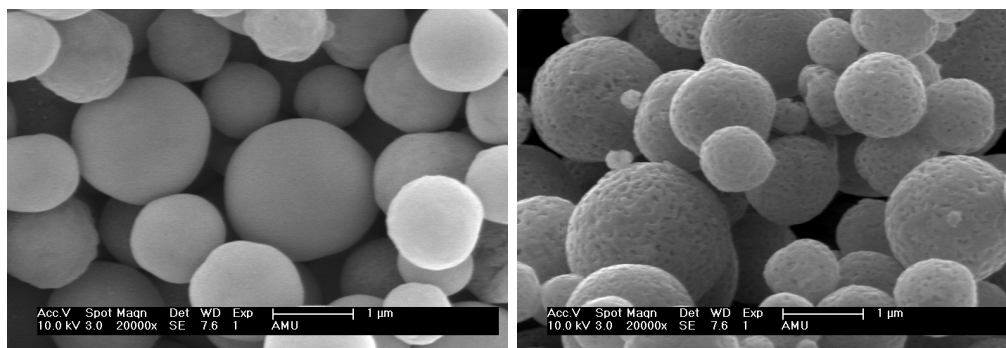


Figure 3.13: SEM picture of $\text{LaTiO}_{3.5}$ produced by spray pyrolysis (left) and LaTiO_2N after ammonolysis (right).

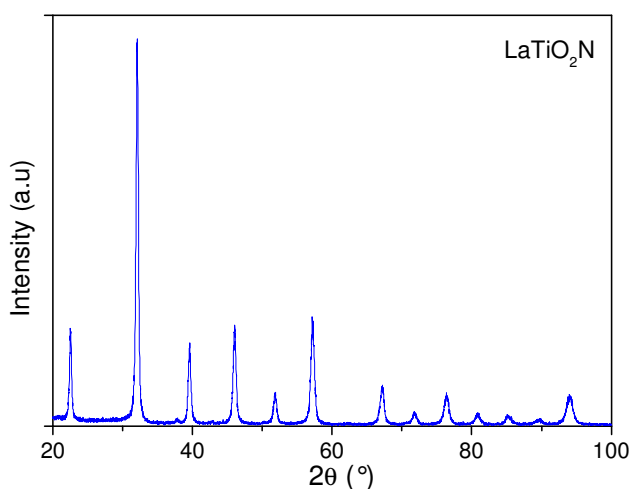


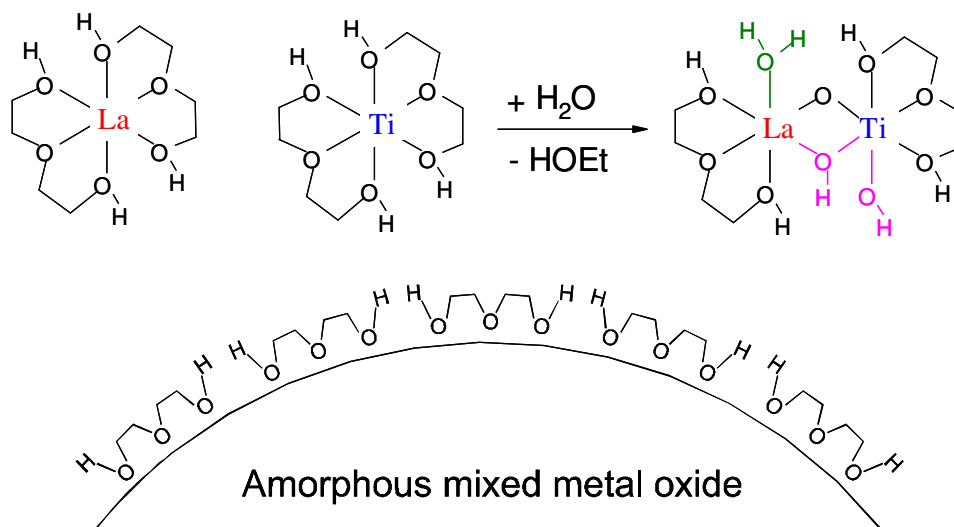
Figure 3.14: X-ray diffraction pattern of LaTiO_2N produced by spray pyrolysis.

3.2.4 Polyol Assisted Coprecipitation

Although the polyol synthesis has been widely used for the preparation of metals and binary oxides, it is a rather new technique to synthesize ternary oxides [14, 15]. The polyol method starts from dissolving metal salts in a chelating polyalcohol („polyol“) at elevated temperatures. A hydrolysis agent is used to initiate the cations co-precipitation leading to (amorphous) oxide nanoparticles. The experiments are usually carried out in a closed reaction flask attached to a reflux condenser. The polyol approach is a good technique to synthesize nanoparticles with fine size control, because the alcohol acts as a surface-capping agent avoiding particles agglomeration, as schematically illustrated in Figure 3.15. On the other hand,

it is in some cases quite difficult to adjust the final composition of the precipitated oxide when complex stoichiometries are desired. The reason is that in these cases several cationic precursors have to be added. Since these precursors might differ in their hydrolysis behavior, the composition of the precipitate does not always match the one of the solution. It is also difficult to find the appropriate hydrolysis agent. In some cases atmospheric moisture is already sufficient, while there are other cases in which larger quantity of water or even HNO_3 or KOH have to be added.

Figure 3.15: Scheme of polyol synthesis. The metal salts are dissolved in the



chelating polyalcohol. Controlled condensation by hydrolysis occurs, forming the amorphous oxide nanoparticles. The alcohol (DEG) acts as a surface-capping agent, avoiding particle agglomeration during the precipitation stage and leading to the formation of small particles.

$\text{LaTi}(\text{O},\text{N})_3$ prepared by polyol co-precipitation was used in the photocatalytic studies (chapter 6). The $\text{LaTiO}_{3.5}$ nanoparticles were synthesized using 550.60 mg of $\text{La}(\text{NO}_3)_3 \cdot 6\text{H}_2\text{O}$ (99% Fluka) and 372.45 mg of $\text{TiC}_{12}\text{H}_{28}\text{O}_4$ (97% Aldrich) dissolved in 35 ml of diethylene glycol (99% Aldrich). The reaction was performed in N_2 atmosphere to avoid early titanium oxide precipitation, normally initiated by air humidity. The mixture was heated at 130°C for 1 h. During this time a clear solution formed. Then 0.5 ml of KOH (2M) was added to promote the hydrolysis of the cations. After that, the solution was heated to 180°C and kept at this temperature for 4h to promote the oxides precipitation. The obtained powder was separated from the diethylene glycol by centrifugation and washed with acetone several times. The amorphous La-Ti-oxide was heated at 800°C during 4h to completely eliminate the organic compounds and to form well-crystalline $\text{LaTiO}_{3.5}$. This white powder was reacted for 3 h in a tube furnace (sec. 3.1.1) under NH_3 flow of 25 ml/min. Four

samples were prepared, they were ammonolyzed at different temperatures: 800°C, 870°C, 920°C and 1000°C.

The x-ray diffraction patterns of the samples nitrated at 800-1000°C are plotted in Figure 3.16. All observed peaks correspond to LaTiO_2N and no impurity phase was detected. It is apparent that with increasing temperature of ammonolysis the peaks in the diffraction pattern become sharper indicating a better crystallinity of the material. The average crystallite size increases with synthesis temperature from 10 nm for the sample reacted at 800°C to 28 nm for the one synthesized at 1000°C.

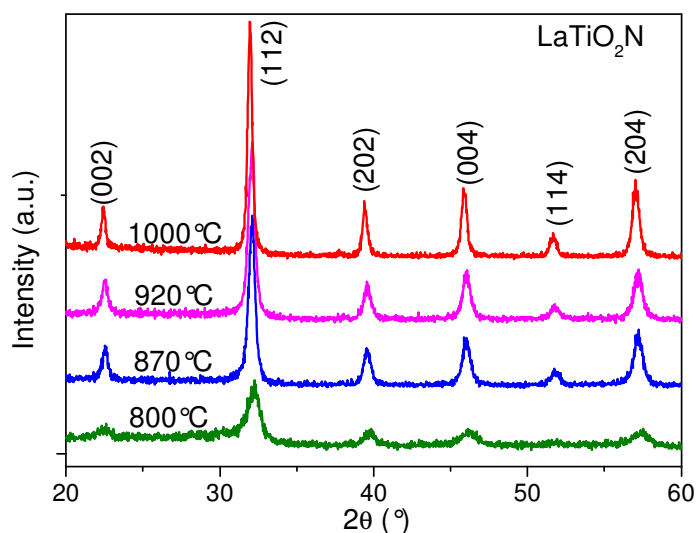


Figure 3.16: XRD patterns of the studied $\text{LaTi}(\text{O},\text{N})_3$ reacted with ammonia at different temperatures.

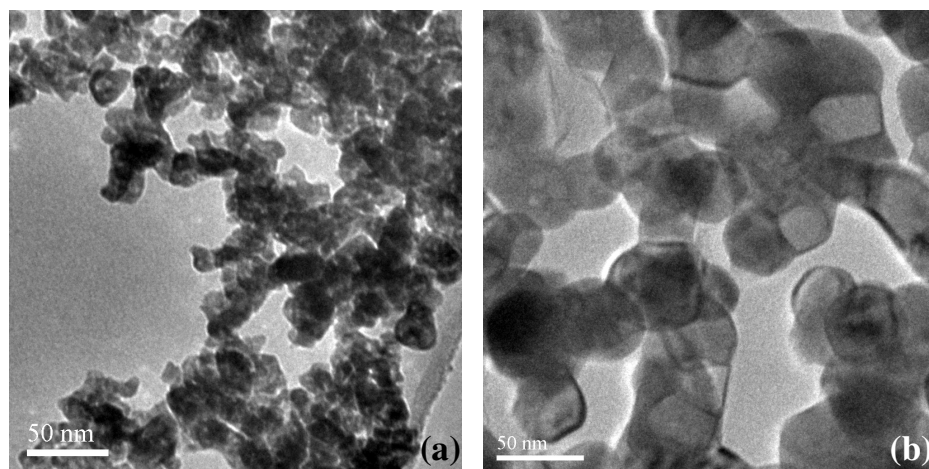


Figure 3.17: Transmission electron micrographs of the oxynitride nanoparticles ammonolyzed at (a) 800°C and (b) 1000°C.

The morphology of the particles was analyzed by transmission electron microscopy. Figure 3.17 shows TEM images of the samples reacted at 800°C (a) and 1000°C (b) with identical magnification. In both cases the particles exhibit spherical shapes. The typical particle size can be estimated as 10 nm for LaTiO₂N synthesized at 800 °C and 40-50 nm for the sample reacted at 1000 °C.

References

- [1] S. J. Clarke, B. P. Guinot, C. W. Michie, M. J. C. Calmont, M. J. Rosseinsky, *Chem. Mater.* 14 (2002) 288.
- [2] S. J. Clarke, K. A. Hardstone, C. W. Michie, M. J. Rosseinsky, *Chem. Mater.* 14 (2002) 2664.
- [3] F. Pors, P. Bacher, R. Marchand, Y. Laurent, G. Roul, *Rev. Int. Hautes Tempér. Réfract.*, Fr. 24 (1988) 239.
- [4] http://keison.co.uk/carbolite/carb21.htm?gclid=CM7E4uvv_5ACFR9paAodz3WHFQ. 2008.
- [5] http://www.nabertherm.de/produkte/details/en/waermebehandlung_2-kammeroefen-strahlungsbeheizung. 2008.
- [6] R. Marchand, F. Pors, Y. Laurent, *Revue Internationale des Hautes Temperatures et des Refractaires* 23 (1986) 11.
- [7] S. G. Ebbinghaus, A. Weidenkaff, A. Rachel, A. Reller, *Acta Crystallogr. C* 60 (2004) i91-i93.
- [8] F. Pors, P. Bacher, R. Marchand, Y. Laurent, G. Roul, *Rev. Int. Hautes Tempér. Réfract.*, Fr. 24 (1988) 239.
- [9] L. W. Tai, P. A. Lessing, *J. Mater. Chem.* 7 (1992) 502.
- [10] M. Kakihana, M. Yoshimura, *Bull. Chem. Soc. Jpn.* 72 (1999) 1427.
- [11] V. C. Albarici, PhD Thesis, UFSCar, Sao Carlos, Brazil (2004).
- [12] J. R. Sohn, Y. C. Kang, H. D. Park, *Jpn. J. Appl. Phys.* 41 (2002) 3006.
- [13] Y. Itoh, I. W. Lenggoro, S. E. Pratsinis, K. Okuyama, *J. Mater. Res.* 17 (2002) 3222.
- [14] S. Wohlrab, M. Weiss, H. Du, S. Kaskel, *Chem. Mater.* 18 (2006) 4227.
- [15] M. A. Flores-Gonzalez, G. Ledoux, S. Roux, K. Lebbou, P. Perriat, O. Tillement, *J. Solid State Chem.* 178 (2005) 989.

4. Oxynitride Perovskites as Pigments

In the last years most countries have created rules restricting the use of pigments containing toxic elements and/or heavy metals (e.g. Cd, Cr, Pb, Sb) to protect human health and the environment. Therefore the development of new inorganic pigments that are non-toxic and environmental friendly is a big challenge [1, 2, 3].

A number of interesting approaches have been published by various research groups. To name only a few examples, Flores *et al* obtained the pigment $\text{Co}_{0.05}\text{Zn}_{1.95}\text{SiO}_4$ with an intense blue color, which contains only 2.5% mol of cobalt [4]. Calbo *et al* minimized the Cr content and partially substituted Ni by Mg and Zn in the spinel black pigment $\text{Ni}(\text{Fe}, \text{Cr})_2\text{O}_4$ [5]. Furthermore Munoz *et al* minimized the amount of Cr in the green pigment formulation $\text{Cr}_{1.14}\text{Al}_{0.86}\text{O}_3$ [6]. Chromium (III) compounds do not show inherent toxicity but their use is being controlled because of the possibility of oxidation to Cr (VI), which is known to be a carcinogenic substance.

Following the necessity to develop eco-friendly dyes and pigments, oxynitrides are good candidates, since they show bright colors and do not contain toxic heavy metals [7-9]. Pérez-Estébanez *et al* studied the fluorite-type oxynitride Zr-Ln-O-N ($\text{Ln} = \text{Ce}, \text{Eu}$ and Er). The pigments based on europium were white, while the ones based on erbium showed a pink color. The compounds with cerium were orange and green, depending on the doping amount. They exhibit high-quality color properties such as intense coloration and high reflectance [10]. The optical properties of the oxynitride solid solution $\text{GaN}:\text{ZnO}$ were investigated by Maeda *et al*. The $(\text{Ga}_{1-x}\text{Zn}_x)(\text{N}_{1-x}\text{O}_x)$ compounds have yellowish color and show smaller band gap values than the pure end members GaN and ZnO. The absorption edges shift to longer wavelengths when the Zn content increases [11]. The system $\text{Ta}_{(3-x)}\text{Zr}_x\text{N}_{(5-x)}\text{O}_x$ was studied by Günther and Jansen. Pure Ta_3N_5 is dark red and with the introduction of $\text{Zr}^{4+}/\text{O}^{2-}$ in the crystal lattice the color changes from orange to yellow because of the substitution of the “softer” nitrogen atoms for the “harder” oxygen atoms [12]. In recent years oxynitrides based on the perovskite framework have also been investigated. For example Jansen and Letschert reported on the solid solution $\text{Ca}_{(1-x)}\text{La}_x\text{TaO}_{(2-x)}\text{N}_{(1+x)}$. Increasing values of x result in compounds with yellow,

orange and red colors. With this discovery the reddish pigments based on the problematic element cadmium may now possibly be substituted [13]. CdS is bright yellow and by substituting part of sulfur by selenium the color turns from orange to red. Cd(S,Se)-based pigments present bright colors as well as high thermal and chemical stability. These pigments themselves have a low solubility and are therefore non-toxic. Nevertheless, upon oxidation (e.g. during waste combustion) they turn into the highly toxic cadmium oxide. Cd-based pigments are nowadays practically forbidden in the European Union. But as can be seen in Figure 4.1, there is only one inorganic compound (ceramic pigment) for bright yellow and red color and they are based on cadmium. Therefore, there exists a high need for new bright yellow and red inorganic pigment. Rachel *et al* have reported on oxynitrides ABO_2N type ($A = Ca^{2+}$, Sr^{2+} , Ba^{2+} and $B = Ta^{5+}$, Nb^{5+}) [14]. The compounds exhibited different colors like yellow, orange, ochre and black, as shown at Figure 4.2.

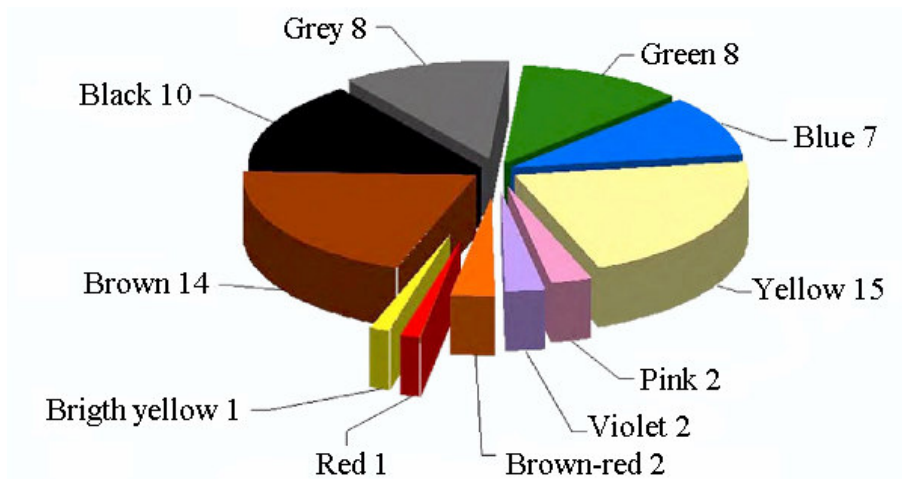


Figure 4.1: Chemically different systems for different colors (adapted from [15]).



Figure 4.2: Picture showing the colors of different compounds. Top line (from left to right): TiO_2 , TiO_xN_y , $CaTaO_2N$, Sr_2TaO_3N , $SrTaO_2N$, $NdTaO_2N$. Bottom line: $BaTaO_2N$, $EuTaON_2$, $LaTiO_2N$, $Yb_2Ta_2O_5N_2$, $SrTiO_3:N$ and $BaNbO_2N$.

In this chapter it will be demonstrated that changes in the cationic/anionic composition of complex oxynitrides result in different colors that cover a vast range of the visible light spectrum. This colors flexibility makes oxynitrides a promising class of ceramics for the production of pigments without toxic elements. Non-toxicity, bright color and thermal stability (discussed in the next chapter) are some of the prerequisites for a good pigment. Further requirements depend in which application the dye is going to be used. However, in general, the pigments should be chemically and environmentally stable, e.g. it should not react with the commodity where it is applied and should not degrade in contact with water or under sunlight. The pigment should also have a good covering power, i.e. a small quantity of dye should paint big areas. It is also desirable that the dye can be easily produced and has a reasonable price.

All oxynitrides discussed in this chapter were prepared by Pechini method (section 3.2.2) and ammonolyzed at 950-1000°C until pure phases were obtained in the x-ray diffraction patterns. The color CIELab (section 2.5) parameters of the various compounds are plotted in Figure 4.3. The axes in the 3D graphic are a^* (-) green, (+) red, b^* (-) blue (+) yellow and L^* (-) dark/black (+) light/white. The colors shown in the plot correspond to the respective $a^*b^*L^*$ -values of each sample. It is important to note that the different specimens show a big variety of colors as yellow, ochre, orange, red, green, light blue, brown, and black. Table 4.1 summarizes the color and the crystal structure of the studied samples.

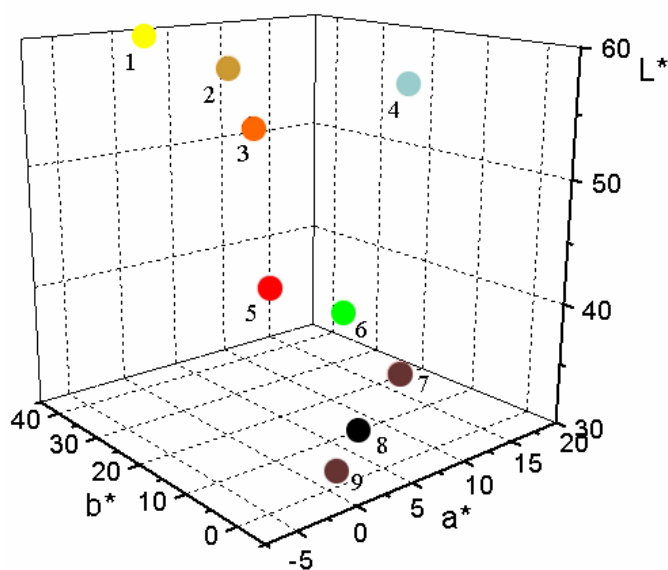


Figure 4.3: Colorimetric graphic of some oxynitride perovskite pigments: 1) CaTaO_2N , 2) $\text{CaZr}_{0.5}\text{Ta}_{0.5}\text{O}_{2.5}\text{N}_{0.5}$, 3) SrTaO_2N , 4) $\text{SrTiO}_3\text{:N}$, 5) BaTaO_2N , 6) $\text{Yb}_2\text{Ta}_2\text{O}_5\text{N}_2$, 7) LaTiO_2N , 8) BaNbO_2N and 9) SrNbO_2N .

There are three main ways to vary the color in oxynitride perovskite systems. The first is to vary the O/N ratio in $AB(O,N)_x$ compounds. A second method is co-substitution of the cations and anions as for example in $A_{1-x}A'_xBO_{3-x}N_x$. And finally, the A or B cations in ABO_2N perovskites can be varied while the O/N ratio is kept fixed.

Table 4.1: Color and corresponding space group for each studied sample.

Sample	Color	Crystal System	Space Group
CaTaO ₂ N	Yellow	Orthorhombic[16]	P n m a
SrTaO ₂ N	Orange	Tetragonal[16]	I 4 / m c m
BaTaO ₂ N	Red	Cubic[17]	P m $\bar{3}$ m
Yb ₂ Ta ₂ O ₅ N	Green	Cubic[18]	F d $\bar{3}$ m
CaZr _{0.5} Ta _{0.5} O _{2.5} N _{0.5}	Ochre	Orthorhombic[19]	P n m a
SrNbO ₂ N	Brown	Tetragonal[20]	I 4 / m c m
BaNbO ₂ N	Black	Cubic[17]	P m $\bar{3}$ m
SrTiO ₃ :N	Light blue	Cubic[21]	P m $\bar{3}$ m
LaTiO ₂ N	Brown	Triclinic[22]	I $\bar{1}$

As an example for the first approach Moriga *et al* [23] have studied the variation of nitrogen content in $LaTi(O_{1-x}N_x)_y$. The color (and the absorption edges) vary from yellow (2.56 eV) through green-yellow (3.17 eV) to light blue (3.44 eV) with the increase of x value, as plotted in Figure 4.4. Nitrogen is less electronegative than oxygen. The metal-nitrogen bonds therefore have a more covalent character than the corresponding metal-oxygen bonds. When oxygen is substituted by nitrogen the band gap decreases and the material starts to absorb light with lower energy. The charge neutrality of the compounds is achieved by formation of ionic vacancies.

The co-substitution approach was for example used by Jansen and Letschert [13] who demonstrated how a simultaneous exchange of Ca^{2+}/O^{2-} by La^{3+}/N^{3-} in $Ca_{(1-x)}La_xTaO_{(2-x)}N_{(1+x)}$ influences the color of perovskite oxynitrides (Fig. 4.5). When x has small values the compounds show light yellow colors while with increasing x the color gets darker passing through dark yellow, orange to red. By using cationic co-substitution it is possible to introduce much more nitrogen in the crystal structure than by anionic vacancies only. Consequently the cationic co-substituted oxynitride compounds show a broader color spectrum.

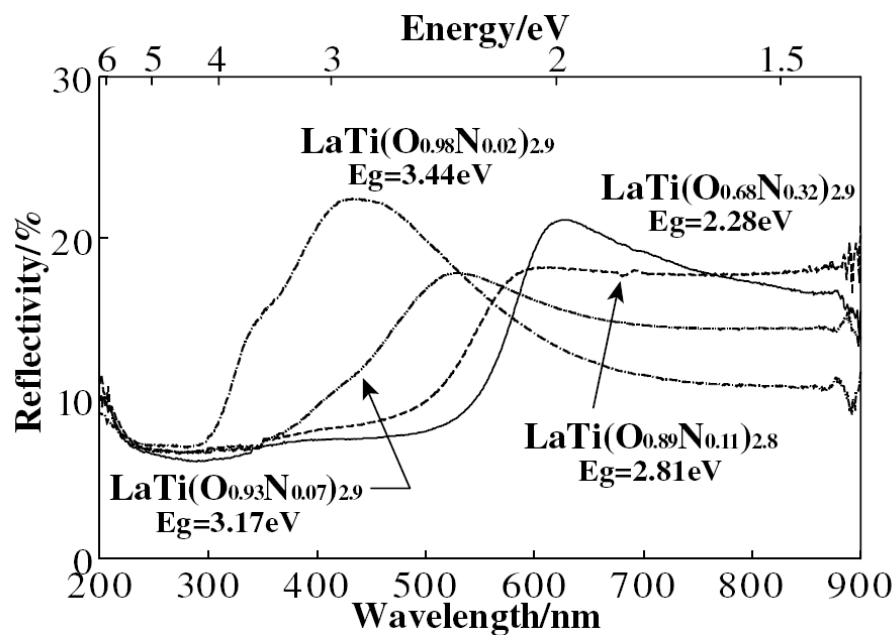


Figure 4.4: Diffuse reflectance spectra of $\text{LaTi}(\text{O}_{1-x}\text{N}_x)_y$ oxynitrides prepared by Moriga *et al.* The estimated band gaps (E_g) for each oxynitride are also given [23].

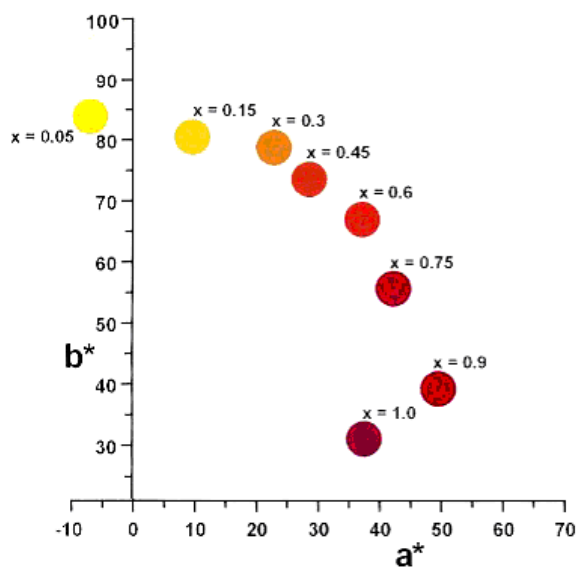


Figure 4.5: Colorimetry plot of $\text{Ca}_{(1-x)}\text{La}_x\text{TaO}_{(2-x)}\text{N}_{(1+x)}$ [13].

To extend these investigations, we have studied samples with identical nitrogen stoichiometry in order to investigate how modifications in the cationic sublattice control the pigment color.

Comparing samples with the general composition ABO_2N one can see that changes on the cationic sites of the oxynitride perovskites result in major color

variations. For example, in the tantalum oxynitrides $ATaO_2N$ the incorporation of A cation of different size but with the same formal charge (+2) leads to the following colors: $BaTaO_2N$ is red, $SrTaO_2N$ is orange, and $CaTaO_2N$ is yellow. This color change is correlated with a reduction of crystallographic symmetry. While $BaTaO_2N$ is cubic, the symmetry is reduced to tetragonal for $SrTaO_2N$ and finally $CaTaO_2N$ possess an orthorhombic unit cell. These crystallographic changes are common for perovskites and account for the smaller size of the A cation. The ionic radii of the A cation surrounded by 12 ions are 1.75 Å, 1.58 Å and 1.48 Å for Ba^{2+} , Sr^{2+} and Ca^{2+} , respectively [24]. The reduced radius of the A^{2+} cation leads to a shrinking of the averaged cell parameters of 4.111 Å, 4.034 Å, and 3.947 Å for $A = Ba^{2+}$, Sr^{2+} and Ca^{2+} , respectively. On the other hand, it is important to note that the tantalum–oxygen/nitrogen distances remain almost constant for these three compounds. In contrast to the bond lengths, the bond angles Ta–(O,N)–Ta strongly alter with the size of the A cations. The angles for the respective compounds are 180°, 169.9°, and 153.3°. The change in bond angles results in modifications of the overlap between the O/N-p and the metal-d orbitals, both for σ - and π -type bonds. A better overlap, i.e. bond angles closer to 180° is expected to result in a more covalent character of the transition metal-oxygen bond and in turn leads to a smaller band gap. It has lately been demonstrated both on the basis of experimental results and DFT calculations that the charge and electronegativity of the A cations has a negligible impact on the electronic structure of perovskite related oxides with d^0 configuration [25]. Nevertheless, a size mismatch of the A cation can cause a structural distortion, resulting in a bond angle value smaller than the 180° in the cubic perovskites. These smaller bond angles strongly influence the conducting band, which consists of antibonding π^* orbitals with dominating metal-d character. While the energetic position of the center of the conducting band remains almost unchanged, a reduced angle leads to a smaller conduction band *width*, in turn increasing the band gap as schematically shown in Figure 4.6. Reported band gap values for $ATaO_2N$ of 1.9 eV, 2.1 eV and 2.4 eV for $A = Ba$, Sr , and Ca , respectively, strongly support these considerations [26].

Another possibility to alter the color of oxynitrides is the substitution of the B cation. Good examples are the perovskite oxynitrides ABO_2N with pentavalent B cations. $SrTaO_2N$ (2.1eV) is orange, $SrNbO_2N$ has a brown (1.9eV) color. An

analogue behavior is found for Ca- and Ba-containing oxynitrides: CaTaO_2N (2.4eV) is yellow and CaNbO_2N (2.1eV) is ochre while BaTaO_2N (1.9eV) is red and BaNbO_2N (1.8eV) is black. For the respective niobates the absorption edge shifts to longer wavelengths compared to the tantalates, i.e. they have narrower band gaps. This effect cannot be explained by atomic bond distance values, since Nb^{5+} has the same ionic radius (0.78 Å) as Ta^{5+} in an octahedral coordination. The observed change in color can also not be elucidated by crystal symmetry, since the Ba-compounds are cubic ($Pm\bar{3}m$), the Sr-compounds are tetragonal ($I4/mcm$) and the Ca-compounds are orthorhombic ($Pnma$). The observed color changes most likely originate from different electronegativities of the B cations. For a more electronegative transition metal ion the corresponding t_{2g} -orbitals (which mainly contribute to the conducting band) are closer to the anionic 2p-orbitals leading to both narrower band gaps and more covalent B -O bonds.

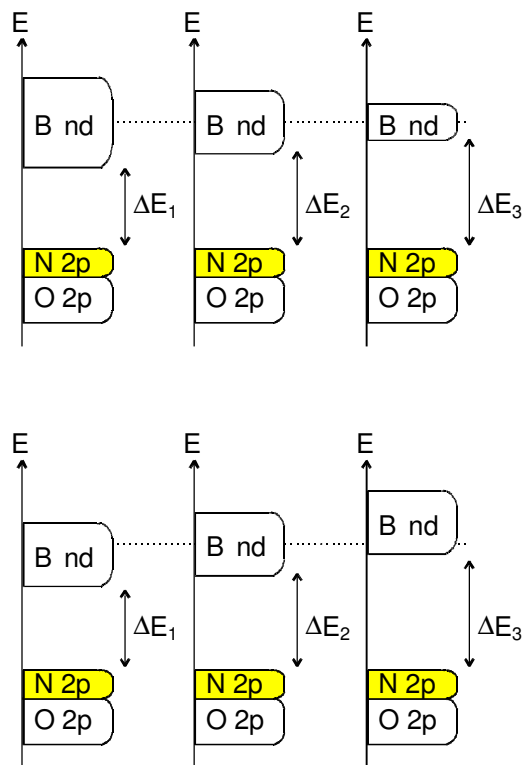


Figure 4.6: Schematic sketch of the influence of B - O - B bond angle (top) from left to right: decreasing from 180° to lower angle and of the electronegativity of the B cation (bottom) from left to right: decreasing electronegativity of the transition metal on the optical band gap in oxynitride perovskites.

This assumption can be confirmed comparing the ionicity of the atomic bonds for the different compounds. The ionicity of Ta-O and Nb-O bounds can be calculated using Pauling's formula:

$$I = 1 - e^{-\frac{(\chi_a - \chi_b)^2}{4}} \quad (4.1)$$

where χ_a and χ_b correspond to the electronegativities of the cation and anion, respectively [27]. The obtained ionicity values using Pauling's electronegativities are $I_{\text{Ta-O}} = 0.610$ and $I_{\text{Nb-O}} = 0.571$. The niobium–oxygen bond is therefore less ionic (more covalent) resulting in a light absorption at longer wavelengths compared to the respective tantalate compounds. This simple scenario has lately been confirmed for pure oxides possessing perovskite-related structures by band structure calculation [25]. The influence of different electronegativities of the *B* cations is schematically displayed in the lower part of Fig. 4.6. The choice of *B* cation has a minor effect on the width of the conducting band but strongly influences its energetic position, resulting in a strong decrease of the band gap with increasing covalence/electronegativity of the *B* cation.

In summary the exchange of cations results in strong changes in the colors of the oxynitride perovskites, opening the possibility to fine-tune the color by doping with small amounts of different cations. Based on very simple consideration, a systematic model for changes in the energetic position of the conducting band can be derived. Starting from a given material the band gap can be decreased by increasing the crystallographic symmetry (e.g. by adjusting the size of the *A* cation) or by increasing the electronegativity of the involved *B* cation. These relationships open the possibility to tailor the optical band gap of oxynitride perovskites.

References

- [1] J. Sokolowska-Gajda, H. S. Freeman, A. Reife, *Dyes Pigm.* 30 (1996) 1.
- [2] F. Fernández, C. Colón, A. Durán, R. Barajas, A. d'Ors, M. Becerril, J. Llopis, S. E. Paje, R. Sáez-Puche, I. Julián, *J. Alloys Compd.* 275–277 (1998) 750.
- [3] M. Trojan, P. Sulcová, P. Mosner, *Dyes Pigm.* 44 (2000) 161.
- [4] A. Fores, M. Llusar, J. A. Badenes, J. Calbo, M. A. Tena, G. Monros, *Green Chem.* 2 (2000) 93.
- [5] J. Calbo, S. Sorli, M. Llusar, M. A. Tena, G. Monros, *Br. Ceram. Trans.* 103 (2004) 3.

- [6] R. Munoz, N. Masó, B. Julián, F. Márquez, H. Beltrán, P. Escribano, E. Cordoncillo, *J. Eur. Ceram. Soc.* 24 (2004) 2087.
- [7] J. Grins, G. Svensson, *Mater. Res. Bull.* 29 (1994) 801.
- [8] R. Marchand, F. Pors, Y. Laurent, *Ann. Chim. Fr.* 16 (1991) 553.
- [9] F. Tessier, R. Marchand, *J. Solid State Chem.* 171 (2003) 143.
- [10] M. Pérez-Estébanez, R. Pastrana-Fábregas, J. Isasi-Marín, R. Sáez-Puche, *J. Mater. Res.* 21 (2006) 1427.
- [11] K. Maeda, T. Takata, M. Hara, N. Saito, Y. Inoue, H. Kobayashi, K. Domen, *J. Am. Chem. Soc.* 127 (2005) 8286.
- [12] E. Guenther, M. Jansen, *Mat. Res. Bull.* 36 (2001) 1399.
- [13] M. Jansen, H. P. Letschert, *Nature* 404 (2000) 980.
- [14] A. Rachel, S. G. Ebbinghaus, M. Güngerich, P. J. Klar, J. Hanss, A. Weidenkaff, A. Reller, *Thermochim. Acta* 438 (2005) 134.
- [15] www.ferro.com. 2008.
- [16] E. Günther, R. Hagenmayer, M. Jansen, *Z. Anorg. Allg. Chem.* 626 (2000) 1519.
- [17] Y.-I. Kim, P. M. Woodward, K. Z. Baba-Kishi, C. W. Tai, *Chem. Mater.* 16 (2004) 1267.
- [18] F. Pors, R. Marchand, Y. Laurent, *J. Solid State Chem.* 107 (1993) 39.
- [19] J. Grins, G. Svensson, *Mat. Res. Bull.* 29 (1994) 801.
- [20] S. G. Ebbinghaus, A. Weidenkaff, A. Rachel, A. Reller, *Acta Crystallogr. , Sect. C* 60 (2004) i91-i93.
- [21] J. Hutton, R. J. Nelmes, *J. Phys. C: Solid State Phys.* 14 (1981) 1713.
- [22] S. J. Clarke, B. P. Guinot, C. W. Michie, M. J. C. Calmont, M. J. Rosseinsky, *Chem. Mater.* 14 (2002) 288.
- [23] T. Moriga, D. Aoki, Y. Nishida, K. Kitaji, K. Takahara, K. Murai, Nakabayashi I., *Phys. Sta. Sol. (a)* 203 (2006) 2818.
- [24] R. D. Shannon, C. T. Prewitt, *Acta Cryst. B* 25 (1969) 925.
- [25] H. W. Eng, P. W. Barnes, B. M. Auer, P. M. Woodward, *J. Solid State Chem.* 175 (2003) 92.
- [26] F. Cheviré, F. Tessier, R. Marchand, *Eur. J. Inorg. Chem.* 2006 (2006) 1223.
- [27] J.-H. Choy, D.-K. Kim, S.-H. Hwang, G. Demazeau, D.-Y. Jung, *J. Am. Chem. Soc.* 117 (1995) 8557.

5. Thermal Oxidation of Oxynitride Perovskites

Pigments may be exposed to elevated temperatures during their application, therefore it is important to know the temperature at which the corresponding compounds start to decompose [1]. The decomposition temperature is useful to decide whether a pigment can be applied, for example as colorants for papers, thermoplastics, rubbers, ceramics, enamels, etc. The analysis of the gases that evolve from the samples submitted at high temperatures (e.g. during combustion) is also important because toxic species may be formed. At room temperatures all the studied oxynitride samples were found to be stable in air, water and in concentrated acids. Their stability at high temperature, on the other hand, varies a lot depending on the *A* and *B* cation in the general formula ABO_2N , as will be shown in this chapter.

The oxide precursors for the studied compounds $SrNbO_{3.5}$ and $SrTaO_{3.5}$ were prepared by conventional solid-state (chapter 3.2.1) while $LaTiO_{3.5}$ was obtained by the Pechini method (chapter 3.2.2). The ammonolysis of the three oxides was done in a tube furnace with an ammonia flow of 25 ml/min. $SrNbO_2N$, $SrTaO_2N$ and $LaTiO_2N$ were obtained at 950°C (54h), 1000°C (36h) and 950°C (36h), respectively. The oxidation reactions of the oxynitrides were carried out in the range of 25–1200°C with a heating rate of 10°C/min in Ar/O₂ mixtures with O₂ contents varying between 0-20% and flow of 40 ml/min. A NETZSCH STA 409C thermobalance connected to a Balzers QMG quadrupole mass spectrometer by a skimmer coupling system (chapter 2.8) was used for the experiments.

When heated in synthetic air all compounds showed a similar reaction behavior as can be seen in Figure 5.1. Between room temperature and approximately 400°C a small reduction of weight is observed, resulting from the loss of absorbed water and CO₂. This effect is most obvious for $LaTiO_2N$ and by far less pronounced for the other compounds. The loss of water is followed by a strong increase in weight. This increase is considerably higher than the expected value for the reaction $2ABO_2N + 1.5O_2 \rightarrow 2ABO_{3.5} + N_2$. After reaching a maximum the sample weights slowly re-decrease in a region of a few hundred degree Celsius. Finally, a sharp weight loss is observed and the oxides $ABO_{3.5}$ are formed. A number of studies have been performed to explain the unexpected intermediate weight gain during oxidation. It was found that some nitrogen stays retained in the completely oxidized structure, forming intermediate dinitrogen-containing compounds as $B \cdots N \equiv N$ and $B \cdots N \equiv N \cdots B$

or metal-nitrogen intermediate compounds as $B\equiv N$ [2, 3]. On the other hand, thermogravimetric measurements coupled with mass spectroscopy revealed that already during the weight increase considerable amounts of N_2 are released [4]. At higher temperatures nitrogen is completely detached and the weight decreases to its final value. The temperature at which the oxynitrides start to decompose/oxidize (i.e. the samples weight starts to increase) varies among the different compounds. $LaTiO_2N$ starts to decompose already at $350^\circ C$, while $SrNbO_2N$ is stable up to $410^\circ C$ and $SrTaO_2N$ starts to decompose only at $450^\circ C$.

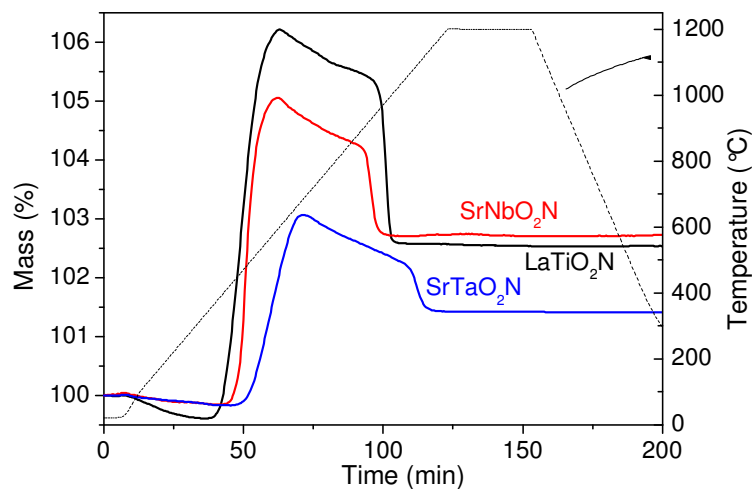


Figure 5.1: Thermogravimetric analysis of $SrNbO_2N$, $LaTiO_2N$ and $SrTaO_2N$ in synthetic air.

To the best of our knowledge, all previous oxidation studies on perovskite oxynitrides were done in air while no systematic investigations on the influence of the oxygen content on the reaction mechanism were performed so far. Recently, Logvinovich *et al* reported the thermal decomposition of $LaTiO_2N$ in He [5] and Rachel *et al* investigated the oxidation of $SrNbO_2N$ under 20% and 1% of O_2 [4]. While the reaction in 20% oxygen showed the described oxidation curves, a completely different behavior was found in an atmosphere with 1% O_2 . The intermediate reaction product was not observed, but the weight increased progressively up to ca. $920^\circ C$ where a small sudden weight loss was found. Finally, the reaction finished with the expected mass corresponding to $SrNbO_{3.5}$. This significantly different behavior was the motivation to study systematically the thermal oxidation of oxynitride perovskites when submitted to heat treatment under atmospheres with different oxygen concentrations, namely between 0 and 20% O_2 .

Mass spectrometry (MS) analyses were done for the following molar masses: 15, 16, 17, 18, 28, 29, 30, 44 and 46. For the sake of clearness only the masses related to nitrogen elimination i.e. 28 (N₂) and 30 (NO) are shown in the Figures 5.3, 5.5, and 5.8. The other masses were monitored to cross check if the obtained results were exclusively related to nitrogen-containing gases. As an example, $m/e = 28$ could be attributed either to N₂ or to CO evolving during the reaction. The same m/e signal could also be due to CO₂ fragmenting in the mass spectrometer to CO + O. In the latter case the $m/e = 28$ signal would be accompanied by a far more intense signal for $m/e = 44$. Thus, if specific peaks appear for the molar masses 28 and 44, it follows that it is not N₂ but CO₂ evolving from the sample. CO and N₂, on the other hand, can be distinguished by their isotope patterns i.e. the intensity ratio $m/e = 28/29/30$. In the CO case, small intensities at $m/e = 16$ and $m/e = 29$ are detected, which eliminate the suspicion if the MS 28 signal in fact corresponds to N₂. In a similar manner, CO₂ and NO₂ (both $m/e = 46$) can be separated since CO₂ has its main peak at MS 44. These examples illustrate the necessity to compare the signals of different masses to confirm which molecules are evolving during the reaction.

Species with $m/e = 17$ and 15 were measured to verify if NH₃ was released during the reactions, but none of the samples showed peaks at these masses (except for signals corresponding to the mass 18, which indicates H₂O). It can therefore be concluded that nitrogen is not eliminated as ammonia during the heat treatment in any of the studied atmospheres. Although the compounds were stored at 120°C prior to the measurements, all samples show small signals in the MS 18 channel between 200-300°C and MS 44/46 between 150-750°C, corresponding to the release of water and CO₂, respectively, both being chemically bonded to the sample. As an example in Fig. 6.2 the MS spectra of SrNbO₂N heated in 5% of oxygen in argon is plotted. The water peak appears at ca. 220°C, while the CO₂ signal has a broad first peak between 220-480°C followed by a more intense peak, which disappears at 670°C. The presence of chemically bonded water and carbonate was attributed to traces of H₂O and CO₂ in the ammonia gas. It can be minimized by cooling the samples not in ammonia but changing the atmosphere to high-purity nitrogen at high temperatures [6].

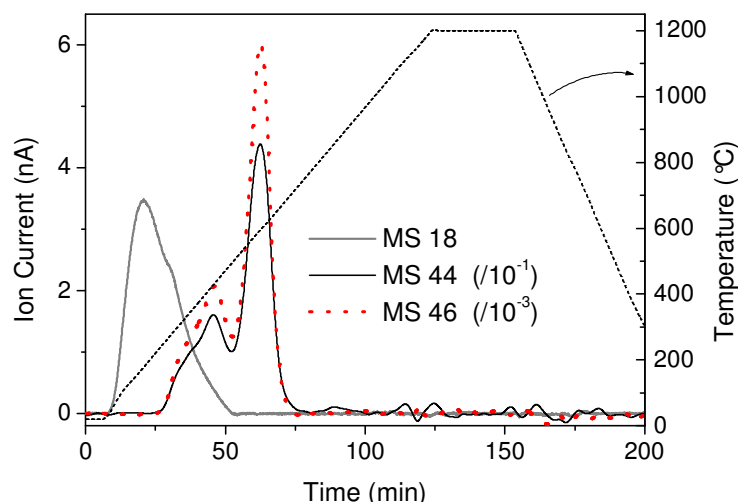


Figure 5.2: $m/e = 18(\text{H}_2\text{O})$, 44 and 46 (CO_2) signals of SrNbO_2N reacted in an atmosphere of 5% O_2 in argon.

Results of the thermogravimetric analyses of SrNbO_2N in varying oxygen contents are plotted in Figure 5.3. The top panel gives the weight change during reaction while the lower two panels show the ion currents for two selected m/e values, namely 28 and 30. It is apparent that for oxygen concentrations between 3% and 20% the behavior of the TG curves is quite similar: At a temperature of roughly 440°C the weight starts to increase. After passing through a maximum the weight slowly decreases and then in a relatively sharp temperature interval of 915°C – 960°C drops to a value of 102.5% of the initial mass. $\text{SrNbO}_{3.5}$ was identified as final reaction product by XRD (Figure 5.4). The observed weight gain does not match the expected value of 4.41% because the sample loses water and carbon dioxide during the heating treatment as shown in Fig. 5.2. This effect partially compensates the weight gained by oxidation. The intermediate weight maximum is found because during a certain temperature regime the fully oxidized compound retains parts of the nitrogen. The retained nitrogen is bonded as N_2 -molecule in the structure $(\text{SrNbO}_{3.5}(\text{N}_2)_x)$ as first found by Le Gendre *et al* using thermogravimetry, Raman spectroscopy and O/N analysis [3]. It is important to note that already at the beginning of the oxidation, SrNbO_2N starts to lose molecular nitrogen as evidenced by the pronounced $m/e = 28$ signal found in the MS spectra at 480°C . This indicates that only part of the nitrogen remains bonded in the oxide structure. After the weight reaches its maximum, the N_2 evolution rate decreases strongly, leading to a slight weight change and a reduction of the MS 28 signal.

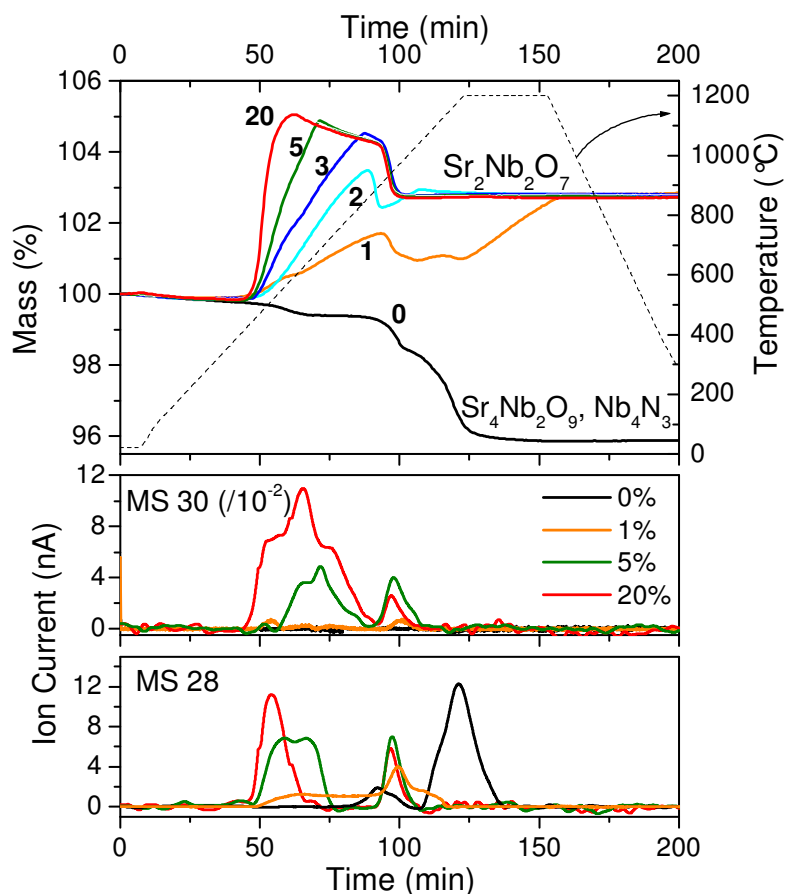


Figure 5.3: Thermogravimetric and Mass Spectrometry curves for $SrNbO_2N$ heated in atmospheres with different oxygen concentrations (the analysis in 0.5% O_2 is discussed in the text but not shown because it took 2h at 1200 °C to complete the reaction).

Finally, at approximately 950°C the remaining N_2 molecules are abruptly detached and the weight reaches the final value. The simultaneous oxygen assimilation and N_2 loss (between 440-960°C) explains the differences in weight gain observed for different oxygen contents. The lower the O_2 concentration, the higher is the required temperature for the sample to become completely oxidized while at the same time N_2 is successively released. As a consequence the maximum achieved weight becomes smaller with lower O_2 content and is reached at higher temperatures.

It is furthermore interesting to note that although the largest part of the nitrogen is released as N_2 , small amounts of NO were also detected (middle panel of Figure 5.2). When heated in 20% O_2 , the onset of the oxidation is accompanied by the formation of small quantities of NO ($m/e = 30$). At the weight maximum an additional peak for NO was found. During the plateau the NO evolution rate decreases to yield a final smaller maximum at 950°C when the residual fraction of N_2 is released as well.

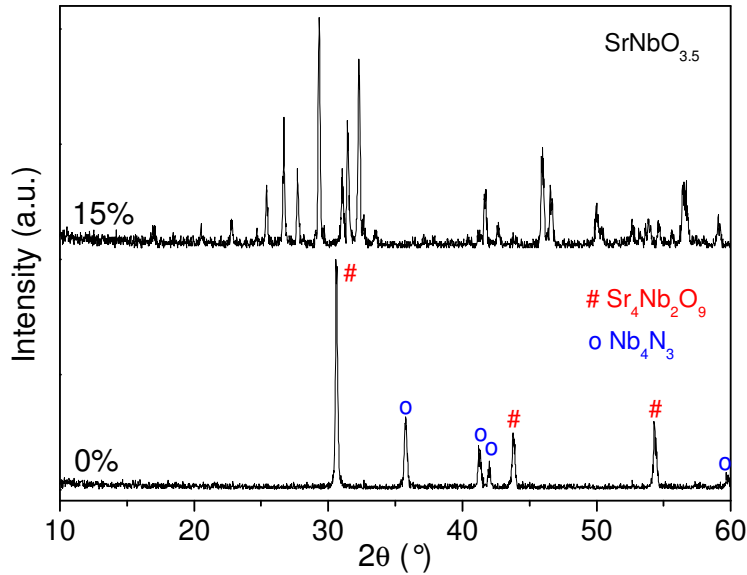


Figure 5.4: X-ray diffraction patterns for SrNbO₂N after the TG/MS experiments under 0% and 15% O₂.

The formation of NO is probably due to the presence of nitrogen species that are bonded in the perovskite structure, which react with O₂ and form NO instead of recombining to N₂. This interpretation is based on the fact that the temperatures at which NO is formed are too low for the reaction of N₂ with O₂. The NO molecules must therefore be built by reactions of more reactive nitrogen species during the reoxidation. Although the sensitivity of the mass spectrometer is not completely identical for the various masses, a comparison of the ion currents (10^{-9} and 10^{-11} for $m/e = 28$ and 30 respectively) clearly indicates that the largest part of nitride ions form N₂ while the formation of nitrogen monoxide is only a side reaction. The occurrence of NO is a quite interesting finding since until now the studies of the thermal oxidation behavior of oxynitride perovskites have only reported the evolution of N₂. In contrast to the NO signal, the MS 44 peaks (NO₂) always showed the same behavior as the ones of MS 46, indicating that no NO₂ is formed, independently of the oxygen percentage. Upon decreasing the oxygen content to 5%, the first NO peaks become significantly smaller. Obviously the lower O₂ concentration only allows a reaction at higher temperatures.

For 0.5% and 1% O₂ the TGA curves reveal a different reaction behavior than the one described above. Since in these atmospheres the O₂ concentration becomes too low for the samples to be completely oxidized below 950°C, the N₂ detaches

earlier than the total oxidation occurs. In that case, the reaction apparently happens in three different stages:

- 1st Formation of $\text{SrNbO}_x(\text{N}_2)_y$ ($2 < x < 3.5$, $y \leq \frac{1}{2}$): some oxygen reacts with the oxynitride sample (weight increase) within a broad temperature range and simultaneously a constant small amount of N_2 is detached, leading to the plateau observed in the MS 28 signal between 470-870°C.
- 2nd Formation of SrNbO_x ($2 < x < 3.5$): N_2 is detached from the sample, the weight goes abruptly down and a sharp peak appears in the MS 28 signal at the same temperature as for the other measurements (ca. 950°C). A very small quantity of NO also evolves from the sample at this temperature.
- 3rd Oxidation to $\text{SrNbO}_{3.5}$: the oxygen uptake continues and the final product is obtained after 30 minutes at 1200°C.

For SrNbO_2N reacted in 0.5% O_2 , the reaction time of 30 min at 1200°C was not sufficient to complete the oxidation. It was necessary to heat the sample almost 2 hours at 1200°C to get the same weight increase as for the other runs. Nevertheless, the weight increase started at roughly the same temperature as for the higher oxygen concentrations and the weight drop at 950°C was also found. It can therefore be concluded that the temperature at which the oxynitrides start to oxidize (around 440°C) and the one at which the retained N_2 is completely detached (950°C) are independent of the oxygen content in the atmosphere.

For zero percent O_2 (pure argon atmosphere) SrNbO_2N showed a completely different thermal behavior. The sample only loses weight, reaching a final value of 95.5% of the initial mass. This finding is not surprising, since there is no oxygen to react with the sample. A small N_2 peak accompanied by a step in the TG signal appears at the characteristic temperature of 950°C. It is worth mentioning, that in oxygen-free atmosphere the evolution of N_2 already starts at a slightly lower temperature of 870°C. The most intense N_2 signal occurs between 1060°C and 1200°C, thus at a much higher temperature than for the reactions in oxygen containing atmospheres. This peak corresponds to the TG signal revealing a weight loss of 2.6 % in this temperature region. No NO peaks were observed, which is understandable since there is no oxygen to form nitrogen monoxide. As final reaction products, the two phases $\text{Sr}_4\text{Nb}_2\text{O}_9$ and Nb_4N_3 were detected by XRD as shown in Fig. 5.4. Evidently, in an oxygen-free atmosphere, nitrogen is not completely released as N_2

but a part of it remains, forming the reduced binary nitride Nb_4N_3 . On the other hand, not the entire niobium becomes reduced but parts of it remain as Nb^{5+} in $\text{Sr}_4\text{Nb}_2\text{O}_9$. A quantitative phase analysis by Rietveld refinement yielded a molar mixture of 70% $\text{Sr}_4\text{Nb}_2\text{O}_9$ and 30% Nb_4N_3 . This composition is very close to the expected ratio of 67% to 33%. The corresponding theoretical weight loss of 2.4% does not agree very well with the experimentally found value of 3.6%, probably because some CO_2 evolves together with N_2 from the sample. The weight loss corresponding to the phase decomposition was measured only after the plateau at approx. 820°C. The first step at the thermogravimetric curve therefore very likely results from the evolution of water and carbon dioxide as discussed for Fig. 5.2.

The thermogravimetric and mass spectroscopic analyses of LaTiO_2N are depicted in Fig. 5.5. LaTiO_2N shows a quite similar behavior to SrNbO_2N . When the sample is reacted in atmosphere with oxygen concentrations higher than 1%, the weight starts to increase at ca. 380°C, and at 960°C drop rapidly to the final value. Nitrogen ($m/e = 28$) is released at ca. 400°C, where a small peak appears and at 960°C the most intense peak occurs for all the atmospheres. Small NO peaks ($m/e = 30$) were found at 270°C for all reaction gases as shown in the middle panel of Figure 5.5. The reactions in 2-20% O_2 also lead to the elimination of NO between 470-820°C and at 970°C. The intensities of these signals increase with the O_2 concentration. Furthermore, the evolution of CO_2 (MS 44 and 46) has been detected between 60-420°C for all atmospheres. Only the TGA run in 20% O_2 shows a different behavior. It yields two additional comparatively intense peaks at 650°C and 960°C, as shown in Figure 5.6. Because no related signals were found for $m/e = 44$, these two peaks correspond to the formation of NO_2 . The quantity of NO and NO_2 eliminated during the studies were two orders of magnitude smaller than N_2 , what means that only ca. 1% of the total evolution of nitrogen is in oxide form. It is possible that for this high oxygen concentration nitrogen is not only oxidized to NO but also to NO_2 . It is interesting to note that in contrast to SrNbO_2N , an evolution of NO_2 is observed for LaTiO_2N . Under 0.5 and 1% O_2 , LaTiO_2N shows generally the same behavior as SrNbO_2N . Both compounds start to oxidize between 380-440°C, but they keep some N_2 in the structure. The remaining N_2 is released at 960°C, and the oxidation continues until 1200°C. All TGA experiments in atmospheres containing at least small amounts of oxygen lead to the same weight gain and resulted in $\text{La}_2\text{Ti}_2\text{O}_7$ as reaction product, as shown in the XRD pattern in Fig. 5.7.

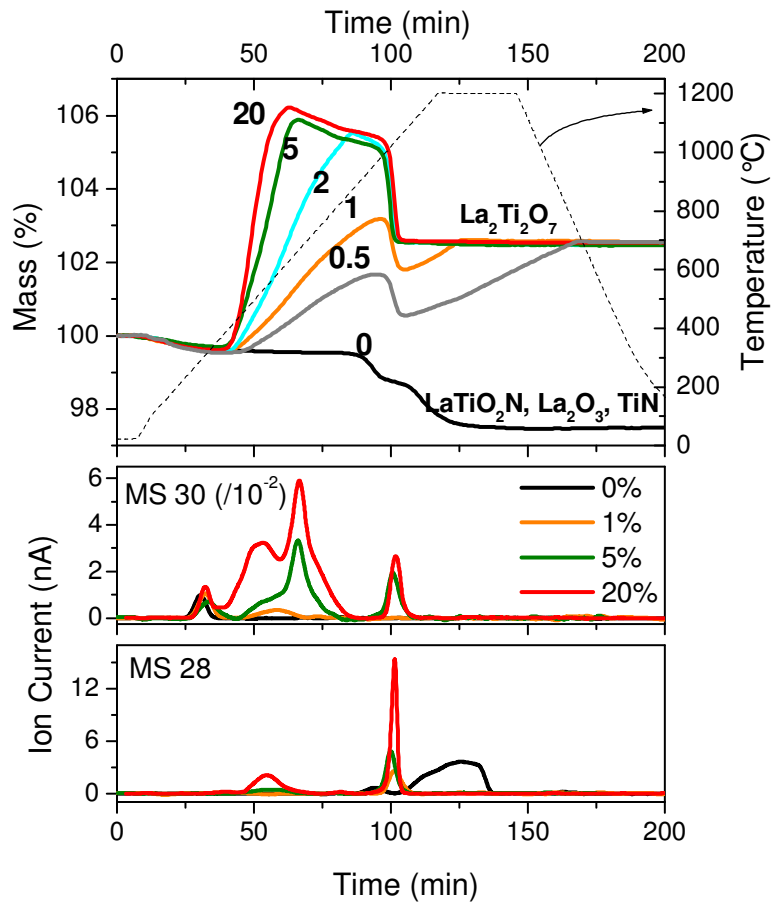


Figure 5.5: Thermogravimetric and mass spectrometry curves for LaTiO₂N heated in atmospheres with different oxygen concentrations.

The total weight gain of 2.6% does not match with the expected value of 4.3%. As explained above, this is because the sample also loses water and CO₂, which partly compensates the weight gain during oxidation. The evolution of these two gases can already be detected by a small loss between room temperature and 400°C. When LaTiO₂N is heated in pure argon (0% O₂) it only shows weight decrease steps, leading to 97.5% of the original mass. The first step in the TGA curve corresponds to water and carbon dioxide evolution, and the second step corresponds to the decomposition of the oxynitride perovskite as confirmed by the MS 28 signal. N₂ starts to detach at 970°C and is completely eliminated only at 1200°C. A very small NO evolution is also observed at 270°C, most likely at this low temperature only NO molecules that were simply superficially bonded to the sample are eliminated. The final product was composed of 76% LaTiO₂N, 14% La₂O₃ and 10% TiN as determined by Rietveld refinement of the respective XRD.

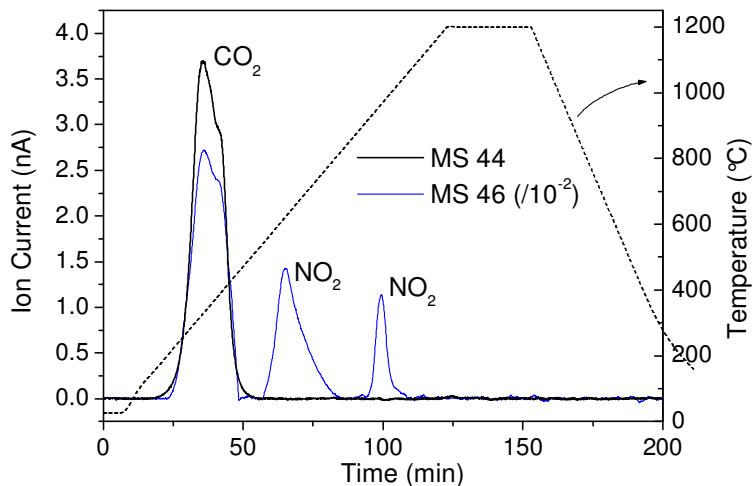


Figure 5.6: $m/e = 44$ and $m/e = 46$ signals for LaTiO_2N reacted under 20% O_2 .

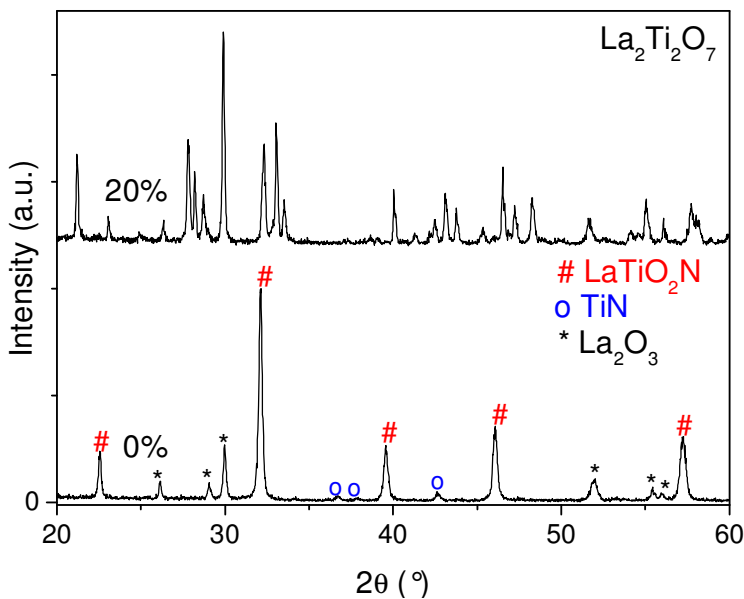


Figure 5.7: X-ray diffraction patterns for LaTiO_2N samples after thermal investigation in atmospheres with 0% and 20% O_2 .

The calculated weight loss of 1.7% is in good agreement with the measured value of 1.4% in the second step of TGA the curve. It is interesting to note that in contrast to SrNbO_2N , which is completely decomposed under the same reaction conditions, for LaTiO_2N 76% of the oxynitride is still stable after 30 minutes at 1200°C . Also the reaction products are different. In addition to the binary nitride TiN containing the transition metal in a reduced oxidation state, the binary oxide La_2O_3 is formed while for SrNbO_2N a complex oxide ($\text{Sr}_4\text{Nb}_2\text{O}_9$) was found. In an earlier

report Logvinoch *et al* [5] studied the thermal stability of LaTiO_2N under oxygen-free He atmosphere. Also in this gas the oxynitride reacted to La_2O_3 and TiN but together with a perovskite-type phase of unknown composition.

The thermogravimetric analysis of SrTaO_2N showed a quite different behavior compared to both SrNbO_2N and LaTiO_2N . Depending on the oxygen concentration in the gas phase, the reactions result in different final weight changes as depicted in Fig. 5.8. The XRD patterns shown in Fig. 5.9 prove a different chemical composition of the reaction products.

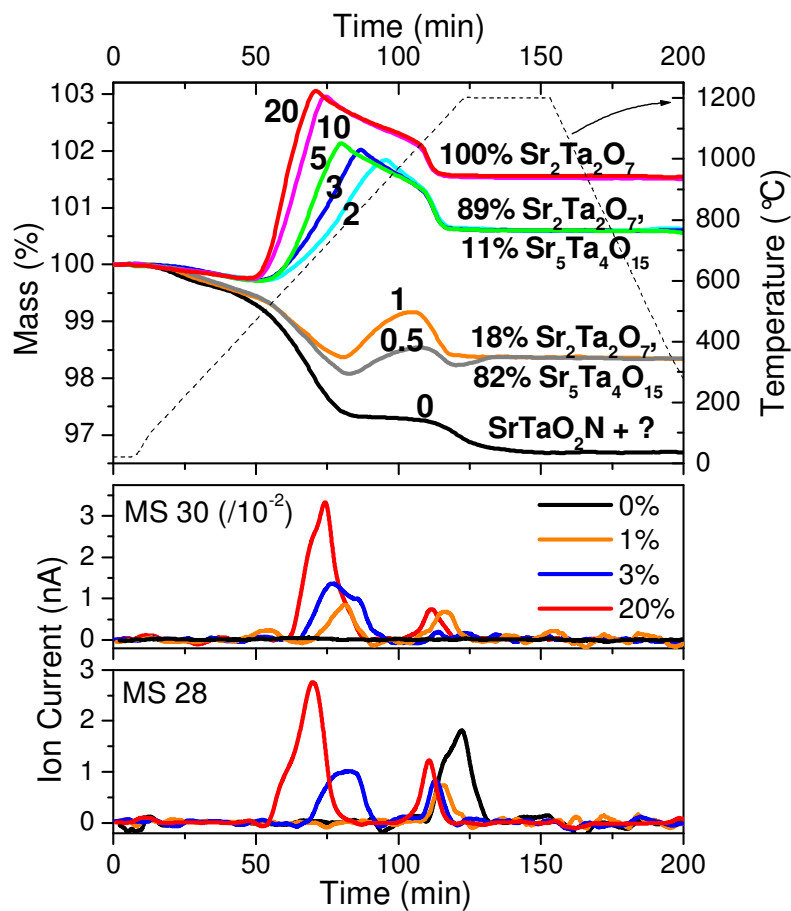


Figure 5.8: Thermogravimetric and mass spectrometry curves for SrTaO_2N heated in atmospheres with different oxygen concentrations.

When the samples is reacted under 10-20% O_2 it starts to oxidize at 480°C , as detected by the weight increase in the TGA curves. As for the other two compounds, the weight reaches a maximum and starts to decrease slowly. At 1050°C the weight goes sharply down to the final value. N_2 and a minor amount of NO (ca. 1% of total

N₂) evolve from the sample at approximately the same temperatures, first between 540-720°C and second at 1070°C. The obtained oxidized phase is pure Sr₂Ta₂O₇ as was verified by x-ray diffraction. The total weight gain value of 1.7% is significantly lower than the expected 3.2%. As already discussed this discrepancy is due to the release of water and CO₂. All thermogravimetric investigations of SrTaO₂N showed a peak in the MS channel 18 between 60 – 370°C corresponding to H₂O evolution and a broad peak between 270 – 870°C for m/e = 44 and 46, due to the release of CO₂.

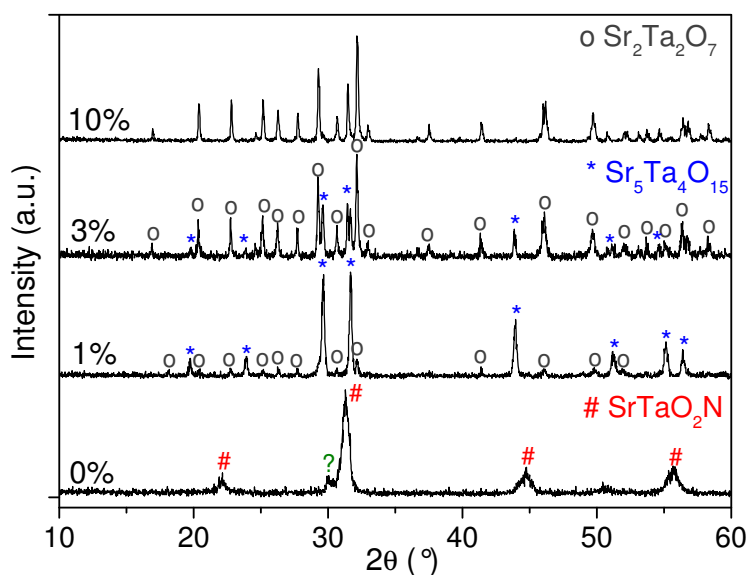


Figure 5.9: X-ray diffraction patterns for SrTaO₂N samples after thermogravimetry in gas atmospheres with 0%, 1%, 3% and 10% O₂.

For 2-5% O₂ the first steps of the reaction are similar to the above described behavior, only the maximum weight value is smaller than for higher oxygen percentages. The N₂ and NO evolutions occur simultaneously, but at slightly higher temperatures than for the aliquots reacted under 10-20% O₂. A broad peak appears for m/e = 28 and 30 between 670-840°C and the next peak is at 1100°C. The final weight was 100.7% of the initial mass. The Rietveld analysis showed that the obtained phases were 89% Sr₂Ta₂O₇ and 11% Sr₅Ta₄O₁₅.

For 0.5 and 1% O₂ the samples start to lose weight at 60°C, corresponding to H₂O and CO₂ elimination as discussed above (Fig. 5.2). At ca. 790°C the weight starts to slightly re-increase and at 1050°C it decreases to reach a final value of 98.4%. A small amount of NO is eliminated between 740-820°C and at 1120°C, while the N₂

peak appears only at 1120°C. The obtained products were the same as found for 2-5% oxygen. Only the ratio varied: 18% $\text{Sr}_2\text{Ta}_2\text{O}_7$ and 82% $\text{Sr}_5\text{Ta}_4\text{O}_{15}$.

For 0% O_2 the reaction is characterized by two steps in the TG. The first weight loss corresponds to water and carbon dioxide elimination while the second is due to dinitrogen evolution as evidenced by the N_2 peak between 1120-1200°C observed for $m/e = 28$. A formation of nitrogen monoxide was not observed. The obtained final weight was 96.5% of the initial mass. The resulted compounds were SrTaO_2N and a second phase, which could not be identified. As shown in the XRD pattern in Figure 5.9, the main peak of this phase appears at $2\theta = 30.2^\circ$. The color of the reacted powder was dark orange with black particles. This indicates that the second phase besides SrTaO_2N contains Ta in a reduced oxidation state. It is worth mentioning that SrTaO_2N remains relatively stable in oxygen-free atmosphere, even after being submitted to 1200°C for 30 minutes. For both the obtained oxide phases ($\text{Sr}_2\text{Ta}_2\text{O}_7$ and $\text{Sr}_5\text{Ta}_4\text{O}_{15}$) tantalum remains in its highest oxidation state, i.e. as Ta^{5+} . It could be expected that for smaller oxygen amounts the final products would contain some reduced tantalum but this is apparently not the case. In contrast to $\text{Sr}_2\text{Ta}_2\text{O}_7$, which possesses a layered perovskite structure, $\text{Sr}_5\text{Ta}_4\text{O}_{15}$ is a hexagonal perovskite with cationic vacancies and can be written as $\text{Sr}_5\text{Ta}_4\Box\text{O}_{15}$ [7]. Its oxygen/cation ratio is 1.67 while for $\text{Sr}_2\text{Ta}_2\text{O}_7$ it is 1.75. Thus, it can be one explanation for the formation of $\text{Sr}_5\text{Ta}_4\text{O}_{15}$ under atmospheres with low oxygen content. The results of mass spectroscopy analysis for the three oxynitride samples are summarized at Table 5.1.

In summary the three studied samples have shown remarkable differences in the thermal behavior when heated in pure argon. SrNbO_2N completely decomposes into $\text{Sr}_4\text{Nb}_2\text{O}_9$ and Nb_4N_3 while for LaTiO_2N ca. 76% of the original oxynitride remained. The rest of the material decomposed in La_2O_3 and TiN . SrTaO_2N was considerably stable and only a small quantity of a second phase (which could not be identified) was formed. When oxygen was present in the atmosphere SrNbO_2N and LaTiO_2N were completely oxidized to the respective oxides $\text{ABO}_{3.5}$ while SrTaO_2N formed $\text{Sr}_5\text{Ta}_4\text{O}_{15}$ and $\text{Sr}_2\text{Ta}_2\text{O}_7$, depending on the oxygen concentration. For all investigated oxynitrides the evolution of N_2 and NO showed a similar behavior, while for LaTiO_2N also NO_2 was released. In this thesis NO and NO_2 were identified for the first time as additional reaction products however in a much lower concentration than N_2 . It could be shown that the studied oxynitrides are thermally stable up to roughly

400°C even in air. Therefore they can be used as pigments in all applications where lower temperatures occur. When protected from oxygen, they can be even used at much higher temperatures for example as glazes for ceramics. Upon high temperatures (during fire or waste combustion) in oxidizing atmospheres, the oxynitrides react to harmless products like indissoluble oxides and N₂. The amount of NO_x released from the samples is very small (app. 1% of the total N-content) so these materials can be considered as non-toxic not only during use, but also in their disposal.

Table 5.1: Summary of the results from the mass spectroscopy analysis listing the temperature ranges in which the specific gases were released and the m/e values used to identify them.

% O ₂	MS	Temperature (°C)		
		SrNbO ₂ N	LaTiO ₂ N	SrTaO ₂ N
All atmospheres	18 (H₂O)	90-490	240-460	60-370
	44 + 46 (CO ₂)	220-480, 670	60-420	270-870
0	28 (N₂)	870-950, 1060-1200	970-1200	1120-1200
	30 (NO)	---	270	---
1	28 (N₂)	470-1150	400, 960	1120
	30 (NO)	950	270	740-820, 1120
5	28 (N₂)	450-710, 950	400, 960	670-840, 1100
	30 (NO)	540-890, 950	270, 470-820, 970	670-840, 1100
20	28 (N₂)	440-680, 950	400, 960	540-720, 1070
	30 (NO)	440-900, 950	270, 400-820, 970	540-720, 1070
	Only 46 (NO ₂)	---	650, 960	---

References

- [1] R. Aguiar, D. Logvinovich, A. Weidenkaff, A. Rachel, A. Reller, S. G. Ebbinghaus, *Dyes Pigm.* 76 (2008) 70.
- [2] R. Marchand, F. Pors, Y. Laurent, *Rev. Int. Hautes Tempér. Réfract.*, Fr. 23 (1986) 11.
- [3] L. Le Gendre, R. Marchand, B. Piriou, *Eur. J. Solid State Inorg. Chem.* 34 (1997) 973.
- [4] A. Rachel, S. G. Ebbinghaus, M. Güngerich, P. J. Klar, J. Hanss, A. Weidenkaff, A. Reller, *Thermochim. Acta* 438 (2005) 134.
- [5] D. Logvinovich, A. Börger, M. Döbeli, S. G. Ebbinghaus, A. Reller, A. Weidenkaff, *Prog. Solid State Chem.* 35 (2007) 281.
- [6] D. Logvinovich, L. Bocher, D. Sheptyakov, R. Figi, S. G. Ebbinghaus, R. Aguiar, A. Reller, A. Weidenkaff, in preparation.
- [7] R.M. Mitchell, *Perovskites: Modern and Ancient*, Almaz Press Inc. (2002) 119-124.

6. The System $\text{Sr}_{(1-x)}\text{La}_x\text{Ti}(\text{O},\text{N})_3$

6.1 Polycrystalline Samples: Crystal Structure Refinement

Polycrystalline samples of the series $\text{Sr}_{(1-x)}\text{La}_x\text{Ti}(\text{O},\text{N})_3$ were first synthesized by Wang *et al* [1]. The doping level was $x \leq 0.05$. These authors demonstrated that lanthanum and nitrogen co-doped SrTiO_3 is a better photocatalyst for the decomposition of NO than the pure SrTiO_3 . Chevire *et al* [2] studied this system in the whole composition range $0.10 \leq x \leq 1.00$. The colors of the samples vary from green, orange, red to brown with increasing x value. To the best of our knowledge the crystal structures of the oxynitrides of this series have not yet been reported. Only the end members SrTiO_3 and LaTiO_2N have been studied. In 1991 Marchand *et al* [3] analyzed the structure of LaTiO_2N using x-ray diffraction. An orthorhombic unit cell with space group Pnma was found. Ten years later Clarke *et al* [4] re-investigated the structure of LaTiO_2N using powder neutron diffraction. In contrast to the earlier work a more distorted perovskite structure with space group $\text{I}\bar{1}$ was reported, with statistical N/O distribution on the different anionic sites. The advantage of neutron diffraction compared to x-ray diffraction is that oxygen and nitrogen can be distinguished (as explained in chapter 2.2) and distortions in the unit cell due to anion displacements can be detected. The other end member of the series, SrTiO_3 has the typical perovskite cubic structure with $a = 3.898\text{\AA}$ and crystallizes in space group $\text{Pm}\bar{3}\text{m}$ [5].

In this section the Pechini synthesis of $\text{Sr}_{(1-x)}\text{La}_x\text{Ti}(\text{O},\text{N})_3$ with $x = 0, 0.25, 0.50, 0.75$ and 1 , and its crystal structure refinements are described. The starting materials were lanthanum nitrate hexahydrate ($\text{La}(\text{NO}_3)_3 \cdot 6\text{H}_2\text{O}$), strontium nitrate ($\text{Sr}(\text{NO}_3)_2$) and titanium (IV) isopropoxide ($\text{C}_{12}\text{H}_{28}\text{O}_4\text{Ti}$). Citric acid was used as chelating agent, with a ratio citric acid:metal ions of 2:1. In the first step titanium citrate was formed by dissolving titanium (IV) isopropoxide in an aqueous solution of citric acid under constant stirring at 70°C during approximately 4 hours, until a clear solution formed. The Ti^{4+} concentration was 0.42 mol/L . To this solution stoichiometric quantities of $\text{Sr}(\text{NO}_3)_2$ and $\text{La}(\text{NO}_3)_3 \cdot 6\text{H}_2\text{O}$ were slowly added and the mixture was kept at 70°C until the reagents were completely dissolved. The solution was dried in a hot plate at 120°C , and the organic part was burned out at 650°C in air within 3 h. Around 2 g of an amorphous white powder were obtained. The powder was ammonolyzed in a rotating quartz tube furnace at 900°C ($x = 0$) and 950°C ($x =$

0.25, 0.5, 0.75 and 1) under an ammonia gas flow of 25 ml/min. The ammonolysis was done in periods of 24 h with intermediate grinding and the obtained products were analyzed by XRD. The ammonolysis was stopped when pure oxynitride phases were obtained. The necessary reaction time for $x = 0, 0.25, 0.5, 0.75$ and 1 were 24 h, 168 h, 168 h, 48 h and 72 h, respectively.

According to the x-ray diffraction patterns all analyzed samples possess the cubic perovskite structure while neutron diffraction revealed considerable structural deviations. The data obtained by neutron diffraction were refined using the program FullProf (chapter 2.3) to solve the space group of these oxynitride phases and to reveal the nitrogen quantity in each sample. The structures of all compounds were refined in different space groups typically observed for perovskites. Starting with the cubic archetype ($Pm\bar{3}m$) passing through tetragonal ($I4/mcm$), orthorhombic ($Pnma$) and finishing with a triclinic model ($I\bar{1}$). To decide which model fits the measured neutron diffraction data best, the parameters that describe the difference between the measured and the calculated data, i.e. profile factor (R_p), weighted profile factor (R_{wp}), and χ^2 , were compared. The model that gave smallest values was chosen. The results for best fits are shown in Table 6.1. The bond distances are only listed for the titanium-nitrogen/oxygen octahedra because these bonds have the larger influence on the oxynitride properties such as color and electrical conductivity. $SrTi(O,N)_3$ has the same cubic structure as the parent oxide $SrTiO_3$ ($Pm\bar{3}m$), but it shows a slightly bigger cell parameter. This finding is expected since the ionic radius of N^{3-} (1.71 Å) is bigger than the O^{2-} (1.40 Å) [6]. It is evident that an increasing of the La^{+3}/N^{3-} doping leads to distortions of the unit cell. The composition $x = 0.25$ crystallizes in a tetragonal structure ($I4/mcm$) while the samples $x = 0.5$ and 0.75 show orthorhombic cells ($Pnma$). For $x = 1$ ($LaTiO_2N$) two possible symmetries were obtained: orthorhombic and triclinic. The refinement in the triclinic space group resulted in smaller values of R_p , R_{wp} and χ^2 than for the orthorhombic structural model, but it is expectable since more parameters were refined. On the other hand, both refinements yielded almost the same values for axes of the unit cell and the angle distortion from 90° is only ca. 0.2%. It is therefore not possible to unambiguously decide with model gives the exact structure of $LaTiO_2N$.

Table 6.1: Refined unit cell values, atomic positions, displacement parameters (Biso), χ^2 , R_{wp} , R_p , O/N ratio and TiN percentage for the $Sr_{(1-x)}La_xTi(O,N)_3$ series.

x value	x = 0	x = 0.25	x = 0.5	x = 0.75	x = 1	x = 1	
$a_p, \text{\AA}$	3.911	3.916	3.910	3.939	3.945	3.945	
Space group	$Pm\bar{3}m$	I4/mcm	Pnma	Pnma	Pnma	$I\bar{1}$	
$a, \text{\AA}$	3.91104(9)	5.5395(3)	5.5392(4)	5.5628(3)	5.5711(3)	5.5711(3)	
$b, \text{\AA}$	3.91104(9)	7.8291(7)	7.8398(6)	7.8559(6)	7.8675(6)	7.8643(6)	
$c, \text{\AA}$	3.91104(9)	5.5395(3)	5.5071(4)	5.5935(4)	5.6040(3)	5.6040(4)	
α, deg	90	90	90	90	90	90.255(6)	
β, deg	90	90	90	90	90	89.86(1)	
γ, deg	90	90	90	90	90	89.94(1)	
La/Sr	x	0.50000	0.00000	0.00000	0.00000	0.00000	0.5032(7)
	y	0.50000	0.50000	0.25000	0.25000	0.25000	0.25000
	z	0.50000	0.25000	0.00000	0.00000	0.00000	0.00000
	Biso	0.81(3)	0.54(3)	1.07(5)	1.01(4)	1.13(4)	1.22(6)
Ti ₁	x	0.00000	0.00000	0.00000	0.00000	0.00000	0.00000
	y	0.00000	0.00000	0.00000	0.00000	0.00000	0.00000
	z	0.00000	0.00000	0.00000	0.00000	0.00000	0.00000
	Biso	0.66(4)	0.38(4)	0.24(5)	0.17(6)	0.02(6)	0.11(3)
Ti ₂	x	-	-	-	-	-	0.00000
	y	-	-	-	-	-	0.50000
	z	-	-	-	-	-	0.00000
	Biso	-	-	-	-	-	0.11(3)
O ₁ /N ₁	x	0.50000	0.00000	0.50000	0.50000	0.50000	-0.0574(5)
	y	0.00000	0.00000	0.25000	0.25000	0.25000	0.25000
	z	0.00000	0.25000	0.0225(6)	0.0538(4)	0.0592(4)	0.014(1)
	Biso	0.86(2)	1.004(1)	1.7(2)	1.3(1)	1.2(1)	1.15(6)
O ₂ /N ₂	x	-	0.7680(2)	0.25000	0.25000	0.25000	0.264(1)
	y	-	0.2680(2)	0.0168(3)	0.0272(2)	0.0314(3)	0.027(1)
	z	-	0.00000	0.75000	0.75000	0.75000	0.235(1)
	Biso	-	0.85(2)	1.21(8)	1.55(8)	1.707(8)	2.5(1)
O ₃ /N ₃	x	-	-	-	-	-	0.25000
	y	-	-	-	-	-	0.4700(2)
	z	-	-	-	-	-	0.75000
	Biso	-	-	-	-	-	1.2(1)
Ti-O ₁ /N ₁ (\AA)		1.95553 (5)	1.9573(2)	1.9637(2)	1.9869(4)	1.9946(4)	1.9933(6)
Ti-O ₂ /N ₂ (\AA)		-	1.9636(2)	1.9569(2)	1.9837(2)	1.9909(3)	1.9900(6)
Ti-O ₃ /N ₃ (\AA)		-	-	-	-	-	1.9880(7)
R_{wp}		7.96	9.27	10.9	10.1	10.4	9.9
R_p		10.7	11.6	14.6	12.2	11.6	11.1
χ^2		1.61	1.97	2.35	2.25	3.33	2.95
TiN(%)		0	1.48	1.30	4.30	0.11	0.15
O/N		2.95/0.05(3)	2.68/0.32(3)	2.24/0.75(3)	2.15/0.85(3)	1.93/1.07(3)	1.95/1.05(8)

In the second line of Table 6.1 for the samples with $x > 0$ the calculated cell parameter for the idealized cubic structure is given:

$$a_p = \left(\frac{a}{\sqrt{2}} + \frac{c}{\sqrt{2}} + \frac{b}{2} \right) \cdot \frac{1}{3} \quad (6.1)$$

Using these values the size of the different unit cells can be compared. It was found that increasing the $\text{La}^{+3}/\text{N}^{-3}$ content leads to an expansion of the unit cell, although Sr^{+2} (1.44 Å) is larger than La^{+3} (1.36 Å). Apparently, the smaller size of the La^{+3} is overcompensated by the effect of the nitride ions. For all the composition nitrogen is homogeneous distributed in the structure.

Except for the composition $x = 0$, the samples show small quantities of TiN as second phase in the neutron diffraction patterns. This impurity could not be detected by x-ray diffraction because of the few amount present in the compounds. Cheviré *et al* [2] had assumed the presence of TiN as second phase in their samples based on the fact that the compounds with high Sr^{+2} content showed a black-green shade, which was attributed to the presence of a small quantity of reduced Ti^{+3} , but they could not confirm their assumption.

The notation $\text{La}_{1-x}\text{Sr}_x\text{TiO}_{2+x}\text{N}_{1-x}$ proposed by Cheviré *et al* [2] has to be modified for the samples studied in this chapter. Since the end member of the series, i.e. $\text{SrTiO}_3\text{:N}$, contains 1.7% of N in its structure and the other compositions have higher nitrogen contents than the stoichiometric formula. The higher nitrogen content could be explained because there are at least two different processes happening during the nitration: Simultaneous cationic/anionic substitution and oxygen vacancies formation.

Combining these two mechanisms the compounds present higher nitrogen content than the idealized formula proposed by Cheviré *et al*. It was reported by Logvinovich *et al* [7] that LaTiO_2N has a higher N content when synthesized by a soft chemistry approach compared to the products from the solid-state reaction. This may be one explanation for the higher nitrogen content in the studied compounds compared to the samples reported in Ref. [2], which were synthesized by solid-state reaction.

The BET surface areas of the samples are plotted in Figure 6.1. The oxide precursors have values varying from 22 to 49 m²/g while after reaction with NH₃ the specific surface areas decrease to 11-17 m²/g. This feature was expected since during ammonolysis the compounds are submitted to high temperatures leading to a sintering of the particles.

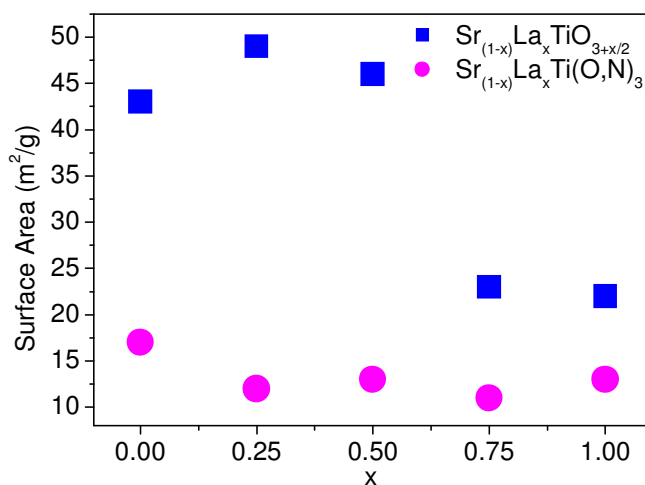


Figure 6.1: Comparison of the surface areas of the oxide and oxynitride samples.

After ammonolysis the powders present different colors. LaTiO₂N is brown, x = 0.75 dark olive, x = 0.50 and 0.25 green and x = 1 light blue. Figure 6.2 shows the UV-vis spectra for the samples measured in reflectance modus as described in chapter 2.4. All compounds have two broad absorption bands with minima varying between 600 nm (x = 1) to 540 nm (x = 0). The absorption at high wavelengths (> 600 nm) can be associated to small amounts of Ti³⁺ present in the compounds as the second phase TiN. Another minimum in the ultra violet region at approximately 380 nm is observed for the samples x = 0 and 0.25 while it is less pronounced to x = 0.5. This edge could correspond to the absorption edge of SrTiO₃. The band gap of the oxynitride samples was calculated by the Kubelka-Munk equation (considering direct band gap transition) and is plotted in Figure 6.3. As expected the band gap decreases with increasing x (La³⁺/N³⁻ amount). For SrTiO₃:N the decrease in the band gap is of 0.3 eV compared with the oxide SrTiO₃ that shows a band gap value of 3.2 eV. The band gap of LaTiO₂N is in agreement with the previous reported values of around 2 eV.

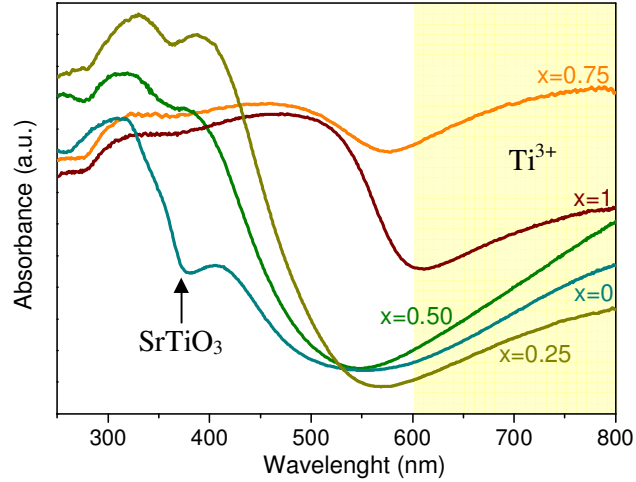


Figure 6.2: Absorbance curves for the oxynitride powders for wavelength between 250 nm and 800 nm.

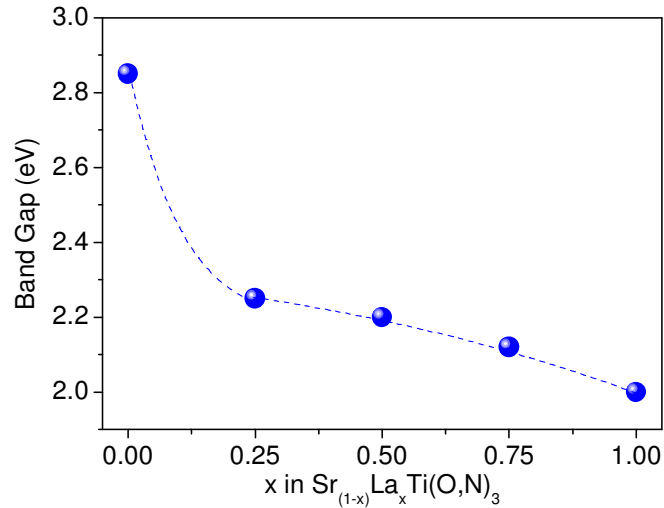


Figure 6.3: Band gap values for the synthesized oxynitride samples.

In summary, samples of $\text{Sr}_{(1-x)}\text{La}_x\text{Ti}(\text{O},\text{N})_3$ with $0 \leq x \leq 1$ have been synthesized by ammonolysis of oxide precursors from the Pechini method. With this technique it was possible to introduce more nitrogen in the perovskite structure than expected using the stoichiometric formula $\text{La}_{1-x}\text{Sr}_x\text{TiO}_{2+x}\text{N}_{1-x}$. The band gap of the samples is shifted to smaller values with increasing $\text{La}^{3+}/\text{N}^{3-}$ amount and their color shadow gets darker, starting with light blue for $x = 0$ passing through green and finishing with brown for $x = 1$. The structures of compounds get less symmetric with increasing $\text{La}^{3+}/\text{N}^{3-}$ amount starting with a cubic space group ($\text{Pm}\bar{3}\text{m}$) for $x = 0$, passing through tetragonal (I4/mcm) for $x = 0.25$, orthorhombic (Pnma) for $x = 0.5$,

0.75. For the composition $x = 1$ it was not possible to decide between orthorhombic and the triclinic model because both system gave similar refinement results.

6.2 Thin Films

For many technical applications, such as in microelectronics, flat panels displays, hard and corrosion resistant coatings, solar cells, etc it is indispensable to use thin films. Oxynitride thin films are an attractive class of functional materials since the introduction of nitrogen into the oxide sublattice often results in unexpected and interesting properties. Especially, the transition metal oxynitride films show unusual electrical and optical properties and sometimes have surprising superior performances compared to the corresponding pure oxide and nitride compounds [8]. As an example, the hardness of ZrO_xN_y thin films is around 33 GPa, while ZrN and ZrO_2 show values of 25 GPa and 9 GPa, respectively [9]. Another example are TiN_xO_y thin films, which present various adjustable colors like yellow-pink, gold, blue and gold-brown while TiO_2 and TiN films are transparent and dark gold, respectively [10]. Oxynitride thin films have been tested in a wide range of electronic, optoelectronic devices and gas sensors. Among the titanium based oxynitrides the most studied system is TiO_xN_y [10-13]. There are also some reports on ternary oxynitride films containing titanium, such as Zn-Ti-O-N, a new colored layer for solar technologies [14], Zr-Sn-Ti-O-N, a potential dielectric material for DRAM application [15], Ti-Si-O-N as copper diffusion barrier in integrated circuits [16] and Li-Ti-O-N as insulator material [17]. The research on thin oxynitride layers containing more than one (transition) metal is a relatively new topic. In many cases reactive sputtering has been employed for the preparation of such films [8, 16, 18, 19]. In addition, other synthesis techniques as chemical deposition [20, 21] and pulsed laser deposition [22] have already been successfully employed to prepare bi-cationic oxynitride layers [23, 24].

Thin films of $(Sr,La)TiO_{3\pm\delta}$ show metal-insulator transitions, depending on the oxygen concentration and in turn the titanium oxidation state [25-28]. Because of the pronounced effect of the anionic composition in this system it is interesting to introduce nitrogen and study the structural and physical properties of the formed oxynitride compounds. The end members of the series, $LaTiO_2N$ and $SrTiO_3:N$ have already been prepared by reactive plasma sputtering and by pulsed reactive crossed

beam laser ablation, respectively [29, 30]. In this section the syntheses of $\text{Sr}_{(1-x)}\text{La}_x\text{Ti}(\text{O},\text{N})_3$ thin films by spin coating and pulsed laser deposition are discussed.

Thin films were spin-coated (SC) by dropping a small quantity of $\text{Sr}_{(1-x)}\text{La}_x\text{Ti}(\text{O},\text{N})_3$, $x = 0, 0.25, 0.50, 0.75$ and 1 polymeric precursor solution produced by Pechini Method (section 6.1) onto the SrTiO_3 (STO) substrate. The viscosity of the solutions was adjusted to a final value of $5 \text{ mm}^2/\text{s}$ by controlling the water contents. Rotation speed and spin time were fixed to 6000 rpm and 30 s, respectively. After deposition the films were dried at 120°C on a hot plate for 20 min to remove residual solvents. Afterwards the films were heated to 400°C with a heating rate of $5^\circ\text{C}/\text{min}$ and kept at this temperature for 2 hours to burn out the organic matrix. This process was repeated six times to obtain a reasonable thickness of around 400 nm. Afterwards, the films were ammonolyzed. Figure 6.4 shows a scheme of the spin coating method.

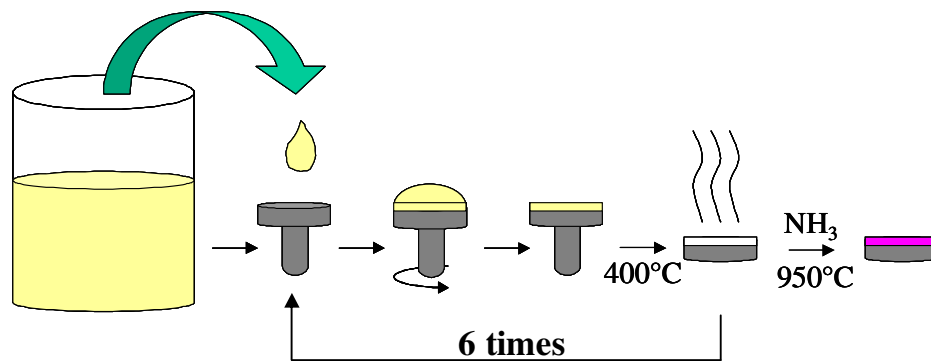


Figure 6.4: Scheme of the spin coating technique for the synthesis of thin films.

In an alternative approach the thin films were also grown by pulsed laser deposition (PLD) on STO and MgO substrates. Targets of $\text{Sr}_{(1-x)}\text{La}_x\text{TiO}_{3+x/2}$, $x = 0, 0.25, 0.50, 0.75$ and 1, were synthesized by calcination of the dried soft chemistry solution at 600°C . The obtained amorphous powders were pressed into pellets of 13 mm diameter and approximately 15 mm length. The pellets were sintered at 1300°C for 12 h in air to prepare the polycrystalline oxide targets (ca. 85 % of the theoretical density) used for ablation. A KrF excimer laser (Lambda Physic LPX 300) was employed to grow the films. The laser beam energy was 800 mJ and 20000 pulses with a repetition rate of 8 Hz were accumulated for each film. The pressure inside the chamber was kept at 1mbar of N_2 . With this pressure the best plasma plume size was

achieved, e.g. perpendicular to the target the plume was covering the entire substrate. The PLD chamber is schematically shown in Figure 6.5. The substrate was kept at 800°C during the ablation. Because of its minimal mismatch in the lattice parameters, SrTiO₃ (100) ($a = 3.905 \text{ \AA}$) was first used as substrate. To investigate the substrate influence on the properties of the films they were also grown on MgO (100) ($a = 4.213 \text{ \AA}$).

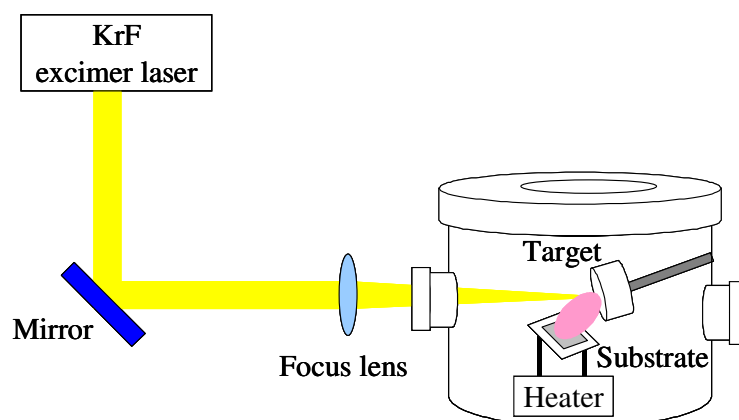


Figure 6.5: Illustration of a pulsed laser deposition chamber.

Subsequent the films (both by SC and PLD) were treated in ammonia atmosphere (flow of 25 mL/min) at 950°C for 3 h in a tube furnace. The used heating rate was 5°C/min. After the 3 hours of reaction the furnace was switched off and allowed to cool down. Gas atmosphere was changed from ammonia to nitrogen when the temperature reached 250°C. For comparison, oxide films were synthesized in air using the same heating program.

After the ammonolysis, the spin coated thin films presented different colors as orange ($x = 1$), yellow ($x = 0.75$), green ($x = 0.5$ and 0.25) and blue ($x = 0$). Figure 6.6 is photograph of the oxynitride films. As can be seen the films are quite homogeneous. The lighter spots visible on the surface of the films were caused during SIMS and SEM analyses. As discussed for the polycrystalline samples (Chapter 4), the difference in color is due to the nitrogen content variation and the cationic size discrepancy/ionicity that have direct influence on the band gap width. The color of the PLD films changed from colorless to greenish after the ammonolysis. The color shadow of the PLD films cannot be surely described, because they have been glued on the heater using silver paint during the ablation. The used substrates were both side

polished, what caused the silver on the back of the substrate to influence the color shadow of the films.

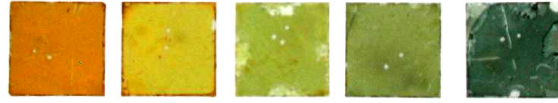


Figure 6.6: Photograph of the colored $\text{Sr}_{(1-x)}\text{La}_x\text{Ti}(\text{O,N})_3$ thin films produced by spin coating deposition. From left to right: $x = 1, 0.75, 0.5, 0.25$ and 0 .

X-ray diffraction (chapter 2.1) was used to investigate the orientational relationships between substrate and films. All the oxynitride films were measured in both configurations grazing angle and $\theta/2\theta$. But the x-rays results are better visualized for the SC in grazing angle configuration while for the PLD films were the $\theta/2\theta$ configuration. The grazing angle configuration minimizes the contribution of substrate peaks in the diffraction pattern. On the other hand the contribution of the diffraction peaks of the films that are epitaxially grown on the substrate are also minimized. Figure 6.7 shows that the spin coated oxynitride films have the perovskite structure.

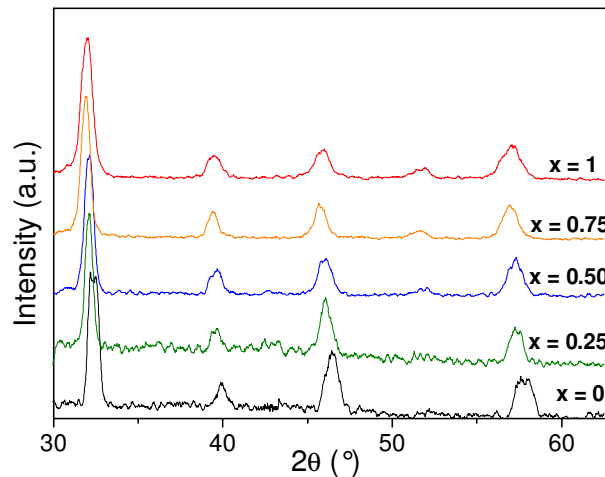


Figure 6.7: X-ray diffraction pattern of $\text{Sr}_{(1-x)}\text{La}_x\text{Ti}(\text{O,N})_3$ spin coated oxynitride thin films.

No indications for impurity phases were found. All peaks correspond to the perovskite phase (ABO_2N) are presented in the diffraction patterns and the relative intensity of the peaks are comparable to the powder x-ray diffraction pattern. These results show that the films have no preferential orientation. In contrast, from the diffraction patterns of the PLD films shown in Figure 6.8 (a) it can be concluded that these films grow epitaxially to the (100) direction of SrTiO_3 .

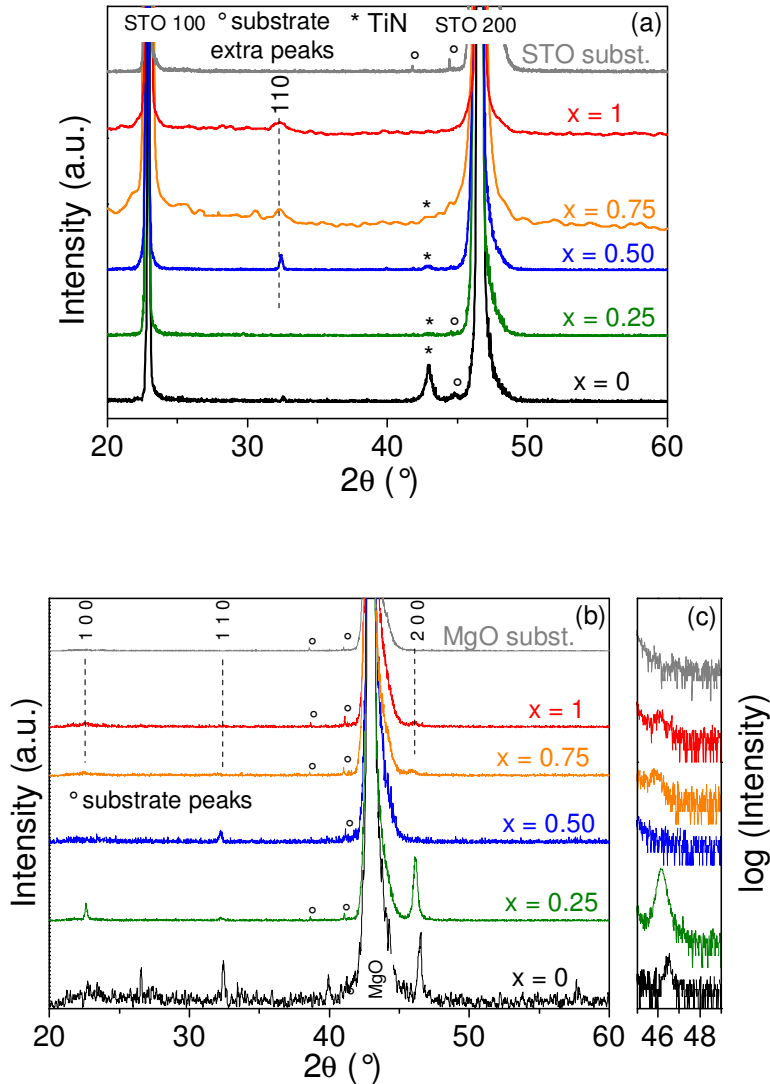


Figure 6.8: X-ray diffraction pattern of the PLD oxynitride thin films grown on: (a) STO, (b) MgO and (c) zoom of the region around 46.2° on MgO substrate showing the (200) cubic perovskite growth direction.

Because of their very similar cell parameters it is not possible to separate the peaks of the substrate and the films. The absence of additional peaks, on the other hand, indicates a high orientation of the films. For the compositions $x = 0, 0.5, 0.75$ and 1, a reflection at 32.4° was observed, in accordance with a (110) growth direction. For some compositions small extra-peaks could be detected. The sample $x = 0$ ($\text{SrTiO}_3\text{:N}$) shows a diffraction peaks at around 43° , which can be attributed to TiN as impurity. The same peaks were found for $x = 0.25$ and $x = 0.5$ but with by far lower intensities, indicating a much better purity of these films.

The oxynitride films have also been grown on MgO substrates to exclude uncertainties if they were really epitaxially grown on STO and not amorphous. When the PLD films were grown on MgO instead of STO, the majority of them showed the most intense diffraction peak at approximately 46.2° , which corresponds to the (200) reflection of the cubic perovskite structure (Figure 6.8 (c)). Only the sample $x = 0.5$ does not present this peak, but again shows a deviating growth direction parallel to (110) as indicated by the presence of a diffraction peak at 32.4° . For the compositions $x = 0$ and $x = 0.25$ the (110) reflection is also observed. This means that these layers are not well epitaxially grown on MgO substrate. Two small reflections peaks at 38.6° and 41° belong to the MgO substrate, as shown in Figure 6.8 (b), which depicts the diffraction patterns of the films in comparison to the pure substrate. It is noteworthy that for the films grown on MgO no TiN was observed as second phase, making this substrate favorable despite of its larger lattice mismatch in comparison to STO.

Figure 6.9 (a)-(f) shows SEM micrographs of the spin coated oxynitride films. The density increases with the La^{+3} content (x value). Films with $0 \leq x \leq 0.5$ are rather porous, and consist of a network of grains, forming an island-like structure, instead of a dense layer. Bouquet *et al* [31] have observed this kind of structure for LiNbO_3 thin films grown by a similar solution process. It was evidenced that the porosity was lower in films treated at reduced temperatures. Unfortunately, in our case it is not possible to use lower temperatures, because the formation of oxynitrides only occurs above 900°C . Curiously, the films with $x > 0.5$ show a very homogeneous structure with smooth surfaces and rather a low porosity. To investigate the film thicknesses, additional SEM cross-section micrographs were taken. As an example, Figure 6.9 (f) shows the cross-section for $x = 0.50$. As can be seen, the films have a homogeneous thickness. The layered structure of the films caused by the successive spin-coating/drying steps is evident. The layers consist of small irregular grains of about 20-40 nm. It is noteworthy that the connection between the substrate (which can be seen in the upper part of the micrograph) and the grown film is very tight. The thickness of the different films varies between 336 nm and 563 nm with an average value of approximately 440 nm. Divided by six means that each spin coating step results in ca. 75 nm.

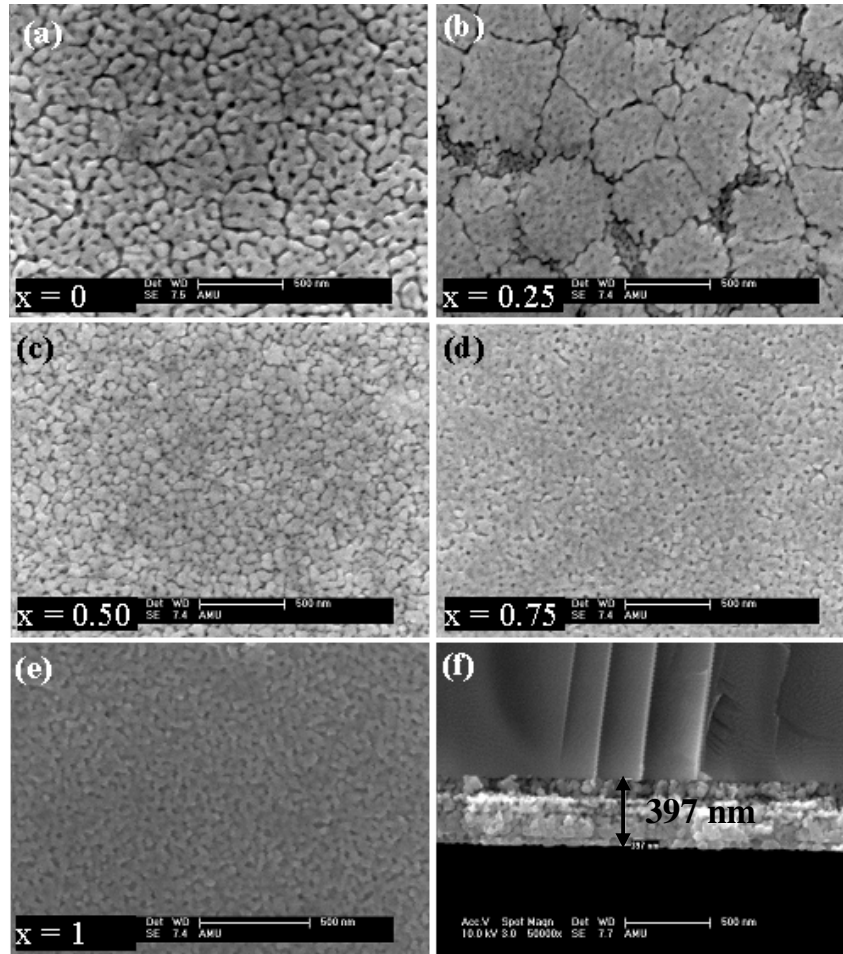


Figure 6.9: Scanning electron micrographs of the SC thin films: (a) $x = 0$, (b) $x = 0.25$, (c) $x = 0.50$, (d) $x = 0.75$, (e) $x = 1$ and (f) cross section of the sample with $x = 0.50$. All scale bars correspond to 500 nm.

The surfaces of the PLD oxynitride films and a cross section are depicted in Figure 6.10 (a)-(d). The micrographs are a bit fuzzy because of the high magnification applied (50000 and 80000). In contrast to the SC films, all the samples show a high density with only few small pores in the range of 50 nm. For the composition with $x = 0$, some larger particles are observed on the film. One possible explanation for this finding is that for this specific composition the target density was not high enough or the applied laser power was too high, extracting solid pieces from the target. Figure 6.10 (d) shows the cross section of the PLD-grown film with $x = 0.5$. The interface between the substrate (left part in the micrograph) and the film is smooth and tight. The film thickness of 450 nm is representative for all the samples. For the other compositions, the thickness values were found to vary between 270 nm and 450 nm.

The SEM image additionally reveals that the cross section of the film is highly dense and homogeneous with few tubular pores perpendicular to the surface and without distinct particles.

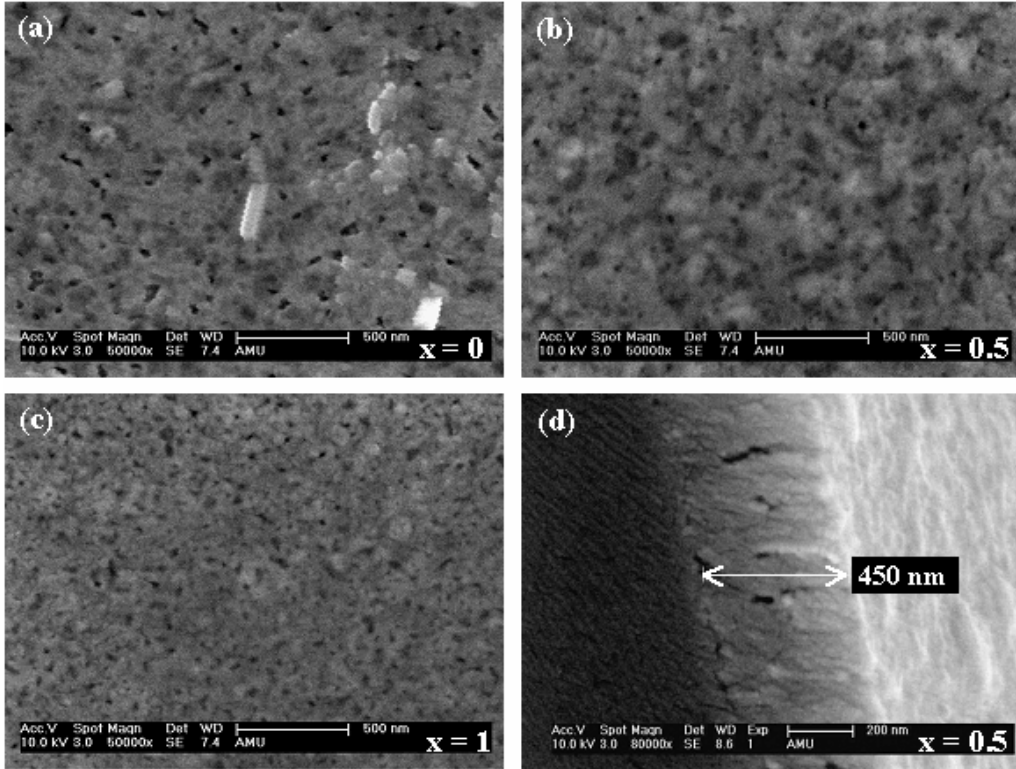


Figure 6.10: SEM of the $\text{Sr}_{(1-x)}\text{La}_x\text{Ti}(\text{O},\text{N})_3$ PLD thin films surfaces grown on STO with composition (a) $x = 0$, (b) $x = 0.5$, (c) $x = 1$ and (d) cross section of $x = 0.5$. The scale bars in (a)-(c) correspond to 500 nm while in (d) corresponds to 200nm.

For a quantitative analysis of the surface roughness, atomic force microscopy was used. The films grown by spin coating have lower roughness than the PLD ones. These measurements show that for the thin films grown by both methods there is a clear tendency for the roughness value to decrease with increasing $\text{La}^{+3}/\text{N}^{3-}$ content. The values varied between 18.5 nm and 2 nm. These numbers reveal a high homogeneity of the films, because the roughness was taken for a large scanning area of $16 \mu\text{m}^2$, as presented in figure 6.11 for the PLD thin film $x = 0.50$. The roughness of the surface is an important parameter for technical applications. For example the electrical properties of films depend not only on the microstructure but also on the interface film/electrodes, which should be smooth and possess good adhesion. On the other hand, a high porosity increases the effective surface area, which is favorable for (photo) catalytic processes.

Secondary ion mass spectrometry (SIMS) was employed to confirm the presence of nitrogen in the ammonolyzed thin films. With this technique it was possible to check for the presence of Ti, Sr, La and N in the films and in the substrate. The obtained results were very similar for all PLD and SC oxynitride film. As an example Figure 6.12 shows the results for the SC film with $x = 0.75$.

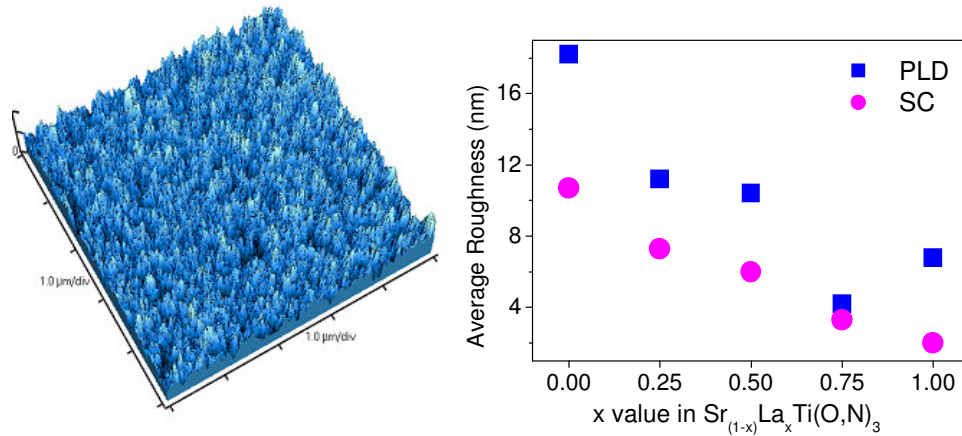


Figure 6.11: Atomic force microscopy scan of the PLD oxynitride thin film $x = 0.50$ (left) and average roughness values for the thin films $\text{Sr}_{1-x}\text{La}_x\text{Ti}(\text{O},\text{N})_3$ (right).

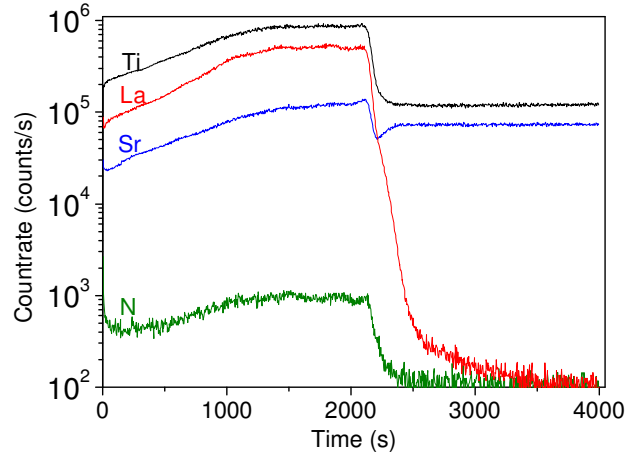


Figure 6.12: SIMS analysis results for the SC oxynitride film with $x = 0.75$.

In the diagram, the time is proportional to the depth from the surface. The higher the time the deeper is the analyzed spot. The interface between the deposited thin film and the substrate appears at around 2500 s. In the analyzed thin film the energy of the applied beam was quite high and it did not only extract ions from the superficial layer of the sample but also from the inner layers. This phenomenon smears out the results giving gradual intensity changes instead of sharp steps at the

interface as film/substrate. Looking at Figure 6.12, it is apparent that lanthanum and nitrogen are only present in the film, because after 2500 s the intensities of the corresponding ions go down to almost zero. On the other hand, titanium and strontium show only a small intensity change at the interface and their intensities remain high in the substrate region, as it is expected for the SrTiO₃ substrate. These results prove that nitrogen is exclusively incorporated in the oxynitride films and does not react with the substrate.

Optical properties were characterized by UV-vis spectroscopy in transmission mode for the spin coated films. Band gap values were calculated assuming a direct band gap. All purely oxide films, which were prepared for comparison with their corresponding oxynitrides, showed band gap values around 3.1 eV. This number is higher than the visible light energy, which explains their transparency. Figure 6.13 shows the results for the SC oxynitride films. Their optical band gap varied between 2.3 eV (LaTiO₂N) and 3.1 eV (SrTiO₃:N). These values agree quite well with the calculated band gaps of the polycrystalline samples (chapter 6.1) with deviations around 0.2 eV.

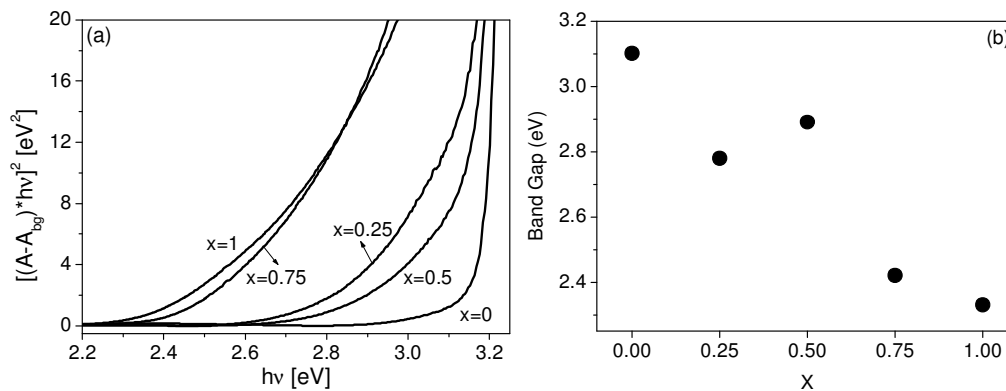


Figure 6.13: (a) UV-visible transmission measurement of the SC oxynitride thin films and (b) corresponding band gap values.

The UV-vis measurements show that the optical band gaps can be modified in a remarkable range by co-substitution of the A-type cation and anion, respectively. Unfortunately it was not possible to measure the optical properties of the PLD films in transmission mode because they were glued on the heater using silver paint during the ablation. The calcinated silver paint blocked the light transmission through the films and the UV-vis equipment in reflectance modus was not accessible by the time that the measurements were carried out.

To investigate the electrical properties of the films, 2-point resistivity measurements were performed in the temperature range 4.2 - 300 K. For the different SC compositions a strong change in the electrical behavior was found. All the oxide films and the oxynitrides with $x = 1$ and $x = 0.75$ turned out to be insulators, i.e. the resistance was above $20 \text{ M}\Omega\cdot\text{cm}$. For $x = 0$ and 0.5 the films show semiconducting behavior, i.e. the resistances decrease with increasing temperature, as shown in Figure 6.14. For $x = 0.25$ an interesting semiconductor/metal transition was observed. The resistivity decreases to a minimum of $0.02 \text{ }\Omega\cdot\text{cm}$ at 120 K. At higher temperatures the resistance increases and the film behaves like a metal. The resistivity values of the SC oxynitride films at room temperature were 0.36 , 0.028 and $1.3 \text{ }\Omega\cdot\text{cm}$ for $x = 0$, 0.25 and 0.5 , respectively.

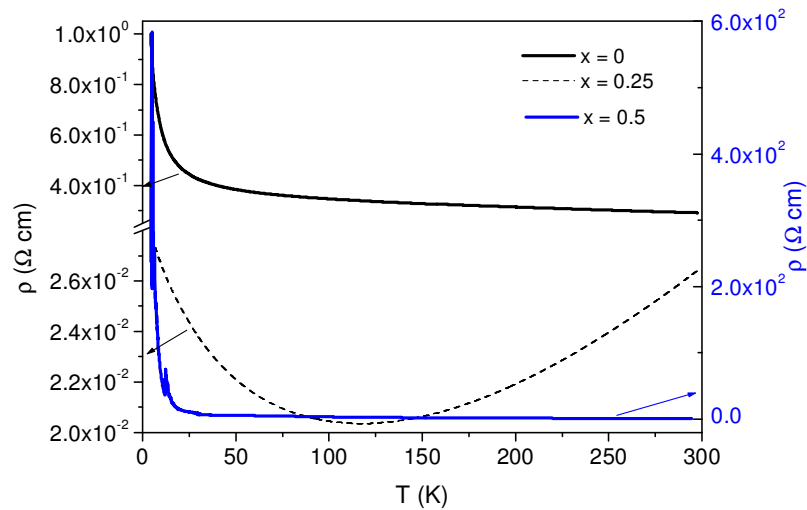


Figure 6.14: Resistivity *versus* temperature for the SC thin films $\text{La}_x\text{Sr}_{(1-x)}\text{Ti}(\text{O},\text{N})_3$ with $x = 0$, $x = 0.25$ and $x = 0.50$.

For the PLD films, all the oxides and the oxynitride with $x = 1$ (LaTiO_2N) grown on STO were insulating. The simultaneous substitution of $\text{Sr}^{2+}/\text{O}^{2-}$ by $\text{La}^{3+}/\text{N}^{3-}$ has a strong influence in the resistivity of the films (Figure 6.15). For example, at room temperature the resistivity values for $x = 0.75$, 0.50 , 0.25 and 0 are $2.2\cdot 10^{-2}$, $1.1\cdot 10^{-3}$, $3.7\cdot 10^{-4}$ and $4.7\cdot 10^{-3} \text{ }\Omega\cdot\text{cm}$, respectively. All oxynitride films have a metallic behavior above 33 K as shown in Figure 6.15 (b). For $x = 0.75$, 0.5 and 0 a semiconducting behavior was observed below 30 K, as can be better visualized in Figure 6.15 (a).

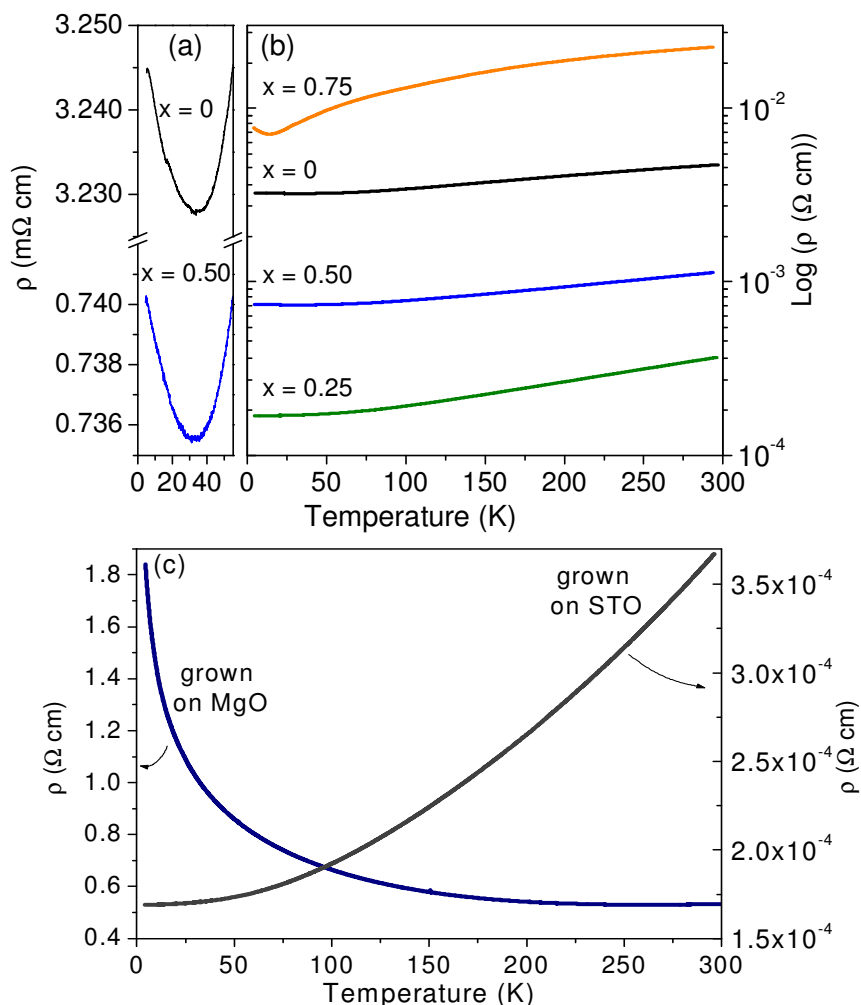


Figure 6.15: Resistivity *versus* temperature for the PLD oxynitride films $\text{Sr}_{(1-x)}\text{La}_x\text{Ti}(\text{O},\text{N})_3$: (a) $x = 0.5$ and $x = 1$, (b) $x = 0, 0.25, 0.5$ and 0.75 grown on STO and (c) comparison of the composition $x = 0.25$ grown on MgO and STO.

This finding is an indication for a semiconductor/metal transition in the oxynitride films grown by PLD. It is furthermore noteworthy that the resistivities do not monotonically increase with x . The composition with $x = 0.25$ shows the lowest resistivity values for both SC and PLD films, while both higher and lower $\text{La}^{3+}/\text{N}^{3-}$ contents result in larger values. The observed resistivities of the PLD films are much lower than the ones of the spin-coated films. This finding can be explained by the denser structure of the films grown by the PLD technique.

A completely different electrical behavior was observed for the oxynitride films ablated on MgO substrates. All the films were insulators, except for $x = 0.25$. This sample presented a semiconductor behavior as plotted in Figure 6.15 (c). Several

factors may explain the discrepancies between the electrical measurements for the PLD samples deposited on STO and MgO substrates. First, studies on Sr-doped LaTiO₃ showed that the resistivity decreases when these compounds are put under pressure [27, 32]. Since STO ($a = 3.90 \text{ \AA}$) has a smaller unit cell than MgO ($a = 4.21 \text{ \AA}$), we can assume that the films are under pressure when grown on STO and they are supposed to show lower resistivity than the ones grown on MgO that are under traction. Second, the possible influence of the TiN impurity in the films needs to be taken into account, especially since TiN also shows a metallic behavior [33]. Nevertheless, the TiN contribution to the electrical conductivity is of minor importance. Assuming a strong influence of TiN on the electrical properties, the film with the highest TiN impurity concentration ($x = 0$) should show the lowest resistivity values. On the contrary, the composition for which almost no TiN was found in its XRD pattern ($x = 0.25$) yielded the lowest resistance values, indicating that the effect of TiN impurities can well be neglected.

Another possible explanation that comes to mind is a variation in the oxygen vacancy concentration among the films. It is known that variation in oxygen concentration can change the electrical behavior of LaTiO_{3+x} from insulator to semiconductor to metallic [34]. In this case Ti⁴⁺ is reduced to Ti³⁺, as given by the equation:



This phenomenon is accompanied by a phase transition, from a layered ($n = 4$) perovskite-related LaTiO_{3.5} to a three dimensional ($n = \infty$) orthorhombically distorted perovskite LaTiO₃ [35].

In the studied oxynitride films, in which titanium remains in the oxidation state +4, formation of oxygen vacancies is required to account for the charge neutrality. For the oxynitride formation, the compound structure is also changed from the $n = 4$ layered perovskite-related LaTiO_{3.5} to distorted three-dimensional structure LaTiO₂N.

It is likely that small variations during the ammonolysis reaction lead to samples with identical cationic composition but with slightly different O/N ratios, resulting in deviating vacancy concentrations and/or slight differences in the crystallographic structure. These deviations may in turn lead to very different

electrical properties. An evidence for the O/N variation is the color difference among the films that show a quite diversity of green patterns.

In conclusion it can be said that thin films of the oxynitride perovskite system $\text{Sr}_{(1-x)}\text{La}_x \text{Ti}(\text{O},\text{N})_3$ have been successfully grown by spin coating and pulsed laser deposition and subsequent ammonolysis. The PLD films showed higher electrical conductivities than the SC films. One advantage of the PLD method is that the films are dense and usually grow epitaxially on single crystalline substrates of suitable lattice parameters. The big disadvantages of PLD are that an expensive set-up is required, the obtained films are rather thin and appropriate (commercial) substrates are often not available or very costly. On the other hand, the spin-coated films can be cheaply prepared from water solutions and be employed to cover larger areas. Because of the films porous surface (high concentration of reaction sites) they could also be employed for (photo) catalysis. The disadvantages of films prepared by SC are non-epitaxially structures and a grainy structure causing poor electrical conductivity due to the grain boundary effects.

References

- [1] J. Wang, S. Yin, M. Komatsu, T. Sato, *J. Eur. Cer. Soc.* 25 (2005) 3207.
- [2] F. Cheviré, F. Tessier, R. Marchand, *Eur. J. Inorg. Chem.* 2006 (2006) 1223.
- [3] R. Marchand, F. Pors, Y. Laurent, *Ann. Chim. Fr.* 16 (1991) 553.
- [4] S. J. Clarke, B. P. Guinot, C. W. Michie, M. J. C. Calmont, M. J. Rosseinsky, *Chem. Mater.* 14 (2002) 288.
- [5] J. Hutton, R. J. Nelmes, *J. Phys. C: Solid State Phys.* 14 (1981) 1713.
- [6] R. D. Shannon, C. T. Prewitt, *Acta Crystallogr. B* 25 (1969) 925.
- [7] D. Logvinovich, L. Bocher, D. Sheptyakov, R. Figi, S. G. Ebbinghaus, R. Aguiar, A. Reller, A. Weidenkaff, in preparation.
- [8] S. Venkataraj, D. Severin, S. H. Mohamed, J. Ngaruiya, O. Kappertz, M. Wuttig, *Thin Solid Films* 502 (2006) 228.
- [9] F. Vaz, P. Carvalho, L. Cunha, L. Rebouta, C. Moura, E. Alves, A. R. Ramos, A. Cavaleiro, P. Goudeau, J. P. Riviere, *Thin Solid Films* 469 (2004) 11.
- [10] F. Vaz, P. Cerqueira, L. Rebouta, S. M. C. Nascimento, E. Alves, P. Goudeau, J. P. Rivière, K. Pischow, J. Rijk, *Thin Solid Films* 447 (2004) 449.
- [11] M. S. Wong, H. P. Chou, T. S. Yang, *Thin Solid Films* 494 (2006) 244.
- [12] F. Fabreguette, L. Imhoff, M. Maglione, B. Domenichini, M. C. M. Lucas, P. Sibillot, S. Bourgois, M. Sacilotti, *Chem. Vap. Deposition* 6 (2000) 109.
- [13] J. M. Chappe, N. Martin, G. Terwagne, J. Lintymer, J. Gavaille, J. Takadoum, *Thin Solid Films* 440 (2003) 66.
- [14] F. Grasset, L. Spanhel, S. Ababou-Girard, *Superlattices Microstruct.* 38 (2005) 300.
- [15] X. B. Lu, Z. G. Liu, *J. Electronic Mat.* 30 (2001) 554.
- [16] Y. C. Ee, Z. Chen, S. B. Law, S. Xu, *Thin Solid Films* 504 (2006) 218.
- [17] J. Cabana, C. Mercier, D. Gautier, M. R. Palacin, *Z. Anorg. Allg. Chem.* 631 (2005) 2136.

- [18] M. Koike, T. Ino, Y. Kamimuta, M. Koyama, Y. Kamata, M. Suzuki, Y. Mitani, A. Mishiyama, *Phy. Rev. B* 76 (2006) 125123.
- [19] V. Rigato, A. Patelli, G. Maggioni, S. Restello, S. Vezzu, D. G. Teer, D. Boscarino, A. Figeras, L. E. Depera, E. Bomtempi, *Surf. Coat. Technol.* 174 (2003) 266.
- [20] G. Pant, A. Gnade, M. J. Kim, R. M. Wallace, B. E. Gnade, M. A. Quevedo-Lopez, P. D. Kirsch, *Appl. Phys. Lett.* 88 (2006) 032901.
- [21] C. H. Lai, B. C. Lin, K. M. Chang, K. Y. Hsieh, Y. L. Lai, *Jpn. J. Appl. Phys.* 45 (2006) 4898.
- [22] M. Hirai, T. Suzuki, J. W. H. Suematsu, K. Yatsui, *J. Vac. Sci. Technol. A* 21 (2003) 947.
- [23] S. Zhao, Z. Fu, Q. Qin, *Thin Solid Films* 415 (2002) 108.
- [24] S. L. Zhao, Q. Z. Qin, *J. Power Sources* 122 (2003) 174.
- [25] Y. Tokura, Y. Taguchi, Y. Okada, Y. Fujishima, T. Arima, *Phys. Rev. Lett.* 70 (1993) 2126.
- [26] K. Shibuya, T. Ohnishi, M. Kawasaki, H. Koinuma, M. Lippmaa, *Jpn. J. Appl. Phys.* 43 (2004) L1178-L1180.
- [27] B. Vilquin, T. Kanki, T. Yanagida, H. Tanaka, T. Kawai, *Solid State Com.* 136 (2005) 328.
- [28] K. Kim, Y. W. Kwon, D. P. Norton, D. K. Christen, J. D. Budai, B. C. Sales, M. F. Chisholm, C. Cantoni, K. Marken, *Solid State Electron.* 47 (2003) 2177.
- [29] L. Le Gendre, C. Le Paven, J. Pinel, D. Fasquelle, J. C. Carru, *Sil. Ind. Special Issue* 69 (2004) 165.
- [30] I. Marozau, M. Döbeli, T. Lippert, D. Logvinovich, M. Mallepell, A. Shkabo, A. Weidenkaff, A. Wokaun, *Appl. Phys. A* 89 (2007) 933.
- [31] V. Bouquet, E. Longo, E. Leite, J. A. Varela, *J. Mater. Res.* 14 (1999) 3115.
- [32] Y. Okada, T. Arima, Y. Tokura, *Phys. Rev. B* 48 (1993) 9677.
- [33] K. Lal, A. K. Meikap, S. K. Chattopadhyay, S. K. Chatterjee, M. Ghosh, K. Baba, R. Hatada, *Physica B* 307 (2001) 150.
- [34] F. Lichtenberg, A. Herrnberger, K. Wiedenmann, J. Mannhart, *Prog. Solid State Chem.* 29 (2001) 1.
- [35] F. Lichtenberg, T. Williams, A. Reller, D. Widmer, J. G. Bednorz, *Z. Phys. B: Condens. Matter* 84 (1991) 369.

7. Oxynitride Perovskites as Photocatalysts

A photocatalyst is a substance that shows catalytic properties under irradiation. The photocatalyst absorbs light by electronic excitations and starts a chemical reaction, based on reduction/oxidation (redox) phenomena without being decomposed itself. Photosynthesis in plants is a well-known example of such a photocatalytic reaction, in which chlorophyll acts as the photocatalyst transforming water and carbon dioxide into glucose in the presence of sunlight [1]. Photocatalysts can be extensively used in water and air purification as well as in hydrogen and oxygen production from water splitting.

In water decontamination photocatalysis can be applied to clean the wastewater contaminated with biological mater and hazardous metals deriving from industrials discharge, excess use of pesticides/fertilizers and domestic waste. The photocatalysts are able to destroy organic contaminants as microorganisms (bacteria, germs, viruses and fungi) and solvents (aldehydes, alcohols, phenols, chlorides, etc), as well as to reduce heavy metals to their nontoxic form, such as Cr(VI) to Cr(III) [2, 3].

In air purification photocatalysts can be used for sterilization and deodorization in hospitals, hotels and houses, destroying microorganisms and/or oxidizing unpleasant odor-causing organic molecules (as cigarette smoke, mould, domestic smells and pets-odor). Photocatalysts can also be applied to purify the air in big cities, eliminating toxic gases and/or contaminant molecules (as volatile organic compounds, NO_x, SO_x) that are expelled from vehicles exhaust gas [4, 5].

Considering water splitting, the evolution of H₂ and O₂ from water using sunlight would be the cheapest and most convenient way to solve energy problems [6, 7]. Hydrogen is of great interest for new clean energy technologies. H₂ is used as fuel, as example in NASA's space shuttles fuel cells, to operate electrical systems. The emitted gas is water, which can even be consumed by the crew in space. Nowadays, almost all the used hydrogen (ca. 40 million tons) is produced by reforming of natural gases [8]. In this process the co-product is CO₂, one of the main responsible for greenhouse effect on the earth surface. Many research groups in the whole word are trying to develop better ways to produce hydrogen. On the other hand, oxygen is also a widely used gas. Some examples of its applications are in hospitals

for patients who have difficulty in breathing or having operations. Airplanes, which fly at high altitude, must carry oxygen. The steel industry uses oxygen to burn off impurities, such as carbon, sulphur and phosphorus from molten iron.

A photocatalyst has to be a semiconductor material with a band-gap energy varying from ca. 1.1 to 3.7 eV (e.g. TiO_2 , Si, ZnO, Fe_2O_3 , SiC, CdS, WO_3 , ZnS). A filled valence band and an empty conduction band characterize their electronic structure. Figure 7.1 represents a photocatalytic reaction. When a photocatalyst is illuminated by highly energetic light (photons with energy $h\nu >$ band gap) an electron is transferred from the valence band (VB) to the conductor band (CB). With this phenomenon an electron-hole pair is formed [3]. The electrons and holes can move in the respective bands but most of them simply recombine producing thermal energy. The lifetime of an e^-h^+ pair is only a few nanoseconds, but this may be enough to promote redox reactions. The electron-hole pairs near the surface can be involved in reactions. The generated holes have strong oxidative character and produce hydroxyl radicals by reacting with water at the surface, and the generated hydroxyl radicals can cause oxidative reactions in organic compounds. On the other hand, the generated electrons can reduce oxygen molecules producing superoxide free radicals.

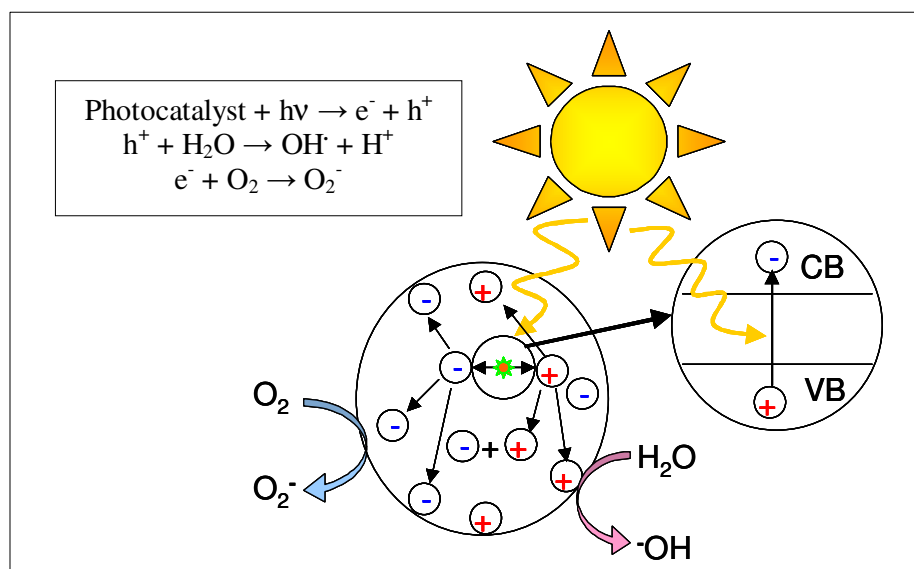


Figure 7.1: Schematic representation of a semi-conductor photocatalyzed reaction.

Because organic matter (bacteria, viruses, germs, and odor molecules) is usually more oxidative than water, holes are more likely to cause oxidation of organic compounds present in the aqueous solutions. Additionally, the recombination rate of

carriers (holes and electrons) decreases when the concentration of organic matter is higher. Organic compounds are thus decomposed and eventually turn into carbon dioxide and water.

TiO₂ is the most popular photocatalyst employed. The possibility of photoelectrolysis was demonstrated for the first time in 1969, when Fujishima [9] obtained a single crystal of titanium oxide and used it as an electrode. A closed circuit using titanium oxide and platinum black as counter electrode was exposed to the light of a xenon lamp. When the surface of the TiO₂ electrodes was irradiated with light consisting of wavelengths smaller than its band gap (415 nm = 3.0 eV), gas bubbles evolved from both electrodes. These gases were found to be oxygen evolving from the TiO₂ electrode and hydrogen from the Pt side. Thus it was proven that water could be decomposed into oxygen and hydrogen under UV light irradiation without application of an external voltage. Moreover, the titanium oxide had not been consumed in the reaction even after several days of continuous photo irradiation.

Generally speaking, a photocatalyst should possess the following characteristics:

- Semiconducting
- Chemically and biologically inert
- Photocatalytically stable
- Efficiently catalyzes reactions
- Activated by sunlight
- Preferable it should be non-toxic, easy to produce and cheap

TiO₂ fulfills almost all of these requisites but it is only activated by a small part of the sunlight, namely the ultra violet part (UV < 400 nm). Looking at the sunlight spectrum depicted in Fig. 7.2, one can visualize how little of the total sunlight radiation that reaches the earth's surface can actually be used by TiO₂ in its photocatalytic reactions. Only about 3-5% of the total sunlight may photoactivate TiO₂ to generate charge carriers. It would of course be much more efficient to use more of the light that we get for free. In the last years, studies on the possibility to apply perovskite-type oxides as photocatalyst have increased. For example, Kato and Kudo [10,11] studied water splitting into H₂ and O₂ for various tantalates and niobates, such as LiTaO₃, NaTaO₃, SrNbO_{3.5}, KTaO₃, SrTaO_{3.5}, CaTa₂O₆, etc. Uno *et al* [12] investigated the titanate series, as LaTiO_{3.5}, SmTiO_{3.5}, GdTiO_{3.5}, YbTiO_{3.5} and

others. Ikeda *et al* examined $K_4Nb_6O_{17}$ [13] and Domen *et al* analyzed $SrTiO_3$ [14]. The problem of these kinds of materials is the same as for TiO_2 , as they have high band gap energies and only absorb in the ultra violet range.

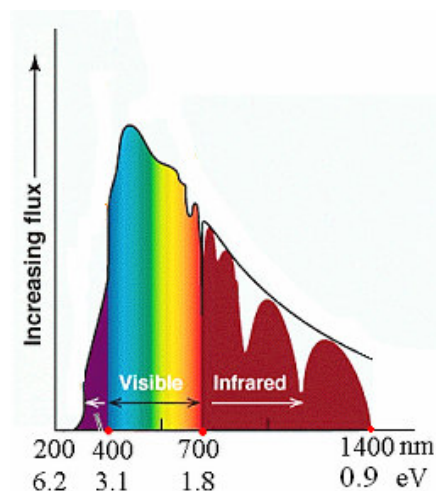


Figure 7.2: Solar spectrum at sea level. Only the ultra violet part ($\lambda < 400$ nm) is accessible for TiO_2 in its photocatalysis reactions [15].

Oxynitride perovskites, on the other hand, absorb a much broader part of the sunlight as they are in most cases colored. They are therefore promising candidates to be used as photocatalysts under visible light, e.g. sunlight. It was reported that $LaTiO_2N$ and $SrNbO_2N$ are able to produce hydrogen and oxygen from water-methanol mixtures under visible light irradiation [16-18]. On the other hand $ATaO_2N$ ($A = Ca, Sr$ and Ba) oxynitrides formed H_2 using the same solution but were not able to oxidize water in O_2 [19]. $LaTaON_2$ and $Y_2Ta_2O_5N_2$ have led to a considerable hydrogen evolution when Pt/Ru were used as co-catalysts [20, 21]. $Rb(Ca,La)NbO:N$ compounds were also investigated, but because they are unstable in water, their photocatalytic activity was quite poor [22]. $Zn_xTiO_yN_z$ decomposed methylene blue and formed hydrogen and oxygen from water solutions [23, 24]. $M_xZnO_yN_z$ ($M = Ga$ and Ge) have also demonstrated H_2 and O_2 evolution from water solution containing co-catalysts [25, 26].

The measurement of the photocatalytic activity of some selected oxynitride perovskites are reported in this chapter. A comparison among their activities is presented to get the first impression of how good they could be as photocatalysts. Three different set-ups have been employed with this intention. First, the

decomposition of methylene blue in aqueous solutions was investigated. As second reaction, the water splitting itself was examined and finally the gas phase decomposition of acetone was studied.

The employed synthesis methods for the applied oxynitrides samples, their colors, BET surface areas and band gaps are given in Table 7.1. The obtained result for the UV-vis analysis in reflectance mode is shown in Figure 7.3. As discussed in Chapter 4 the color of the oxynitrides (band gap and consequently the absorption edge) can be shifted with cationic and/or anionic substitutions.

Table 7.1: Oxynitride samples used in the photocatalysis experiments and their respective synthesis method, ammonolysis time and temperature, band gap and BET surface area.

Sample	Synthesis Method ⁺	Ammonolysis T (°C)	Ammonolysis Time (h)	Color	Band Gap [§] (eV)	Surface Area (m ² /g)
CaNbO ₂ N ^{*°}	Pechini	950	60	Black	2.10	9.9
SrNbO ₂ N [*]	Solid state	950	54	Brown	1.94	3.4
SrNbO ₂ N [°]	Pechini	950	36	Brown	1.94	9.1
BaNbO ₂ N [*]	Solid state	950	72	Black	1.80	1.0
SrTaO ₂ N ^{*°#}	Pechini	950	18	Orange	2.14	5.8
BaTaO ₂ N [*]	Solid state	1000	54	Red	1.91	2.6
NdTaO ₂ N ^{*°}	Pechini	1000	54	Red	2.10	6.4
LaTiO ₂ N [°]	Solid state	950	126	Brown	2.19	3.6
LaTiO ₂ N ^{*°}	Pechini	950	24	Brown	2.19	13.7
LaTiO ₂ N [°]	Spray pyrolysis	950	24	Brown	2.19	10.0
P25 ^{▪°#}	-	-	-	White	3.24	50

+ Synthesis method employed to prepare the respective oxide precursor (chapter 3.2).

§ Calculated considering direct allowed band gap as described in chapter 2.4

Used for decomposition of methylene blue in aqueous solution (see Section 7.1)

* Used in water splitting (see Section 7.2)

° Used for gas phase acetone decomposition (see Section 7.3)

▪ P25 is the commercial trademark from Degussa for nanoparticles of TiO₂ composed of ca. 30 wt% rutile and 70 wt% anatase.

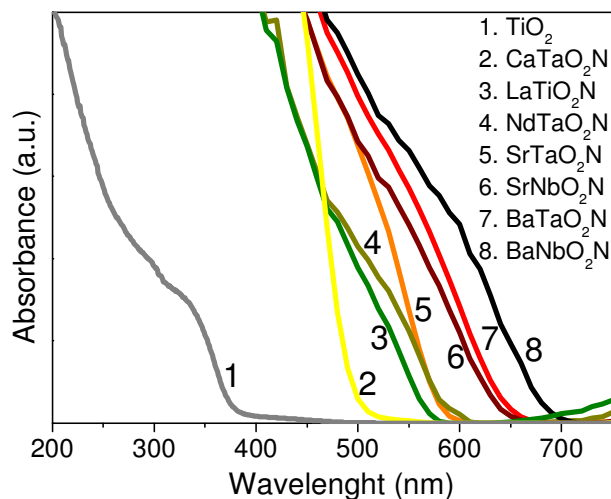


Figure 7.3: Absorbance spectra for selected oxynitrides in comparison with TiO_2 .

7.1. Decomposition of Methylene Blue in Aqueous Solution

As mentioned in chapter 7, one of the possible applications for photocatalysts is the decomposition of organic material for the detoxification of wastewater. The investigated organic dye was methylene blue (MB). It is easy to detect the MB in water solutions because of its characteristic blue color [27, 28]. There are a number of intermediate organic molecules formed during the redox reactions of MB on the photocatalyst surface. The MB photodecomposition reactions proposed by Houas *et al* [29] are shown in Figure 7.4. Other studies have detected different intermediate compounds as leucomethylene blue, leucomethylene blue sulfoxide, leucomethylene blue sulfone, benzenesulfinic acid, benzenesulfinic acid with hydroxyl radical and benzenesulfinic acid with NH_2 radical [30] or azure A, azure B, azure C, thionine and phenothiazine [31]. The decomposition of methylene blues is composed of complicated intermediate reactions but the obtained final products were always the same for the different publications: CO_2 , H_2O , HNO_3 and H_2SO_4 [29-32].

To test the catalytic potential of the oxynitride samples, a simple setup consisting of a suspension of the oxynitrides with MB aqueous solution was used. This mixture was stirred and illuminated for several hours. A halogen lamp (Osram 15 V, 150 W) was used to irradiate a quartz reactor vessel containing the organic aqueous solution [33]. As the halogen lamp heats up during the experiment, a water-cooling device was placed between the reaction vessel and the lamp. The water absorbs the IR light emitted by the halogen lamp. Running water from a cryostat

through the IR filter kept the reaction vessel at constant temperature. Fig. 6.5 shows a photograph of the used set-up.

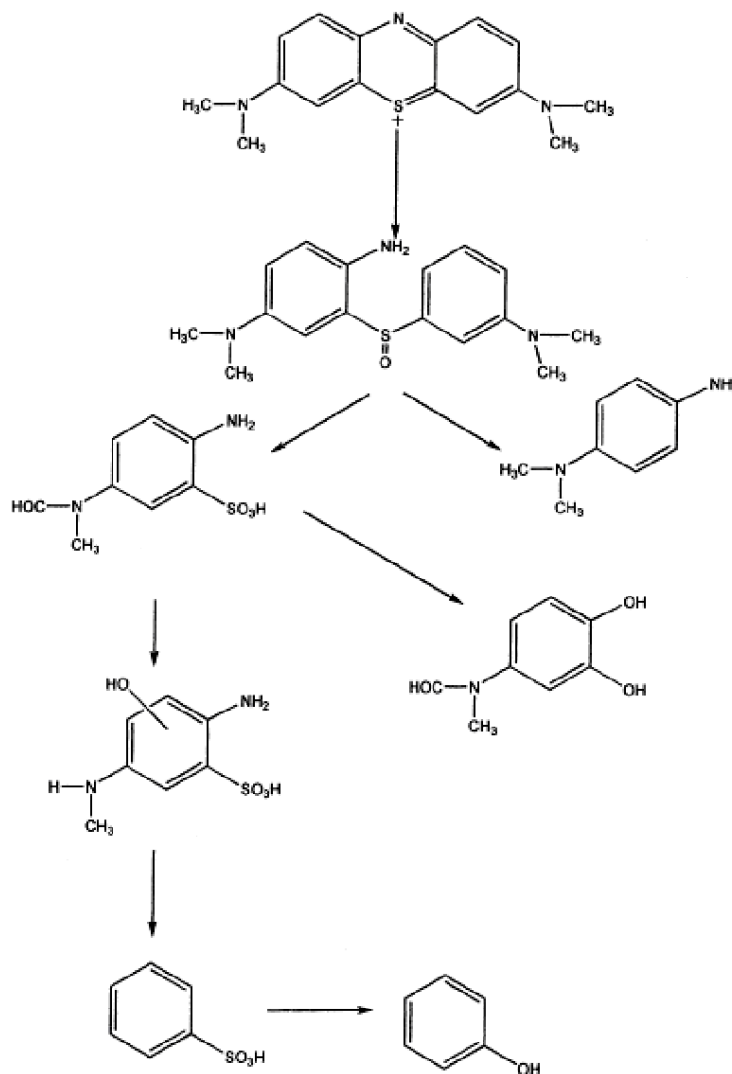


Figure 7.4: Proposed reaction mechanism for methylene blue decomposition [29].

The initial concentration of methylene blue in water was arbitrarily chosen as 18 mg/L. The amount of tested photocatalyst was 0.5 g/L. The basic idea of the experiments is to follow the degradation (decolorization) of MB. After switching on the lamp, aliquots were taken at fixed time intervals and the MB concentration was measured by UV-vis spectroscopy. The catalyst was separated from the dye solution by centrifugation. This separation step is needed because if particles remained dispersed, the light would be absorbed and/or scattered, impeding the UV-Vis

measurements. Methylene blue has its maximum light absorption at a wavelength of 600 nm therefore this wavelength was used to determine the dye concentration.

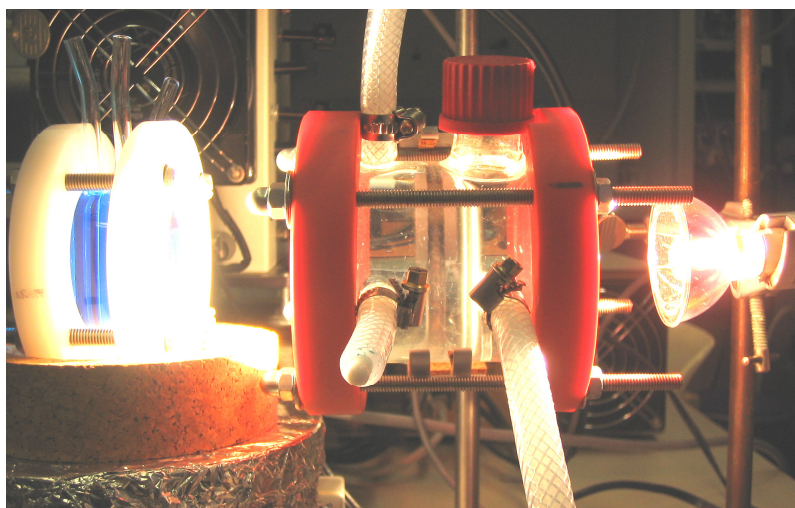


Figure 7.5: Set-up for methylene blue photodecomposition showing from left to right the reaction vessel, the cooling device (IR filter) and the halogen lamp.

Figure 7.6 depicts a plot using P25 (TiO_2 – Degussa) and SrTaO_2N as photocatalytic materials. For comparison, a pure methylene blue solution without any photocatalyst was also exposed to irradiation (blank measurement). Open symbols in the graphic are measurements performed without UV filter while the closed symbols correspond to runs with an additional UV filter (that lets light of $\lambda > 380$ nm pass through) attached in front of the reaction vessel. P25 showed a better degradation rate than SrTaO_2N when the measurements were done without UV filter. The decomposition rate for all experiments decreased when the UV filter was used. This finding was already expected since the most energetic part of the light was cut off. P25 and SrTaO_2N showed almost the same decomposition rate as the blank run when the UV radiation was blocked, indicating their poor catalytic efficiency when activated by the visible part of the spectrum. SrTaO_2N has a surface area more than eight times smaller than TiO_2 . This parameter should be considered since a higher surface area means more active sites for the catalytic reaction. A more detailed discussion about the influence of the surface in the photocatalytic activity of the sample is given for LaTiO_2N in the next chapter (7.3).

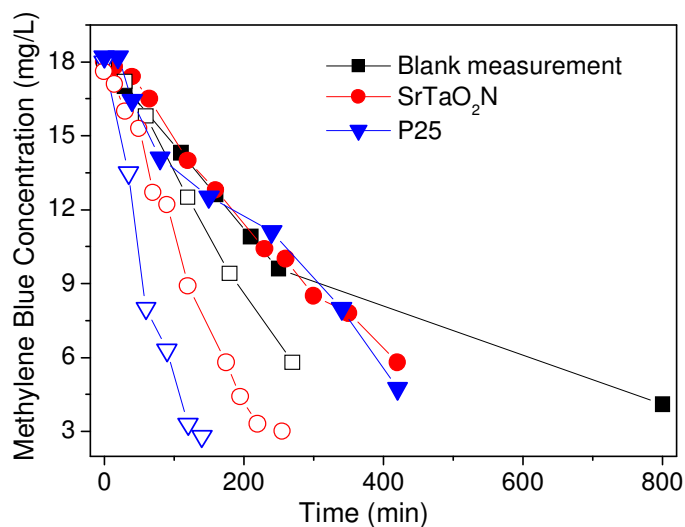


Figure 7.6: Methylene blue concentration *versus* time. The used photocatalytic concentration was 0.5 g/L in water solution. Open symbols correspond to reactions without UV-filter, closed symbols to reactions using UV-filter ($\lambda > 380\text{nm}$).

Two problems appeared during the experiments. First it was striking that the methylene blue already decomposed under light without any photocatalytic material present. The decomposition was slower than in the presence of a photocatalyst, but it was quite high for reliable results. The second problem was that the tested photocatalytic compounds adsorbed the organic dye on their surfaces. After some hours of reaction, P25 was found to turn blue and SrTaO₂N, which is originally orange, had changed to a green color. Because of these reasons, MB is not a good organic molecule to be used in this kind of analysis. Some experiments using methylene orange (MO) as organic material were also tried out. The MO was quite stable, not showing decomposition under irradiation and it was also adsorbed on the photocatalysts surfaces. The photocatalytic power of the oxynitride samples was therefore tested using other two different set-ups, which are described in the next sections (7.2 and 7.3).

7.2. H₂ and O₂ Evolution from Aqueous Solutions

For water splitting under visible light not only a band gap energy smaller than 3 eV is required but also the band gap edge potentials have to be suitable. As shown in Figure 7.7 the bottom of the conduction band should be located at a more negative potential than the reduction potential of H⁺ to H₂ and the top of the valence band should be situated more positive than the oxidation potential of H₂O to O₂ [34].

Normally for water reduction (i.e. hydrogen evolution), co-catalysts are used. Co-catalysts are often nanoparticles of noble metals or metal oxides (e.g. Pt, Rh, Pd or NiO_x, RuO₂, Cr₂O₃), they are loaded on the surface of the photocatalyst to form active sites and reduce the activation energy for gas evolution. The choice of the co-catalyst is very important, as example for Y₂Ta₂O₅N₂ the use of 0.25 wt % of Ru together with 0.15 wt% of Pt increased the quantity of hydrogen evolution 22 times compared with the sample 0.15 wt% Pt/Y₂Ta₂O₅N₂ [21].

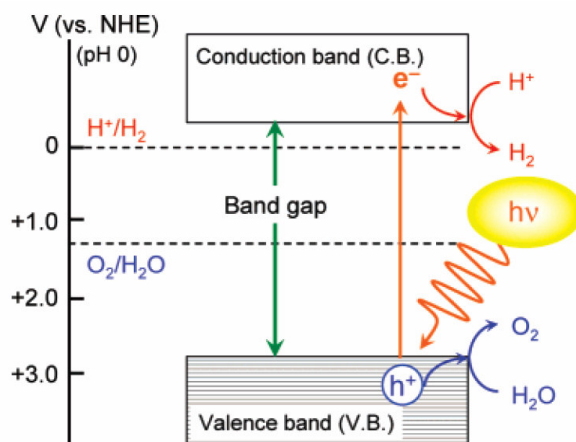


Figure 7.7: Basic principle of overall water splitting [34].

The photocatalytic power of selected oxynitride perovskites to form H₂ and O₂ from aqueous solutions was measured by Prof. Kazunari Domen, University of Tokyo – Japan. The used reactor is schematized in Figure 7.8. It consists of a Pyrex reactor vessel connected to a closed gas circulation and evacuation system. The reaction vessel is illuminated by a 300 W Xe lamp equipped with UV cut-off filter ($\lambda > 420$ nm) and a water-cooling system. The used solution volume was 200 ml with 0.2 g of oxynitride for both experiments. The reaction solution was evacuated several times to remove air before the lamp was switched on. The reaction time was 5 hours. During this period the evolved gas was analyzed by gas chromatography. In this set-up, the two part reactions (formation of hydrogen and oxygen) are studied applying slightly different reaction conditions. Reduction of H⁺ to H₂ was examined using 0.5 wt% Pt as co-catalyst in an aqueous solution containing 10 % volume of methanol. The alcohol serves as sacrificial electron donor. Oxidation of H₂O to O₂ in the presence of Ag⁺ (as electrical receptor) was measured in a separate reaction. The photocatalytic activities of the samples are shown in Figures 7.9 and 7.10. A significant hydrogen

evolution from water-methanol solutions was observed for NdTaON_2 , BaTaO_2N and LaTiO_2N with total H_2 productions of 1, 4 and 9 μmol , respectively, during 5h of reaction. Additionally, oxygen evolution was investigated using Ag^+ aqueous solution with La_2O_3 . The latter oxide was added to keep the pH ~ 8 . For this reaction the compounds SrTaO_2N , BaTaO_2N , LaTiO_2N and CaNbO_2N were found to show a considerable activity in O_2 production of 4, 6, 22 and 37 μmol , respectively. CaNbO_2N showed a surprisingly good oxygen evolution of almost two times higher than LaTiO_2N in the same reaction time.

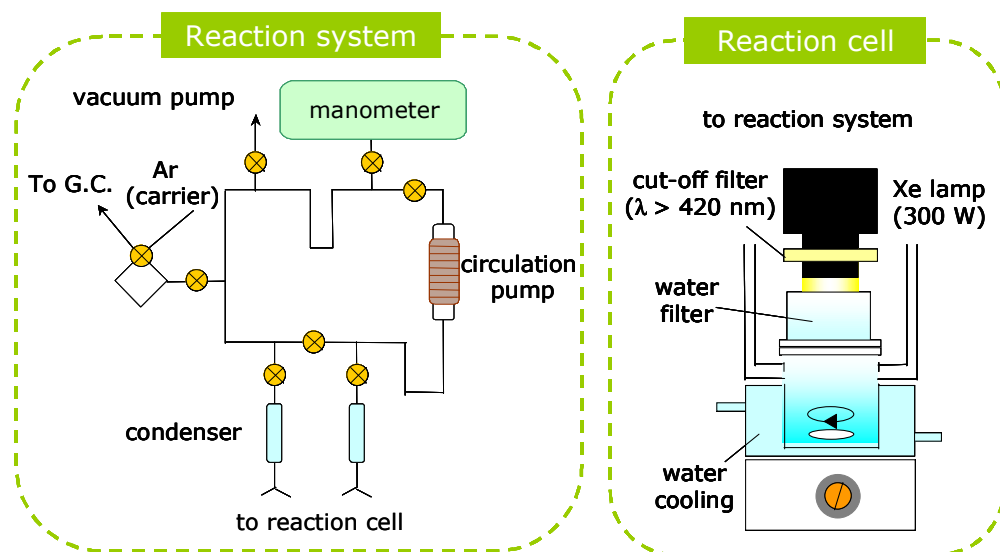


Figure 7.8: Scheme of the used set-up for water splitting by photocatalysis [18].

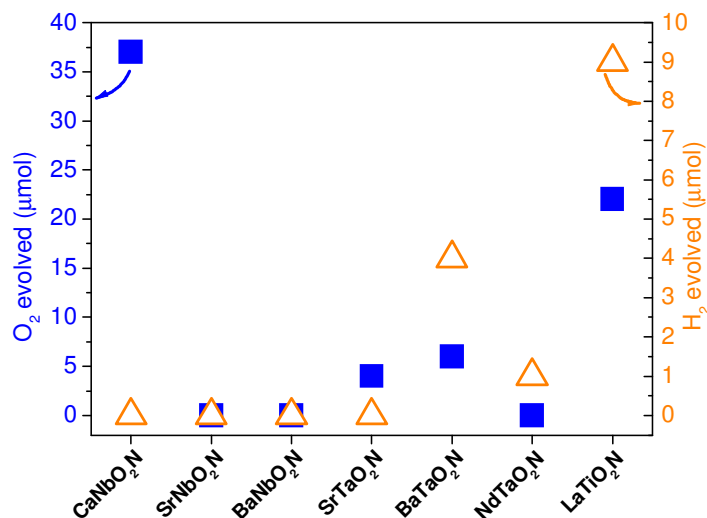


Figure 7.9: O_2 and H_2 evolution for selected oxynitride perovskites resulting from 5 hours of reaction. Open symbols correspond to hydrogen evolution and the closed ones to oxygen.

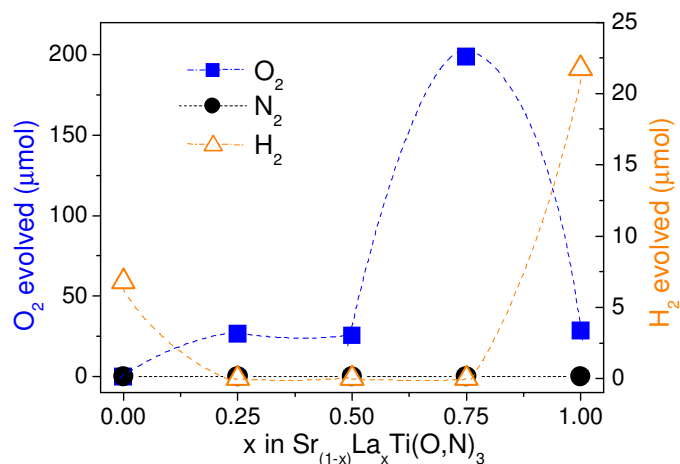


Figure 7.10: Oxygen, hydrogen and nitrogen evolution during 5 hours of photocatalytic measurements for $\text{Sr}_{(1-x)}\text{La}_x\text{Ti}(\text{O},\text{N})_3$ oxynitrides.

The photocatalytic activity of the samples $\text{Sr}_{(1-x)}\text{La}_x\text{Ti}(\text{O},\text{N})_3$ (chapter 6) synthesized by Pechini method was also investigated. The largest H_2 evolution was found for LaTiO_2N . Hydrogen evolution was only observed for $x = 0$ and $x = 1$, with 6.8 and 22 μmol , respectively. While sample $x = 0$ did not show activity for oxygen evolution, the compounds $x = 0.25$, 0.5 and 1 have approximately the same O_2 production rate of 26 μmol in 5 hours of reaction. For $x = 0.75$ the evolution of O_2 showed the highest value of 200 μmol . That is more than five times higher than found for CaNbO_2N the best photocatalyst in Figure 6.9, with O_2 production of 37 μmol in 5 h. Nitrogen evolutions was not observed for any photocatalyst, which means that the samples are stable and do not decompose during the photocatalytic experiments.

As discussed in the beginning of the chapter the water splitting study was a to get a first impression about the photocatalytic activity of the oxynitride perovskites. Most of the samples have the ability to reduce/oxidize aqueous solution in H_2 and/or O_2 under visible light. Probably when only one product of the water splitting was evolved the band gap positions of the oxynitride did not fit with the expected values for water oxidation (O_2 evolution) or hydrogen reduction (H_2 formation). The band gap position of the studied oxynitrides is not yet known and unfortunately no systematic conclusions can therefore be developed. Nevertheless the obtained results encourage new studies on this field. At least two parameters could be investigated: the surface area of the samples should be increased to improve the H_2/O_2 evolution (as discussed in chapter 7.3 for acetone decomposition) and different co-catalysts could be tested to find out the best coupling co-catalyst/oxynitrides for water reduction.

7.3. Gas Phase Decomposition of Acetone

The photocatalytic evolution of H₂ and O₂ from aqueous solutions have been intensively investigated using oxynitride perovskites as photocatalysts [16, 17, 20, 21, 24, 26, 34, 35]. On the other hand, to the best of our knowledge, the photocatalytic decomposition of organic molecules by oxynitrides was not yet reported. To examine whether oxynitride perovskites are applicable for air purification, for example to reduce disturbing odors, the photocatalyzed decomposition of simple organic molecules in air was studied. In closed rooms, such as kitchen, hotels and pubs ultra violet light cannot be employed to promote the photocatalytic decomposition of odor molecules, because of its damaging effect on the human health as skin burning and eyes injury. Therefore, it is necessary to have the photocatalysts activated only by the visible part of the light spectrum.

An infrared spectrometer (Bruker Equinox 55) was used to measure in-situ the photocatalytic activity of the samples. Different organic molecules have been tested as methane, methanol, iso-propanol, toluol, acetone and aniline. Acetone was chosen because it is highly volatile and can easily be detected by its carbonyl group absorption peak. Furthermore, its oxidation products CO₂ and H₂O are also easy to detect by infrared spectroscopy and no intermediate products were formed as in the case of methylene blue. For the investigations a special reaction vessel was designed in which the oxynitride film is placed in a quartz tube reactor closed by KBr windows. The film was illuminated by a 150 W Xenon lamp. The composition of the gas atmosphere inside the reactor was measured online with an IR laser beam passing through the KBr windows. To cut off the UV part of the light a 420 nm filter was used in all performed experiments. The in-situ measurement using the IR set-up was improved during the course of the investigations. For example, for the spectrometer a new door with a quartz window and an UV-filter holder was constructed. Before this change the IR was let opened during the measurements (because its door was not transparent) and the measured CO₂ concentration was instable due to the influence of the atmosphere in the laboratory. A better reactor completely tight and equipped with extern valves was also built. Before the reactor was not properly tight, resulting in acetone leakages. The use of external valves avoids opening the door of the IR device to flush the reactor with synthetic air and to introduce acetone, consequently the system is free of external CO₂. In the final set-up a system using a syringe and diaphragm with constant gas flow allowed the injection of the same quantity of

acetone in all measurements. This made comparisons among the results obtained for the different photocatalysts more reliable. In a typical experiment, the reactor was flushed several times with synthetic air. Then 5 μl acetone was injected in the diaphragm and the valve connected to the synthetic air cylinder with a gas flow of 15 ml/min was opened for 30 seconds. A photograph of the injection system is shown in Figure 7.11. After this time the lamp was switched on. The on-line measurements were recorded for 800 minutes. The oxynitride perovskite powders were spread as thin films on glass slides. These films are made by mixing the powder with iso-propanol to form a viscous paste using mortar and pestle. The paste was doctor bladed onto microscopy glass laminas as shown in Figure 7.12, and dried at room temperature overnight. The dimension of the films was 20 mm x 55 mm. The thickness of 40 μm was determined by the adhesive tape used to delimitate the border of the films. The blank measurement was done with the same conditions but using a clean microscopy glass lamina as sample. A photograph of the used final set-up is shown in Figure 7.13.

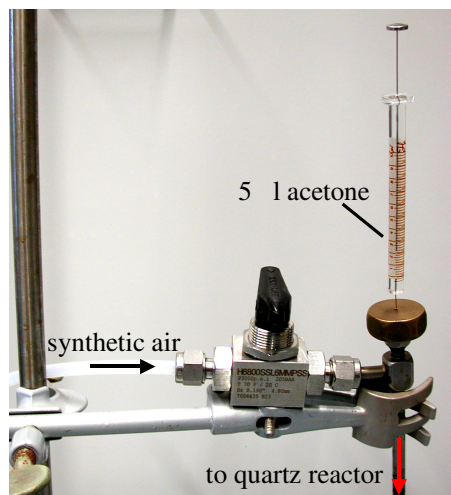


Figure 7.11: Photograph of the injection system.

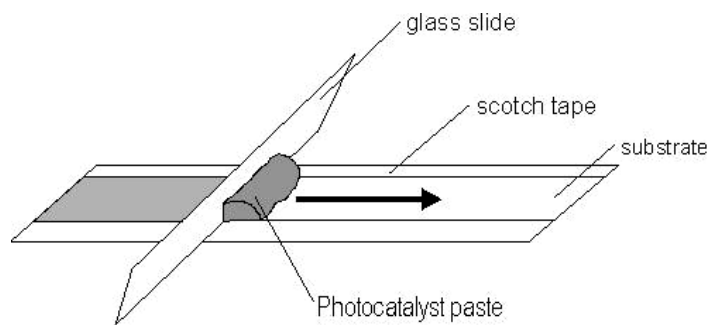


Figure 7.12: Schematic drawing of doctor blade technique [36].

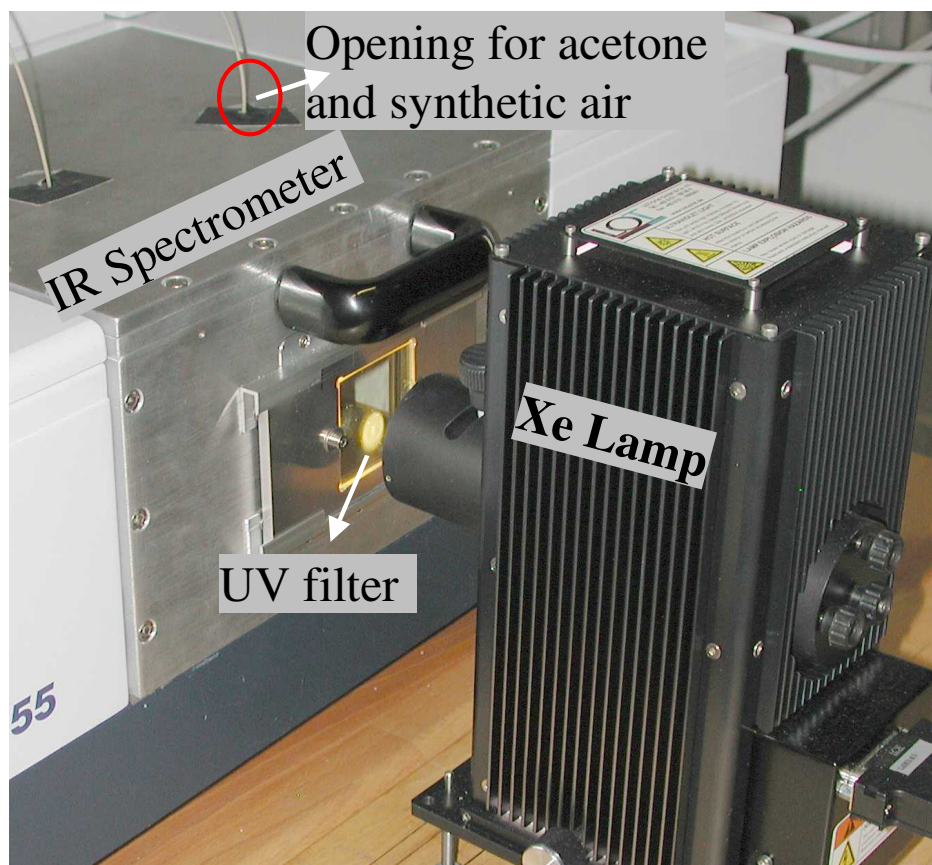
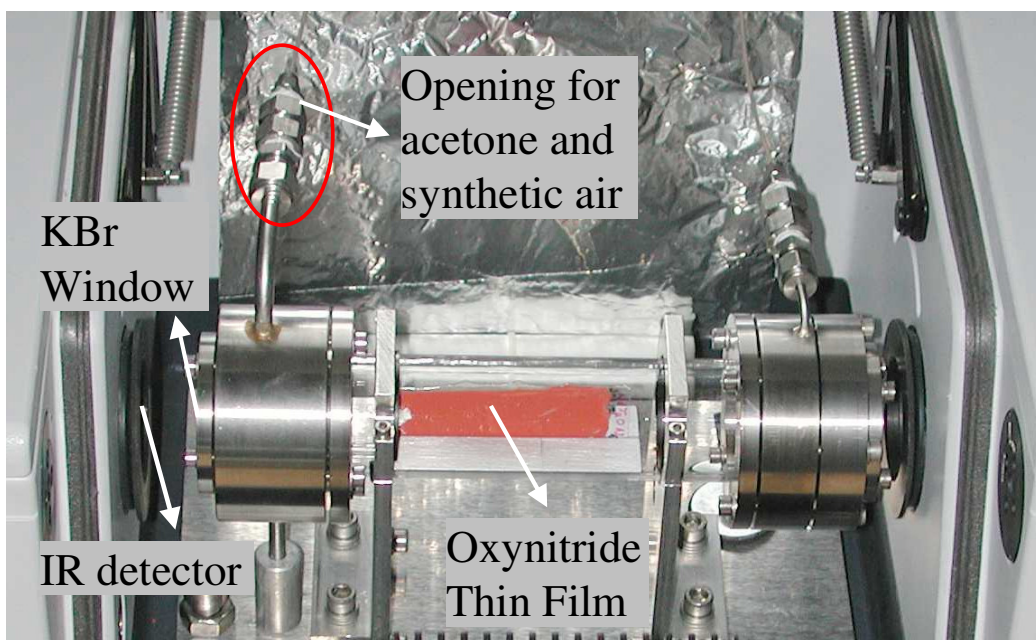


Figure 7.13: Photograph of the quartz reactor with the oxynitride thin film (top) and of the closed infrared device with the xenon lamp (bottom) used for the photocatalysis experiment.

Figure 7.14 shows the IR spectra during a typical acetone photodecomposition experiment. The left graphic is a pseudo-3D plot of the intensity change with increasing irradiation time. The most characteristic peaks are marked. In the right part of the figure peaks related to acetone (1150-1280, 1600-1820, 2800-3100 cm^{-1}), CO_2 (600-765, 2250-2400 cm^{-1}) and water (1400-1750, 3550-3750 cm^{-1}) are plotted for the beginning and ending of the reaction. As can be seen, the intensities of the acetone peaks drastically decrease with time. Absorption peaks due to CO_2 and H_2O were not present at the beginning but evolve with time. It can therefore be concluded that during the photocatalytic decomposition acetone is totally oxidized to CO_2 and water in the presence of light.

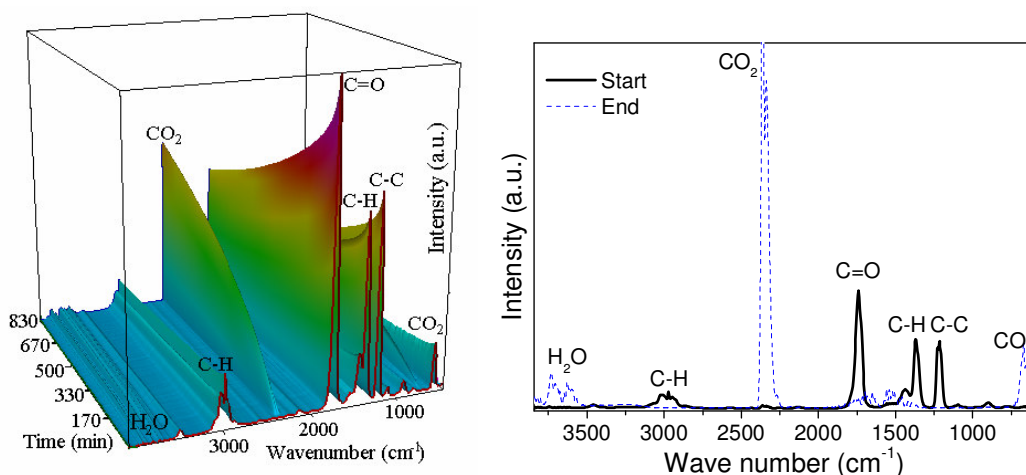


Figure 7.14: Typical FTIR 3D graphic obtained during photodecomposition of acetone (left). Acetone, CO_2 and water correlated peaks for the start and end point of the photocatalysis reaction (right).

The photocatalytic results for the different oxynitride samples are plotted at Fig. 7.15. The intensity of the $\text{C}=\text{O}$ peak was integrated in the wavenumber range 1664-1834 cm^{-1} . The peak intensities were normalized with respect to their intensity at the beginning of reaction, and the blank measurement was subtracted from the curves. For all samples the concentration of $\text{C}=\text{O}$ decreases with time, indicating that all of them have the capability to decompose acetone under visible light irradiation. Four samples showed an even better activity than P25. The one with the fastest decomposition rate was NdTaON_2 , followed by LaTiO_2N prepared by the Pechini method, CaNbO_2N and SrNbO_2N , respectively. These results show that oxynitride-based compounds are in fact promising candidates for the gas phase decomposition of

simple organic compounds. In this context it should be taken into account that the high activity of P25 is to a large extent due to its high surface area.

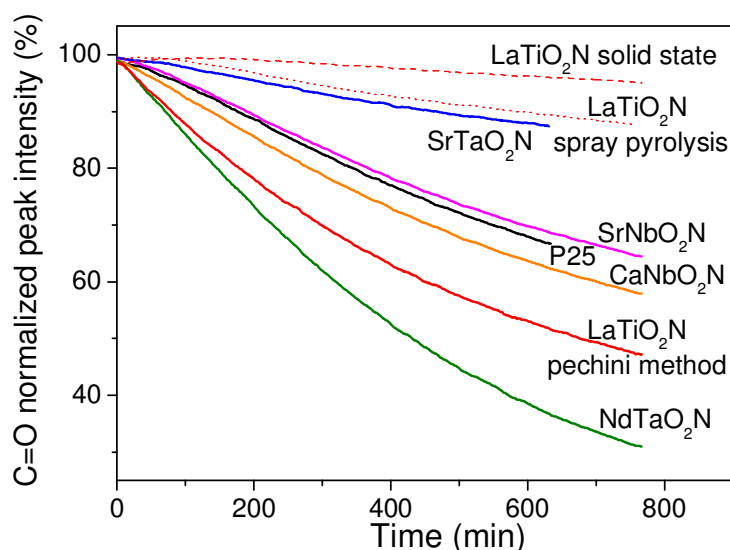


Figure 7.15: Normalized integrated C=O peak intensity *versus* time for different photocatalysts.

The influence of the specific surface area on the photocatalytic activity of the oxynitrides was investigated using LaTiO₂N as test material. Three samples, synthesized by solid-state reaction (sec. 3.2.1), Pechini method (sec. 3.2.2) and spray pyrolysis (sec. 3.2.3) with BET surfaces of 3.6, 13.7 and 10 m²/g, respectively, were measured. As expected the sample with lowest surface area, i.e. LaTiO₂N prepared by solid-state reaction, showed a much lower photocatalytic activity. After 11 hours (660 min) of reaction, the sample decomposed only 3.7% while the one synthesized by Pechini method decomposed 46.5% of the total acetone inside the reactor. The sample synthesized by spray pyrolysis have an intermediate surface area and an intermediate photocatalysis active after 11h of reaction it decomposed 11.8% of acetone. P25, for comparison, has a surface area value of approximately 50 m²/g while the tested oxynitrides showing a better performance than P25 only exhibited values around 10 m²/g. It is therefore reasonable to assume that oxynitrides with a comparable specific surface would show much higher reaction rates than titanium dioxide. Since the surface area has such a strong influence on the photocatalytic activity of the oxynitrides, a direct comparison of the different samples is not possible because they show variable BET surface areas.

One of the problems of all investigated oxynitride perovskites is that they have to be submitted to high temperature (between 700-1050°C) during long periods of time (minimum 10 hours) to allow the introduction of nitrogen on the crystal structure, yielding the respective oxynitride phases. This heat treatment increases the particle sizes of the materials due to sintering and in turn decreases the specific surface area of the catalysts. This results in a smaller number of active sites for the redox reactions and consequently reduces the photocatalytic activity of the oxynitride compounds. The active surface area is actually one of the most important issues for photocatalysis as shown above for LaTiO_2N prepared by different routes and little has been discussed in the field of oxynitrides to improve this parameter. In the following the photocatalytic activity for the gas phase decomposition of acetone by $\text{LaTi}(\text{O},\text{N})_3$ nanoparticles is discussed. The samples were prepared by the polyol technique (sec. 3.2.4) and ammonolyzed at 800°C, 870°C, 920°C and 1000°C. They are named in the following text as sample 800, sample 870, sample 920 and sample 1000, respectively. Special emphasis is given to the influence of the ammonolysis temperature and its effect on particle size, surface area and nitrogen content.

The UV-Vis diffuse reflectance spectra of the nanoparticle samples are shown in Fig. 7.16. The absorption edge shifts to lower energies (longer wavelengths) with increasing temperature of ammonolysis.

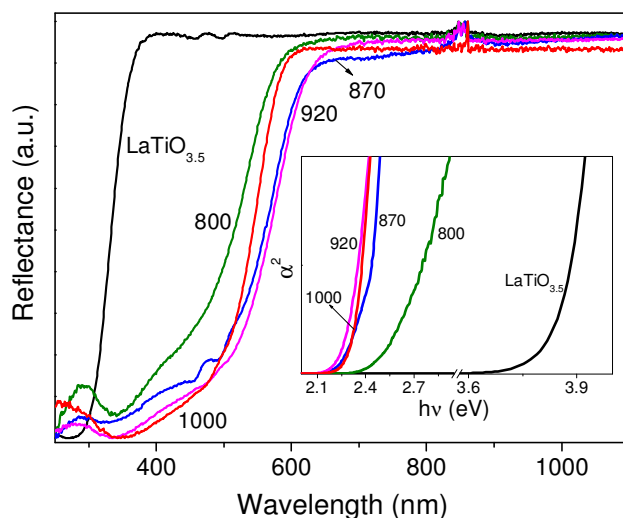


Figure 7.16: UV-vis diffuse reflectance spectra of the $\text{LaTi}(\text{O},\text{N})_3$ samples ammonolyzed at temperatures between 800°C and 1000°C.

The corresponding color impression of the powder gets gradually darker, starting from orange for sample 800, passing through red (sample 870 and 920) to brown (sample 1000). The band gaps were calculated assuming a direct allowed band gap transition [37]. The plot is shown as inset in Figure 7.16 and the resulting values are listed in Table 7.2. Although the band gap values may have a considerable uncertainty, the general trend is obvious. The band gaps decrease from roughly 2.6 eV to 2.3 eV with temperature of nitridation, since at higher temperature more nitrogen is incorporated on the crystal structure as discussed bellow. The band gap values of sample 1000 and 920 are quite similar because they have almost the same nitrogen content.

Table 7.2: Surface area, particle size, nitrogen content and optical band gap for the $\text{LaTi}(\text{O},\text{N})_3$ samples ammonolyzed at different temperatures for 3 h.

$\text{LaTi}(\text{O},\text{N})_3$ ammonolyzed at $T(^{\circ}\text{C})$	BET Surface Area (m^2/g)	Particle Size ¹ (nm)	N/(N+O) ratio ²	Band Gap ³ (eV)
800	44	10	0.082	2.60
870	26	18	0.225	2.41
920	19	22	0.315	2.28
1000	16	28	0.325	2.30

¹ Calculated by the Scherrer equation (thickness, $t = 0.9 \lambda / (B \cos\theta_B)$, where λ is the x-ray wavelength and B is the full-width at half maximum of the most intense peak at $2\theta \approx 32^{\circ}$)

² Obtained from ERDA analysis (chapter 2.7.3)

³ Calculated using Kubelka-Munk equation and considering direct allowed band gap transition (chapter 2.4)

ERDA analyses were performed to quantify the N/(N+O) ratio. For sample 1000 the experimentally found value of 0.325 is very close to the expected value of 1/3 in LaTiO_2N , proving that the sample has completely reacted. While for sample 920 the N/(N+O) ratio is still above 0.3 it decreases to 0.08 for the sample ammonolyzed at 800°C . The N/(N+O) ratios given in Table 7.2 correspond to 28 %, 71 %, 95 %, and 98 % completeness of the reaction for samples 800, 870, 920, and 1000, respectively. $\text{LaTiO}_{3.5}$ consists of layers of perovskite blocks with a thickness of four octahedra slabs. During nitridation these blocks are connected to yield the (distorted) cubic perovskite structure that can be considered the $n = \infty$ end member of the [110]-phases introduced in chapter 1. During this process all possible phases with $4 < n < \infty$ may form on an atomic scale. As a consequence the

periodic repetition of the layering is destroyed and only the diffraction peaks corresponding to the crystalline product LaTiO_2N are observed (see x-ray diffraction patterns in Figure 3.16).

The results of the photocatalysis measurements are plotted in Fig. 7.17. A comparison of the four samples is done for the acetone-related peaks [$\text{C}=\text{O}$ ($1664\text{--}1834\text{ cm}^{-1}$), C-C ($1147\text{--}1271\text{ cm}^{-1}$) and C-H ($2883\text{--}3167\text{ cm}^{-1}$)] and for the resulting products CO_2 ($2235\text{--}2405\text{ cm}^{-1}$) and H_2O ($3528\text{--}3979\text{ cm}^{-1}$). The intensity of each peak was integrated in the specified wavenumber range given in parenthesis. The acetone related peaks were normalized with respect to their intensities at the beginning of reaction and subtracting the blank run. Since the peak intensities for $\text{C}=\text{O}$ and C-C bonds show almost identical behavior, only the graphic for $\text{C}=\text{O}$ is plotted in Figure 7.17a. From Figure 7.17a it can be seen that the sample 870 is the one that decomposes $\text{C}=\text{O}$ and C-C bonds fastest, followed by the samples 800 and 920. The sample 1000 had no significant activity.

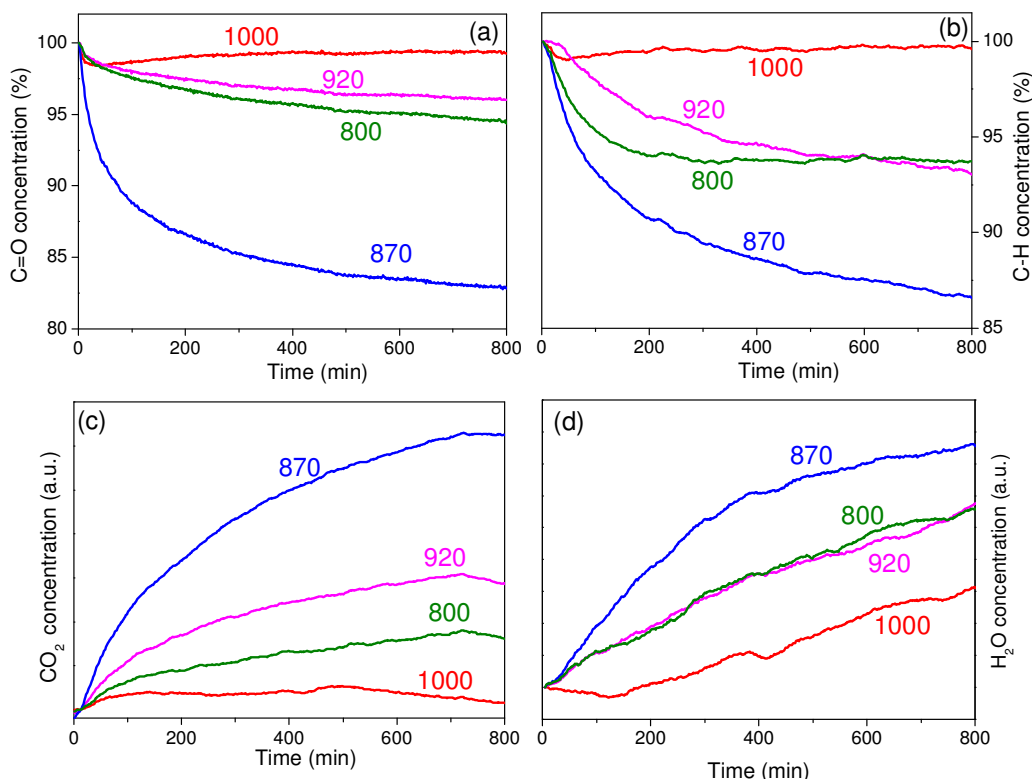


Figure 7.17: Decomposition of $\text{C}=\text{O}$ and C-H bonds (top) and CO_2 and H_2O formation (bottom).

For the IR signals corresponding to the C-H bonds a similar behavior was observed as depicted in Figure 7.17b. Again, sample 870 decomposes the C-H bonds fastest, followed by sample 800 and 920. Sample 1000 does not decompose the C-H bonds. Considering the concentrations of the photoreaction products it was found that the activity for CO₂ evolution follows the order sample 870 > 920 > 800 > 1000. With respect to water evolution, the sample 870 is again the most active, followed by samples 920 and 800. The sample 1000 was the one that produced less water.

The following conclusions can be drawn from the outlined results: the sample 870 has the highest photocatalytic activity as it decomposes C=O, C-C and C-H bonds fastest and produces the largest quantities of water and carbon dioxide. The samples 800 and 920 show almost the same behavior for C=O, C-C and C-H bonds decomposition and for water and CO₂ formation. The sample 1000 shows the same behavior as the blank measurement, which means it possesses no photocatalytic activity.

The summary of the photocatalytic activity of the different samples is plotted in Figure 7.18. The data points correspond to the percentage of the normalized C=O intensity at the end of the photocatalytic reaction, subtracting the value obtained for the blank run. Looking at the parameters listed in Table 7.2, it can be stated that the ammonolysis temperature leads to a systematic change of the physical properties. With higher reaction temperature the particle size increases while simultaneously the specific surface area is reduced. A higher nitridation temperature also results in higher nitrogen contents and smaller band gaps.

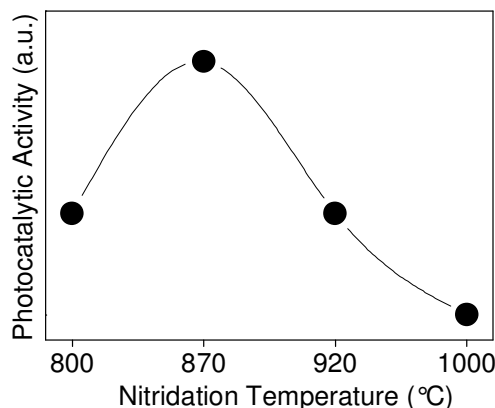


Figure 7.18: Photocatalytic activity of the oxynitrides LaTi(O,N)₃ ammonolyzed at different temperatures.

The most active photocatalyst was the sample 870, which has a surface area of $26\text{m}^2/\text{g}$ and a band gap of 2.41 eV . The sample 800 has a higher surface area but on the other hand also a larger band gap, while the sample 920 has smaller band gap but a smaller surface area. These two properties apparently compensate each other and as a result the latter two samples show a similar photocatalytic activity. Surprisingly, the sample 1000 did not show any considerable activity although it possesses a relatively small band gap. Its low photocatalytic efficiency may on the one hand be due to the smaller specific surface area. On the other hand, a value of $16\text{ m}^2/\text{g}$ is still considerably large so the reduced surface cannot be the only reason for the missing activity. From the catalytic measurements it can be concluded that besides a high surface area, well adjusted light absorption properties as well as the presence of some unreacted layered oxide are important requirements for a high photocatalytic activity.

Our results are similar to finding of a recent study on the hydrogen production from water-methanol mixtures using nitrogen-doped $\text{SrNbO}_{3.5}$ as photocatalyst. The parent oxide has the same $n = 4$ layered perovskite structure as $\text{LaTiO}_{3.5}$ and the highest photocatalytic activity was also observed for an intermediate nitrogen concentration [17]. It is known that layered perovskites often show high photocatalytic activities because their interlayer space can act as reaction sites and the electron-hole pair recombination process is retarded by physical separation between the slabs [38]. Nitrogen introduction in the oxide lattice decreases the band gap and the samples absorb visible light. On the other hand, a high level of N-doping leads to a collapse of the layered structure. These findings are a hint that the photocatalytically active phase may indeed be the layered oxide with a medium nitrogen doping level, which is sufficient to lead to an activation by shifting the absorption edge to the visible light region but is too low to destroy the layered structure of the perovskite. An optimal catalytic activity would therefore be a compromise between a maximum surface area, a tailored band gap value and an adjusted ratio of parent oxide/oxy-nitride.

In summary, the investigations of methylene blue decomposition in aqueous solution were difficult by the fact that the dye has a complex chemical structure and the intermediated reactions were not identifiable. Another problem was that the samples adsorbed the dye on their surfaces. Therefore these investigations were not continued. In the water splitting study many of the oxynitrides samples showed

considerable activity to yield oxygen and/or hydrogen from water solutions. Probably when only one product of the water splitting was evolved the band gap positions of the oxynitride did not fit with the expected values for water oxidation or hydrogen reduction. As discussed before, the band gap positions of the studied oxynitrides are not yet known and therefore no systematic conclusion can be done. The oxynitride samples have also shown good photocatalytic efficiency in the investigations of gas phase decomposition of acetone. The active surface area of the samples is an important parameter for photocatalysis as demonstrated using LaTiO₂N prepared by different synthesis technique. It was confirmed that for an ABO_{3.5} layered perovskite the partially ammonolyzed compound gives the best photocatalysis results. Because the absorption edge is shifted to the visible light region and the layered structure is partially kept.

References

- [1] <http://photoscience.la.asu.edu/photosyn/education/photointro.html>. 2008.
- [2] S. Malato, J. Blanco, A. Vidal, C. Richter, *Appl. Cat. B: Environmental* 37 (2002) 1.
- [3] K. Kabra, R. Chaudhary, Sawhney R.L., *Ind. Eng. Chem. Res.* 43 (2004) 7683.
- [4] <http://www.cru-z.com/arc-e/>. 2007.
- [5] J. Peral, X. Domènech, D. F. Ollis, *J. Chem. Technol. Biotechnol.* 70 (1997) 117.
- [6] F. E. Osterloh, *Chem. Mater.* 20 (2008) 35.
- [7] M. Matsuoka, M. Kitano, M. Takeuchi, K. Tsujimaru, M. Anpo, J. M. Thomas, *Catalysis Today* 122 (2007) 51.
- [8] <http://www.nrel.gov/hydrogen/> National Renewable Energy Laboratory, U.S.Department of Energy. 2007.
- [9] K. Hashimoto, H. Irie, A. Fujishima, *Jpn. J. Appl. Phys.* 44 (2005) 8269.
- [10] H. Kato, A. Kudo, *Catalysis Today* 78 (2003) 561.
- [11] H. Kato, A. Kudo, *J. Photochem. Photobiol. A* 145 (2001) 129.
- [12] M. Uno, A. Kosuga, M. Okui, K. Horisaka, S. Yamanaka, *J. Alloys Compd.* 400 (2005) 270.
- [13] S. Ikeda, A. Tanaka, K. Sinohara, M. Hara, J. N. Kondo, K. Maruya, K. Domen, *Micropor. Mater.* 9 (1997) 253.
- [14] K. Domen, S. Naito, T. Onishi, K. Tamaru, *Chem. Phys. Lett.* 92 (1982) 433.
- [15] <http://thinkorthwim.com/index.php?tag=sunscreen>. 2008.
- [16] A. Kasahara, K. Nukumizu, T. Takata, J. N. Kondo, M. Hara, H. Kobayashi, K. Domen, *J. Phys. Chem. B* 107 (2003) 791.
- [17] S. M. Ji, P. H. Borse, G. K. Hyun, D. W. Hwang, J. S. Jang, S. W. Bae, J. S. Lee, *Phys. Chem. Chem. Phys.* 7 (2005) 1315.
- [18] A. Kasahara, K. Nukumizu, G. Hitoki, T. Takata, J. N. Kondo, M. Hara, H. Kobayashi, K. Domen, *J. Phys. Chem. A* 106 (2002) 6750.
- [19] D. Yamasita, T. Takata, M. Hara, J. N. Kondo, K. Domen, *Solid State Ionics* 172 (2004) 591.
- [20] M. Liu, W. You, Z. Lei, T. Takata, K. Domen, C. Li, *Chin. J. Catal.* 27 (2006) 556.
- [21] M. Liu, W. You, Z. Lei, G. Zhou, J. Yang, G. Wu, G. Ma, G. Luan, T. Takata, M. Hara, K. Domen, C. Li, *ChemComm* (2004) 2192.

- [22] J. A. Schottenfeld, A. J. Benesi, P. W. Stephens, G. Chen, P. C. Eklund, T. E. Mallouk, *J. Solid State Chem.* 178 (2005) 2313.
- [23] F. Grasset, G. Starukh, L. Spanhel, S. Ababou-Girald, D. S. Su, A. Klein, *Adv. Mat.* 17 (2005) 294.
- [24] T. Hisatomi, K. Hasegawa, K. Teramura, T. Takata, M. Hara, K. Domen, *Chem. Lett.* 36 (2007) 558.
- [25] Y. Lee, H. Terashima, Y. Shimodaira, K. Teramura, M. Hara, H. Kobayashi, K. Domen, M. Yashima, *J. Phys. Chem. C* 111 (2007) 1042.
- [26] X. Sun, K. Maeda, M. Le Faucheur, K. Teramura, K. Domen, *Appl. Cat. A: General* 327 (2007) 114.
- [27] R. W. Matthews, *Wat. Res.* 25 (1991) 1169.
- [28] J. Tang, Z. Zou, J. Ye, *Angew. Chem. Int. Ed.* 43 (2004) 4463.
- [29] A. Houas, H. Lachheb, M. Kisib, E. Elaloui, C. Guillard, J. M. Herrmann, *Appl. Cat. B: Environmental* 31 (2001) 145.
- [30] H. Gnaser, M. R. Savina, W. F. Calaway, C. E. Tripa, I. V. Veryovkin, M. J. Pellin, *Int. J. Mass Spect.* 245 (2005) 61.
- [31] T. Zhang, T. Oyama, A. Aoshima, H. Hidaka, J. Zhao, N. Serpone, *J. Photochem. Photobiol. A: Chem.* 140 (2001) 163.
- [32] I. A. Salem, M. S. El-Maazawi, *Chemosphere* 41 (2000) 1173.
- [33] A. Mills, J. Wang, *J. Photochem. Photobiol. A: Chem.* 127 (1999) 123.
- [34] K. Maeda, K. Domen, *J. Phys. Chem. C* 111 (2007) 7851.
- [35] A. Kasahara, K. Nukumizu, G. Hitoki, T. Takata, J. N. Kondo, M. Hara, H. Kobayashi, K. Domen, *J. Phys. Chem. A* 106 (2002) 6750.
- [36] C. Zilverentant, PhD Thesis, Technique University Delft 2003.
- [37] X. Gao, I. E. Wachs, *J. Phys. Chem. B* 104 (2000) 1261.
- [38] J. Kim, D. W. Hwang, H. G. Kim, S. W. Bae, J. S. Lee, W. Li, S. H. Oh, *Topics in Catalysis* 35 (2005) 295.

8. Thick Oxynitride Perovskite Layers

Thin films of oxynitrides are required for applications like colored surfaces and photoelectric cells. On the other hand, oxynitride single crystals would be ideal for intrinsic electric and dielectric properties measurements and for structure analysis. Experiments using single crystals also permit to measure physical properties in different crystalline directions, which are not possible using polycrystalline samples. Different techniques have been employed to prepare oxynitride perovskite films. Spin coating and pulsed laser deposition (both in section 6.2) have been used to produce $\text{Sr}_{(1-x)}\text{La}_x\text{Ti}(\text{O},\text{N})_3$ thin films. While spin coating resulted in random crystallized layers PLD gives epitaxially films. The oxynitride systems BaTaO_2N and $\text{SrMo}(\text{O},\text{N})_3$ have also been successfully grown by PLD technique [1, 2]. RF sputtering has been used to produce LaTiO_2N . This method results in good oriented thin layers as well [3]. To the best of our knowledge, single crystals of oxynitride perovskites have not been synthesized yet. The reason is that the materials cannot be molten and decompose at high temperatures. The best samples obtained so far are thin epitaxial layers grown by PLD or RF-sputtering.

In this chapter the preparation of nearly single-crystalline oxynitride films of several micrometer thickness is described. The basic idea of the experiment is not to grow the oxynitrides on the surface of an inert single crystalline substrate but to use the single crystal itself as reactant. The advantages are obvious: the lattice mismatch is minimal and the correct cationic composition is already fixed.

Crystals were grown by the floating zone technique. The applied high temperature furnace (model GERO SPO) is equipped with two 1000 W halogen lamps, gold-coated ellipsoidal mirrors, water-cooling system and diverse gas entrances. The gold-coated mirrors focus the radiation of the lamps on a small area of an oxide bar. The oxide material heats up and melts. The power of the lamps can be adjusted to an ideal temperature in which a small region of the oxide is melted but with sufficient viscosity to connect the two oxide bars (seed and feed, explained in more detail in the next paragraph). At the beginning of the experiment the top of the seed bar and the lower part of the feed are melted and then the two bars are connected. Afterwards, the bars move down and consequently the molten zone moves up. The lower part of the bar is cooled down and small crystallites are formed. Subsequently, a “bottle neck” is

intentionally built to decrease the number of crystallites. When the experiment is successful only one crystal is formed. The growth rate was adjusted between 4-10 mm/h, depending on the oxide system. The Figure 8.1 (a) is a photograph of the used furnace. During the crystal growth oxide seed and feed rods were counter rotated with a speed varying between 5-30 rpm inside a quartz tube. The quartz tube is required to protect the gold coated mirrors and to allow the use of different gases during the crystal growth. With the use of thick-walled tube gas pressures until 6 bar can be applied. A constant flow of synthetic air (0.2 l/min) at ambient pressure was used as gas atmosphere. Figure 8.1 (b) shows a projected image of a crystal growth experiment. The molten region is the brightest one in the middle, above is the feed rod and below is the formed crystal. The resulting crystal boules have typical lengths of at least 1 cm and 3-6 mm diameter. A photo of a typical crystal boule is shown in Fig. 8.1 (c).

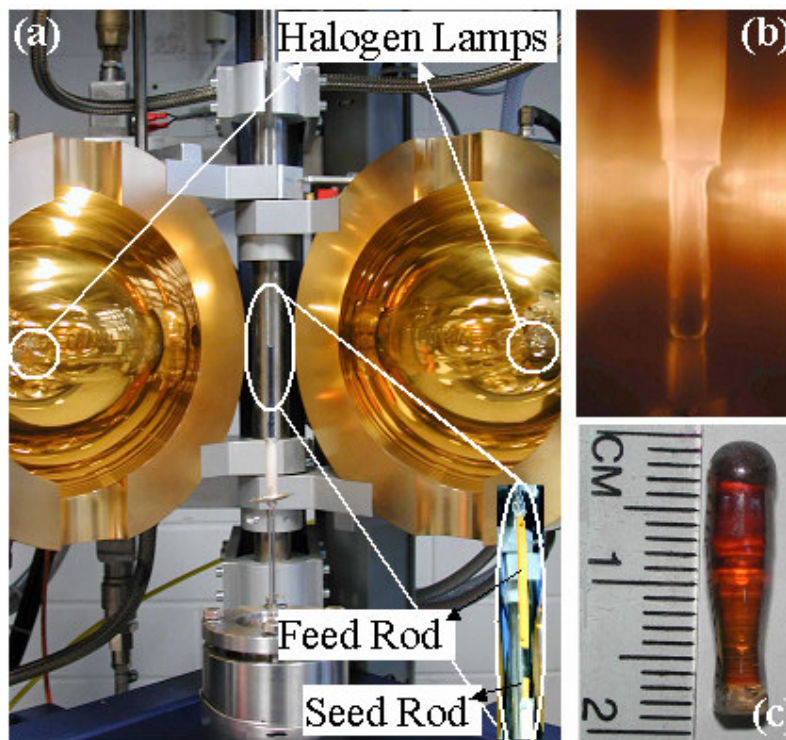


Figure 8.1: (a) Floating zone furnace, (b) the growth experiment and (c) a typical crystal boule (SrTiO_3).

Polycrystalline samples of $\text{Sr}_{(1-x)}\text{La}_x\text{TiO}_{(3+x/2)}$, with $0 \leq x \leq 1$, LaTaO_4 , $\text{LaTiO}_{3.5}$, $\text{NdTiO}_{3.5}$, $\text{SrTaO}_{3.5}$ and $\text{SrNbO}_{3.5}$ were prepared by conventional solid-state reactions (sec. 3.2.1). The oxides/carbonates precursors were mixed using mortar and

pestle. Afterwards the mixtures were heated at 1100°C for 48 h in a box furnace under air. For some compositions intermediate grinding was necessary. The resulting powders were pressed in rectangular bars of 85×5×5 mm³ and 15×3×3 mm³ that served as feed and seed rod, respectively, for the crystal growth experiment. The bars were sintered at 1300-1450 °C (depending on the melting point of the material) for 24 h to increase their density and mechanical stability.

Numerous attempts to prepare single crystalline oxynitrides in-situ by crystal growth experiments in (diluted) ammonia atmospheres were performed. None of these trials was successful instead they resulted in the formation of (partly reduced) oxides. The first try was using oxide stabs of SrNbO_{3.5} under 8% NH₃ in N₂ atmosphere. During the crystal growth enormous gas bubbles were formed in the melting region what make impossible the crystal formation. Experiments starting with oxynitride stabs of SrNbO₂N, LaTiO₂N and SrTaO₂N under 1, 2 and 4% NH₃ in N₂ atmosphere were also tried. It was not possible to grow crystals because bubbles were formed in the molten phase. Black pieces were obtained, that were the respective reduced ABO₃ phase, as confirmed by x-ray analysis. To try to avoid the reduction power of ammonia experiments under NO₂ were also performed. SrTaO₂N was melted under 2 % NO₂ in N₂ atmosphere. Some bubbles were also observed in the molten zone and a completely oxidized crystal was obtained, i.e. SrTaO_{3.5}. Since the direct oxynitride single crystals growth did not work as expected, the idea was to ammonolyze the oxide crystals.

The preparation of single crystals of the system Sr_(1-x)La_xTiO_(3+x/2) was tried, since the synthesis of these compositions as thin films was achieved without big problems. The synthesis of the end members LaTiO_{3.5}, SrTiO₃, x = 0.1 and 0.2 was successful. However, it was not possible to synthesize the intermediate compositions with 0.3 ≤ x ≤ 0.9 as single phase crystal. Phase separation was observed and the obtained crystal boules showed grayish colors and rough surfaces. Figure 8.2 shows photos of two grown boules that represent the Sr_(1-x)La_xTiO_(3+x/2) series with 0.3 ≤ x ≤ 0.9. The crushed crystals were examined by powder x-ray diffraction and the results are shown in Figure 8.3. The sample x = 1 is phase pure LaTiO_{3.5}, while the samples x = 0, 0.1 and 0.2 are single phase with the perovskite structure of SrTiO₃. On the other side, the samples with 0.3 ≤ x ≤ 0.9 were formed of mixtures of LaTiO_{3.5} and SrTiO₃.

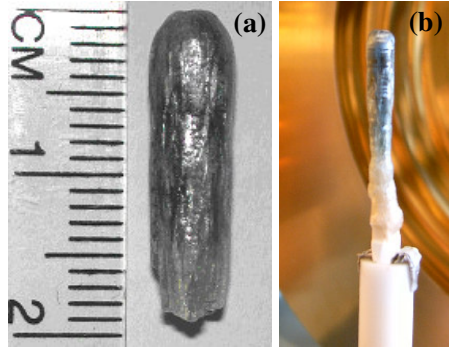


Figure 8.2: Photos of the obtained boules of compositions (a) $x = 0.5$ and (b) $x = 0.9$.

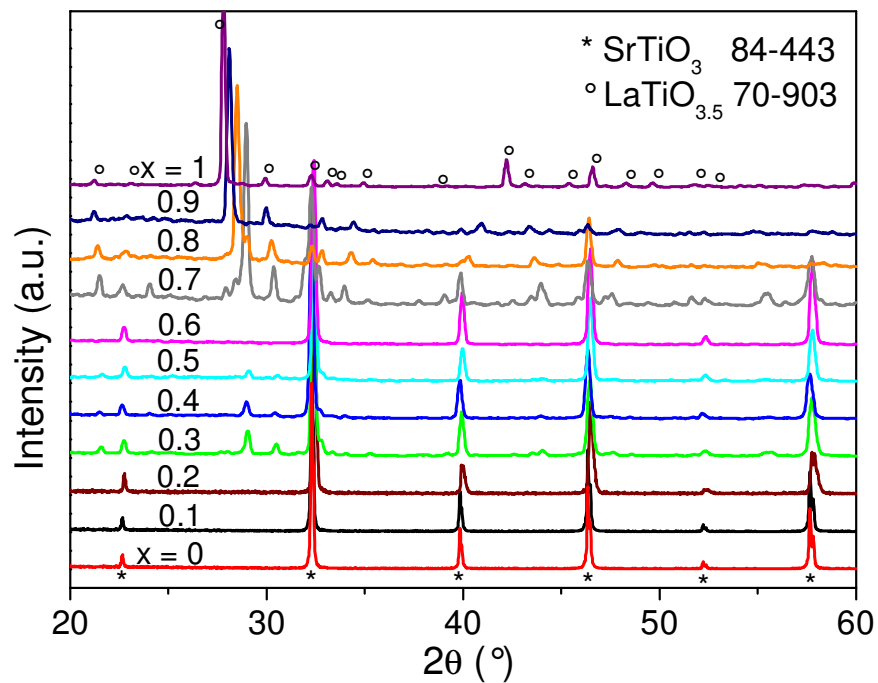


Figure 8.3: X-ray diffraction patterns of the $\text{La}_x\text{Sr}_{(1-x)}\text{TiO}_{(3+x/2)}$ crystals grown by the floating zone technique.

The preparation of single crystals of LaTaO_4 by the floating zone technique was also tried. A boule with a length of ca. 2 cm was obtained, but when it was cooled down it broke in small pieces. The crystal shattered because LaTaO_4 undergoes a phase transition from orthorhombic (high temperature) to monoclinic at 175°C [4]. The small pieces of LaTaO_4 were ammonolyzed at 900°C for 72 h and 1050°C for 120 h. The obtained samples are named in the following text as sample 900 and sample 1050, respectively. Figure 8.4 shows the x-ray diffraction pattern of the oxide LaTaO_4 and the ammonolyzed compounds. Sample 900 is composed of two phases,

namely LaTaO_4 and LaTaON_2 while sample 1050 is pure LaTaON_2 . The color of the ammonolyzed compounds was dark red/purple.

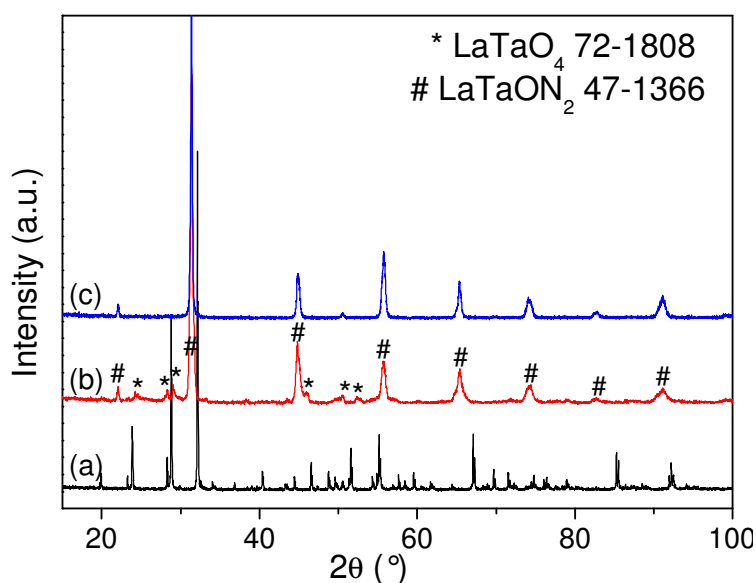


Figure 8.4: X-ray diffraction pattern of the (a) non-ammonolyzed LaTaO_4 , (b) sample 900 and (c) sample 1050.

The small crystals were analyzed by SEM before and after ammonolysis. The oxide sample is shown in Figure 8.5(a). The crystal appears dense without cracks. The sample 900 shows parallel cracks on its surface (Fig. 8.5 (b)) while the sample 1050 is completely cracked with parallel fissures (Fig. 8.5 (c)-(d)). Probably the crystals cracked because of the structural tension during the phase transformation from oxide to oxynitride. While LaTaO_4 is an $A_nB_nO_{3n+2}$ perovskite-related layered structure with $n = 2$ and unit cell volume of 327.22 \AA^3 [4], LaTaON_2 is a three dimensional perovskite with a volume of only 264.13 \AA^3 [5]. During the ammonolysis 3 O^{2-} are substituted by 2 N^{3-} and the TaO_6 octahedra are corner-connected, shrinking the structure volume and causing cracks on the oxynitride single crystals.

The samples have also been analyzed by TEM. Figure 8.6 (a) is a high resolution TEM micrograph of sample 1050. The atomic planes are equidistant, as expected for the 3D oxynitride structure. The distance between the horizontal planes is around 2.8 \AA , which corresponds to the (200) direction while the vertical planes distance is ca. 4.0 \AA corresponding to the (002) direction of the orthorhombic unit cell with $\mathbf{a} = \mathbf{b} = 5.716 \text{ \AA}$ and $\mathbf{c} = 8.084 \text{ \AA}$ [5]. The oxide sample is shown in Figure 8.6(b). In LaTaO_4 the crystal shows a layered structure characteristic for the

LaTaO₄ with $n = 2$. The planes distances are in accordance with the reported monoclinic unit cell with $a = 7.650 \text{ \AA}$, $b = 5.577 \text{ \AA}$ and $c = 7.820 \text{ \AA}$ [6].

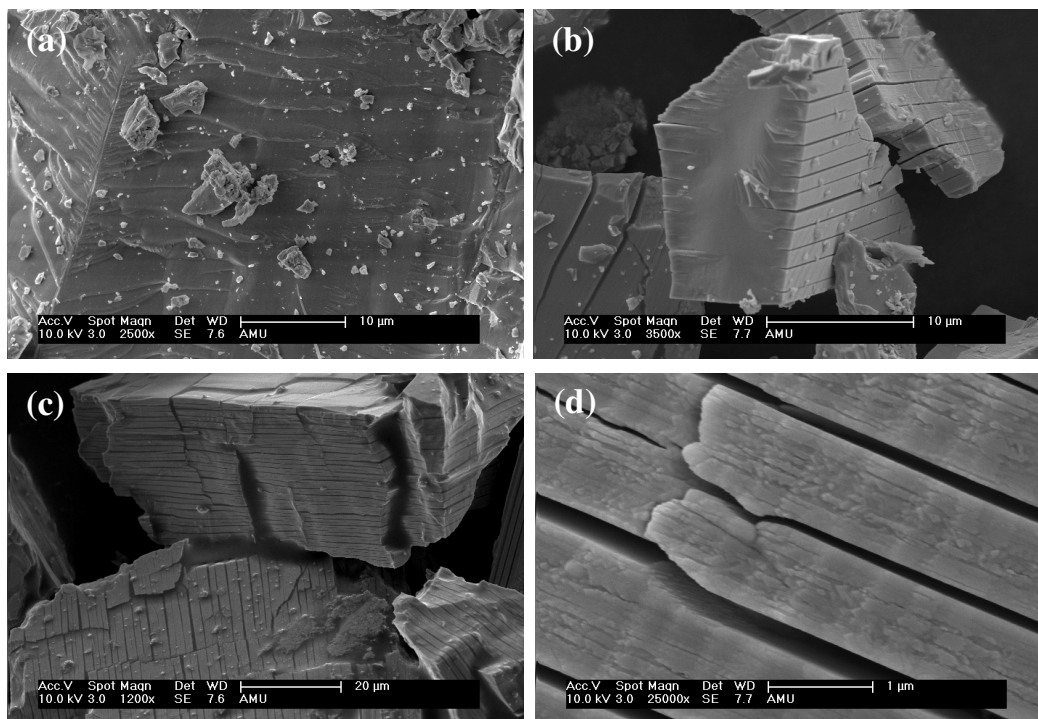


Figure 8.5: Single crystals of (a) LaTaO₄, (b) sample 900 and (c-d) sample 1050.

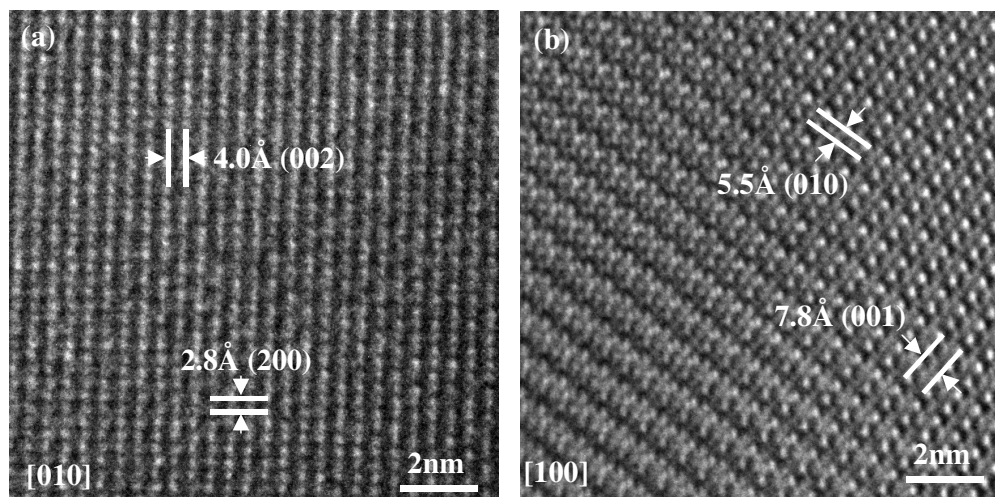


Figure 8.6: HRTEM of (a) LaTaON₂ - sample 1050 and (b) LaTaO₄.

Attempts to solve the structure of the sample 1050 (LaTaON₂) by single crystal x-ray diffraction were not successful. Small crystals (ca. 0.1 x 0.1 mm) were glued on the top of a glass fiber and analyzed in the single crystal diffractometer

Syntex P21. At least 5 crystals were analyzed and the resulted diffraction patterns gave similar results. As example one rotation photograph of a crystal piece taken on the 4-circle diffractometer is shown in Figure 8.7.

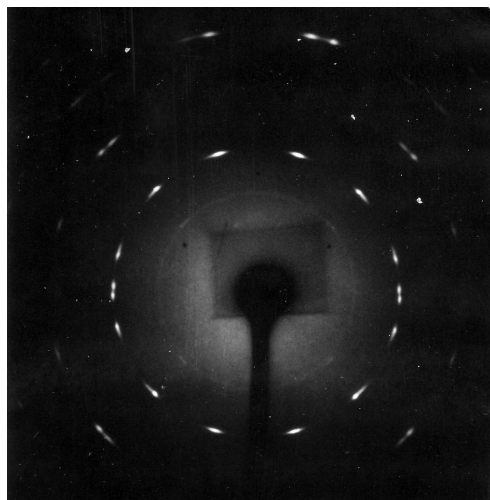


Figure 8.7: X-ray diffraction rotation photo of sample 1050.

It can be seen that instead of sharp reflection points the diffraction pattern shows diffuse spots. The obtained diffraction pattern is typical of crystals that have high mosaicity, i.e. the crystal has several mosaic domains. In the case of LaTaON_2 , the high mosaicity results from the extensive cracking of the crystals as confirmed by SEM (Figure 8.5). This phenomenon makes a structure analysis by single crystal diffraction impossible.

Since the trials to synthesize single crystals of $\text{Sr}_{(1-x)}\text{La}_x\text{TiO}_{(3+x/2)}$ and LaTaO_4 were not successful, layered perovskite systems of the $\text{ABO}_{3.5}$ type were investigated. It was possible to grow crystals of $\text{LaTiO}_{3.5}$, $\text{NdTiO}_{3.5}$, $\text{SrNbO}_{3.5}$ and $\text{SrTaO}_{3.5}$. The crystals were transparent (violet in the case of $\text{NdTiO}_{3.5}$ and colorless for the other samples). Due to the layered crystal structure of the $\text{ABO}_{3.5}$ oxides the obtained boules were easily cleaved yielding thin slices of some hundred micrometer thickness and several square millimeters area. These slices were ammonolyzed in a tube furnace at temperatures between 900 °C and 1050 °C for several hours in an ammonia flow of 50 ml/min. The reaction temperature, time and the color of the ammonolyzed compounds are for $\text{LaTiO}_{3.5}$ 1000 °C, 18 h and 120 h – orange/red; for $\text{NdTiO}_{3.5}$ 1000 °C, 20 h - orange/brown; for $\text{SrNbO}_{3.5}$ 900 °C, 18 h and 76 h – dark brown; and for $\text{SrTaO}_{3.5}$ 1050 °C, 18 h and 120 h - orange. After ammonolysis an oxynitride layer

with ABO_2N composition was formed on top of the oxide crystal slice. A picture of a $SrTaO_{3.5}$ single crystal slice before and after the reaction with NH_3 is shown in Figure 8.8(a). It can be seen that before the ammonolysis the slice is colorless and after it becomes reddish. The photo of the cross section of the 120 h ammonolyzed slice is shown in Figure 8.8(b). The oxynitride layer (brighter - on the top) has a thickness of about 25 μm . The spots on the surface are due to the polishing procedure during sample preparation.

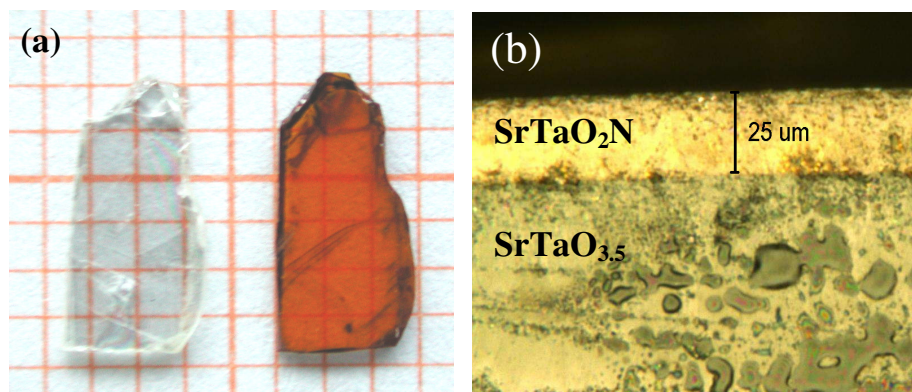


Figure 8.8: Thin slice of a $SrTaO_{3.5}$ crystal (a) before (left) and after (right) ammonolysis (the grid represents $1 \times 1 \text{ mm}^2$) and (b) optical microscopy of the cross section of the ammonolyzed slice.

Electron probe microanalysis (EPMA) was used to verify the incorporation of nitrogen. The left side of Figure 8.9 shows the photograph of a cross section of the 18 h ammonolyzed $LaTiO_{3.5}$ crystal. The line scan of the EPMA nitrogen signal is overlaid. The right part of the figure depicts the comparison of the line scans for the elements oxygen and nitrogen. The results clearly confirm high oxygen and a negligible nitrogen concentration for the inner region of the crystal, indicating that this part has not yet reacted. The rather high baseline level for the nitrogen signal is due to a partial overlap with the titanium signal. For the colored surface layer, the oxygen concentration is significantly decreased while the nitrogen content increases simultaneously, as expected for the reaction $LaTiO_{3.5} \rightarrow LaTiO_2N$. During the ammonolysis the oxygen ions are replaced by nitride ions. As $1.5 O^{2-}$ is substituted by $1 N^{3-}$ the layers lose anions and neighboring slabs (octahedron layers) are linked in a zipper-like mechanism. This proposed mechanism is closely related to the one found during the reduction of $LaTiO_{3.5}$ to $LaTiO_3$ [7]. In both cases the number of anions decreases from 3.5 to 3. While the reaction $ABO_{3.5} \rightarrow ABO_3$ results in a partial

reduction of the transition metal, the formation of the oxynitrides ABO_2N preserves the sum of the negative charges of the anions and in turn leaves the oxidation state of the B -type cation unchanged.

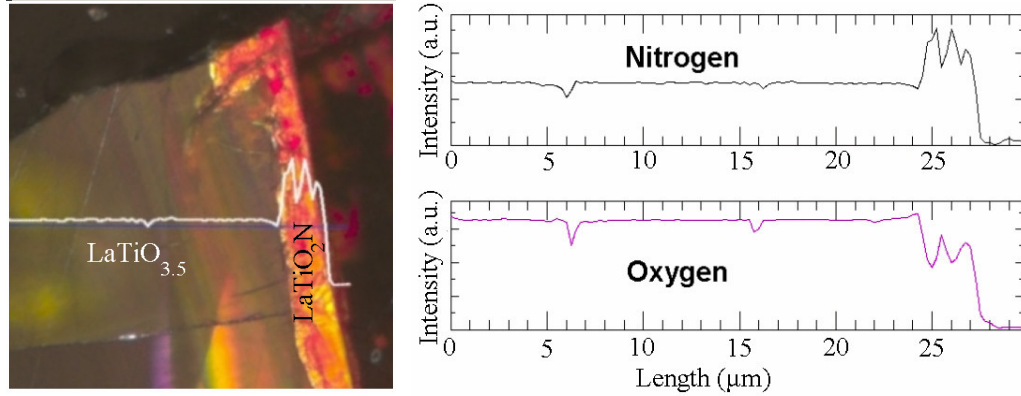


Figure 8.9: Optical photograph (left) and EPMA scans for oxygen and nitrogen (right) for $LaTiO_{3.5}$ crystal ammonolyzed during 18 h.

X-ray diffraction was carried out for all samples. As example, the θ/θ x-ray diffraction patterns of the nitrated $NdTiO_{3.5}$ and $SrTaO_{3.5}$ crystals are shown in Figure 8.10. XRD reveals the presence of both the oxynitride and the unreacted oxide in agreement with the SEM/EPMA results discussed above. As can be seen, for both the oxide and the oxynitride phase only specific sets of reflections were observed. This can easily be understood from the crystal structures. Although for all four compounds under investigation different space groups and cell parameters have been reported in the literature (see references in [8]), their idealized crystal structure can be derived from the cubic perovskite by using the relations:

$$\mathbf{a} = \mathbf{a}_p \quad \mathbf{b} = \mathbf{a}_p \cdot \sqrt{2} \quad \mathbf{c} = 2 \cdot s + n \cdot \mathbf{a}_p \cdot \sqrt{2} \quad (8.1)$$

Here, \mathbf{a}_p is the cubic perovskite unit cell length ($\approx 3.9 \text{ \AA}$), n reflects the number of perovskite slabs in each layer and $s \approx 2.3 \text{ \AA}$ is the distance between neighboring layers. Since $SrNbO_{3.5}$, $SrTaO_{3.5}$, $NdTiO_{3.5}$, and $LaTiO_{3.5}$ are all $n = 4$ members of the $A_nB_nO_{3n+2}$ family of [110]-perovskites (they are called like this because they can be derived by cutting the original cubic perovskite in the 110 direction), a \mathbf{c} axis of approximately 26.7 \AA results. The crystals cleave perpendicular to this long axis and therefore a crystal slice oriented horizontally on the sample holder only yields reflections with indices (00l) when measured on a powder x-ray

diffractometer. Furthermore, due to systematic extinctions only reflections with $l = 2n$ are observed (n describes an integer number and is not related to the n in $A_nB_nO_{3n+2}$).

For the $A_nB_nO_{3n+2}$ oxides the c axis is parallel to the $[110]$ -direction of the cubic perovskite structure of the formed oxynitrides. This structural relationship is shown in the right side of Figure 8.10. As a consequence of this topotactical relation only $\{hh0\}$ reflections of the oxynitride phase are found in the diffraction pattern. The absence of any reflections other than $\{hh0\}$ already is a clear indication for the formation of a (nearly) single crystalline surface layer with strict epitaxial orientation to the oxide crystals.

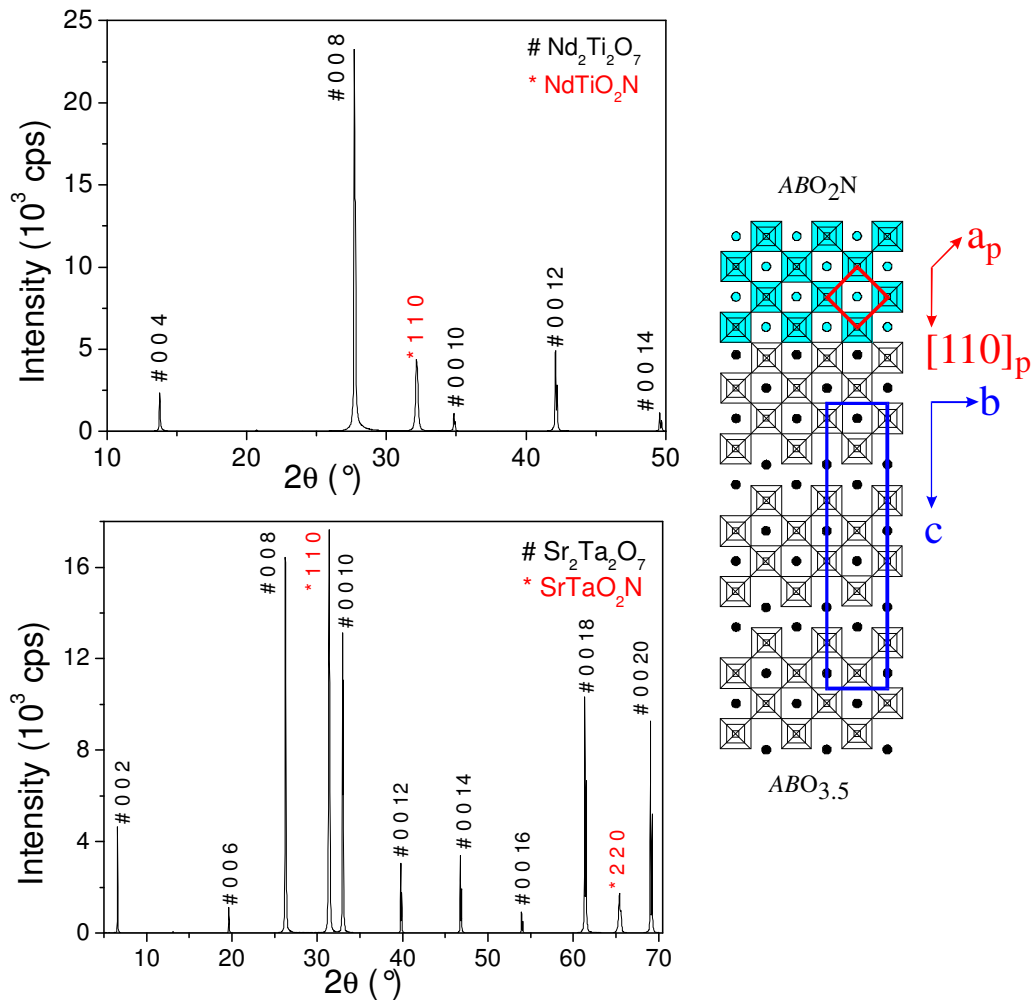


Figure 8.10: X-ray diffraction pattern of ammonolyzed $NdTiO_{3.5}$ and $SrTaO_{3.5}$ crystal slices. The right part illustrates the structural relation between the $ABO_{3.5}$ oxide educts and the oxynitride.

The orientational relation between the oxide crystal and the nitrated surface layer was examined in detail by pole figure measurements. Figure 8.11 depicts a {110} pole figure plot for SrTaO₂N. It consists of one peak at $\chi = 0^\circ$ and four peaks at $\chi = 60^\circ$, indicating that the oxynitride film contains only one texture component. The comparison with the in-plane orientation of the SrTaO_{3.5} substrate yields the full epitaxial relationship SrTaO₂N (110)[001] \parallel SrTaO_{3.5} (001)[100]. For this alignment the misfit in the SrTaO₂N [001] direction amounts only 2.3 %. The same epitaxial relationship was found for all compounds. The mosaic spread of the epitaxial oxynitride layer was determined by measurements of the rocking curve (ω scan) and azimuthal scans (φ scan) of the (110) reflections at $\chi = 0^\circ$ and $\chi = 60^\circ$, respectively. The mosaicity is a measure for the orientational distribution of the domains. For SrTaO₂N, a full width at half maximum (FWHM) of 0.37° for the ω scan and of 0.43° for the φ scan document a very good alignment of the oxynitride film both in polar and azimuthal direction.

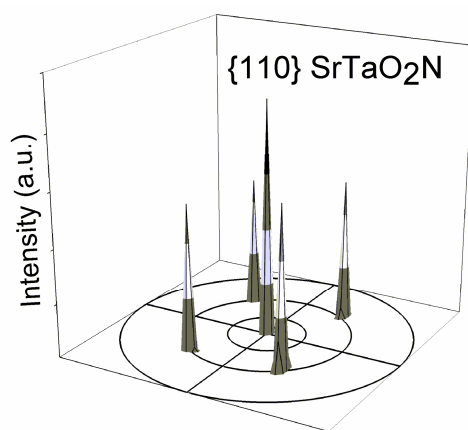


Figure 8.11: X-ray pole figure of the SrTaO₂N{110} reflections ($2\theta = 32.9^\circ$).

The mosaicity for SrNbO₂N was obtained for rocking curve with a FWHM of 1.44° and the φ scan of one of the (110) poles an azimuthal alignment of 1.04° . Very similar results were found for the ammonolyzed *Ln*TiO_{3.5} crystals. The ω scan of the (110) reflection ($\chi = 0^\circ$) and the φ scan of the (001) reflection ($\chi = 45^\circ$) yielded values for the polar and azimuthal mosaic spread of 1.80° and 1.41° for LaTiO₂N. The corresponding values for NdTiO₂N were determined to 0.34° and 0.36° . From these examinations it follows that the ammonolysis of oxide crystals can be used to synthesize (nearly) single-crystalline films of perovskite oxynitrides with a highly topotactical relation to the parent crystal substrate. It should be emphasized that the

described orientational relationship corresponds to the idealized structure for the oxides according to Equation 8.1 and the cubic perovskite structure for the oxynitrides. Possible small structural deviations were not considered. In fact, SrNbO_2N and SrTaO_2N crystallize in tetragonal space groups [9-13]. For LaTiO_2N a triclinic structure was reported [14], while an orthorhombic unit cell was found for NdTiO_2N [14]. These small structural distortions could not be detected in the pole figure measurements (i.e. no splitting of the peaks were observed) but may contribute to the slight peak broadening in the ω and φ scans.

The ammonolyzed crystals have additionally been analyzed by high-resolution transmission electron microscopy (HRTEM). As discussed before the $\text{ABO}_{3.5}$ oxides have a layered structure with $n = 4$ octahedra thick. The dimension of the unit cell in the c axis direction corresponds to 2 layers, each of 4 BO_6 -slabs (as schematized in Figure 8.10 right). In Figure 8.12 the layered structure is clearly visible for $\text{LaTiO}_{3.5}$.

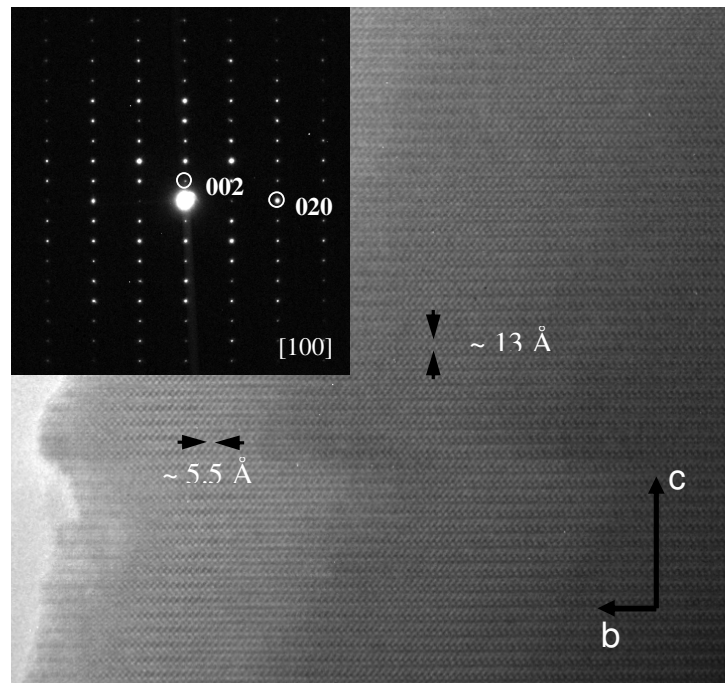


Figure 8.12: HRTEM and electron diffraction pattern of a $\text{LaTiO}_{3.5}$ single crystal.

It can be concluded that the horizontal thick light lines with 13 \AA spacing correspond to the 4-octahedra thick layers. The measured layer thickness is in good agreement with the expected value of $\frac{1}{2}c$. In the horizontal direction the distance between the planes is 5.5 \AA , which corresponds to the b axis. The inset in the figure is the diffraction pattern of $\text{LaTiO}_{3.5}$. The oxynitride part of the crystal has also been

analyzed. Its diffraction pattern is shown in Figure 8.13. It was indexed with $\bar{1}\bar{1}$ structure, $\mathbf{a} = 5.61 \text{ \AA}$, $\mathbf{b} = 7.87 \text{ \AA}$ and $\mathbf{c} = 5.58 \text{ \AA}$ [14]. The weak diffraction spots are due the super structure reflections.

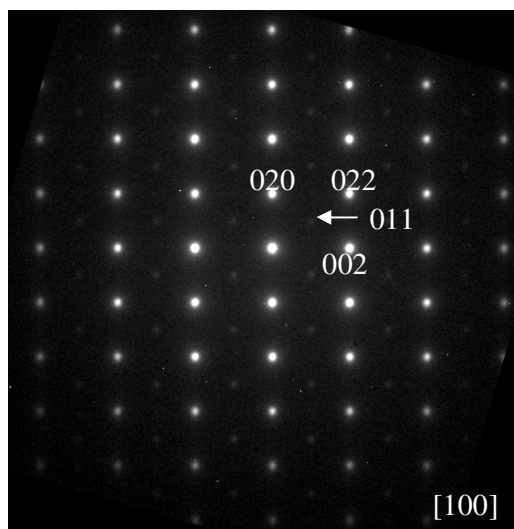


Figure 8.13: Diffraction pattern of LaTiO_2N single crystal.

The optical properties of the crystals were measured in transmission mode using UV-vis spectroscopy (chapter 2.4). Figure 8.14 gives the spectra of the oxynitrides in comparison to the corresponding oxides. $\text{LaTiO}_{3.5}$, $\text{SrNbO}_{3.5}$ and $\text{SrTaO}_{3.5}$ are transparent in the visible range and their absorption edge is in the UV region at ca. 350 nm. A very small shoulder at around 400 nm detected for $\text{LaTiO}_{3.5}$ is most likely due to a trace impurity of iron in the TiO_2 used as starting material and explains the very pale-brownish color of the grown crystals. In contrast, $\text{SrNbO}_{3.5}$ and $\text{SrTaO}_{3.5}$ show no absorption in this region and in turn the crystal slices appear completely colorless. The UV-vis spectrum of $\text{NdTiO}_{3.5}$ is rather complex due to the various transitions of the f-electrons. The material has an intense violet color, which after the ammonolysis turned into orange-brown. For the ammonolyzed crystals the onset of absorption is dramatically shifted to longer wavelengths (roughly 480-550 nm) and clear interference fringes can be observed. The oscillation widths and amplitudes of these fringes depend on the refractive indices of the oxynitrides and the corresponding oxides and the thickness of the reacted surface layer. Since these values differ for the various samples, the interference fringes show strong variations. From a plot of $((A - A_{\text{background}}) \times h\nu)^2$ versus $h\nu$ (A being the absorbance of the samples)

the following optical band gaps were derived: $\text{LaTiO}_{3.5}$ 3.6 eV, LaTiO_2N 2.2 eV, $\text{SrNbO}_{3.5}$ 3.9 eV, SrNbO_2N 2.1 eV, $\text{SrTaO}_{3.5}$ 4.1 eV and SrTaO_2N 2.3 eV. The obtained values are in good agreement with the band gap for the respective polycrystalline samples (chapter 7) [15, 16]. The uncertainty in these values is estimated to be 0.1-0.2 eV.

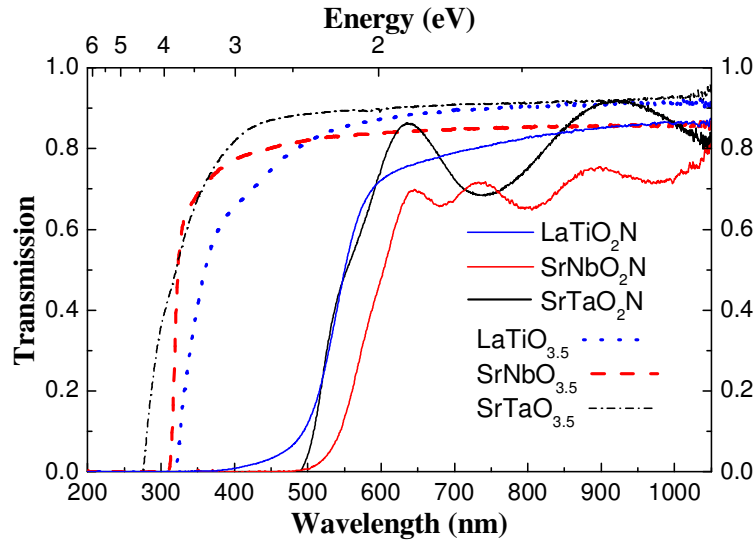


Figure 8.14: UV-vis spectra of LaTiO_2N , SrNbO_2N and SrTaO_2N in comparison to the unreacted oxides.

Electric conductivity measurements were performed on the $\text{ABO}_{3.5}$ single crystals before and after ammonolysis. The measurements were done in a coplanar configuration using a pseudo-four point measurement. The coplanar configuration was chosen instead of the “sandwich” one to minimize the influence of the oxide layer on the results of the electrical conductivity of the ammonolyzed samples. The electrical properties for $\text{SrNbO}_{3.5}$ before and after ammonolysis are shown in Figure 8.15. $\text{SrNbO}_{3.5}$ shows extremely low conductivity at room temperature (10^{-9} - $10^{-6} \Omega^{-1}\text{cm}^{-1}$, the values increased with increasing the applied frequency). $\text{SrNbO}_{3.5}$ can be classified as insulator material. A distinct anomaly is observed at ca. 100 K. It corresponds to a ferroelectric transition from a high temperature polarization in the **bc** plane to a polarization parallel to the [001], as reported in ref. [17, 18]. The electric properties of SrNbO_2N have not been reported before. The results of the electrical conductivity of SrNbO_2N are shown in Fig. 8.15(b). SrNbO_2N shows a semiconducting behavior, i.e. the conductivity increases with temperature. The conductivity of the ammonolyzed layer is around $4 \cdot 10^{-3} \Omega^{-1}\text{cm}^{-1}$ at room temperature.

This is 3-6 orders of magnitude higher than for the corresponding oxide. As discussed in Chapter 5, it is expected that the introduction of nitrogen in the oxide lattice results in a shrinking of the band gap and increases the electrical conductivity of the oxynitride sample.

A cross section SEM microscopy of the ammonolyzed $\text{SrNbO}_{3.5}$ crystal is shown in Figure 8.16. The crystal was imbedded in a polymeric resin to facilitate the polishing stage. A “sandwich” structure is clearly visible. The inner part of the crystal slice is brighter and corresponds to the oxide phase while the outer parts are the oxynitride composition. The thickness of the oxynitride layers are approximately 52 μm and 32 μm . Probably the thinner layer was in contact with the ceramic crucible during the ammonolysis. Comparing with $\text{LaTiO}_{3.5}$ (Figure 8.9) that was ammonolyzed for only 18 h and show a thickness of ca. 4 μm , it can be concluded that the higher the reaction time, the thicker the oxynitride layer became.

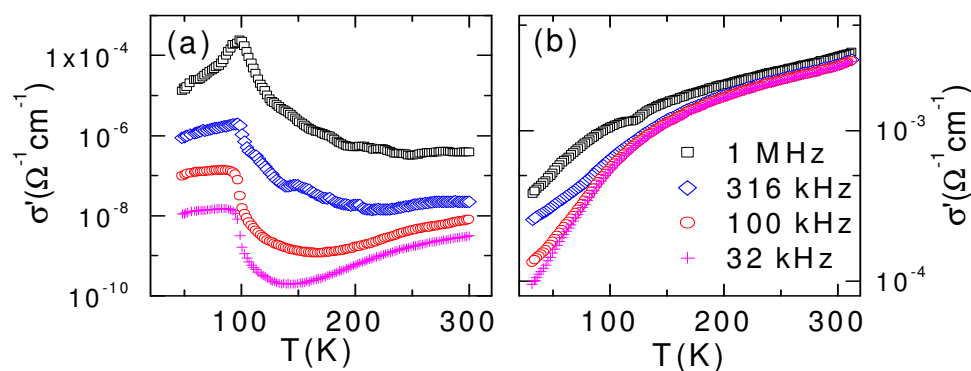


Figure 8.15: Electrical conductivity of the $\text{SrNbO}_{3.5}$ single crystal (a) before and (b) after ammonolysis at 950°C during 76 h.

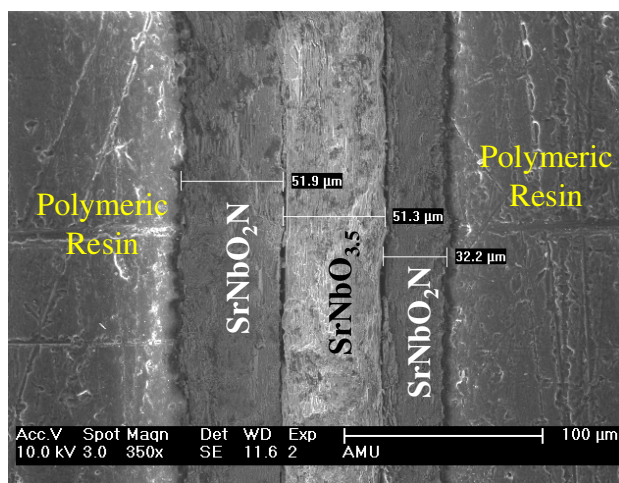


Figure 8.16: Cross section of the ammonolyzed (950°C - 76 h) $\text{SrNbO}_{3.5}$ crystal.

Figure 8.17(a) shows the electrical conductivity measurements for a crystal slice of SrTaO_{3.5}. Two electric anomalies can be observed, one between 78-95 K and the second at roughly 155 K. They are associated with ferroelectric phase transitions as reported in [19]. As for SrNbO₂N, the electrical properties of SrTaO₂N have not yet been published. SrTaO₂N also shows a semi conductor behavior and the electrical conductivity values increases up to 5 orders of magnitude compared to the non-ammonolysed crystal.

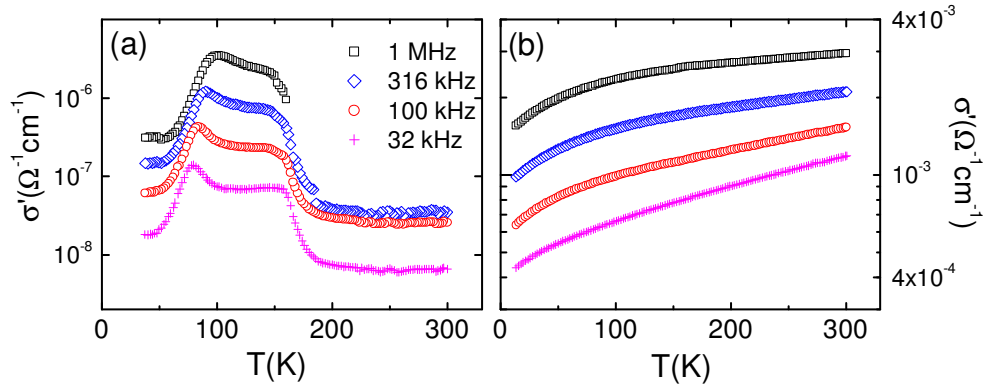


Figure 8.17: Electrical conductivity of a SrTaO_{3.5} single crystal (a) before and (b) after ammonolysis at 1050°C for 120 h. The thickness of the oxynitride layer is ca. 25 μm .

The electrical properties of LaTiO_{3.5} are plotted in Figure 8.18(a). No anomalies were found for LaTiO_{3.5}. Its electrical conductivity varies between 10^{-9} - 10^{-7} $\Omega^{-1}\text{cm}^{-1}$ at room temperature increasing with the applied frequency. As the other oxynitrides LaTiO₂N presents semiconducting behavior with electrical conductivity values in the order of 10^{-2} $\Omega^{-1}\text{cm}^{-1}$, e.g. at least 5 orders of magnitude higher than the respective oxide.

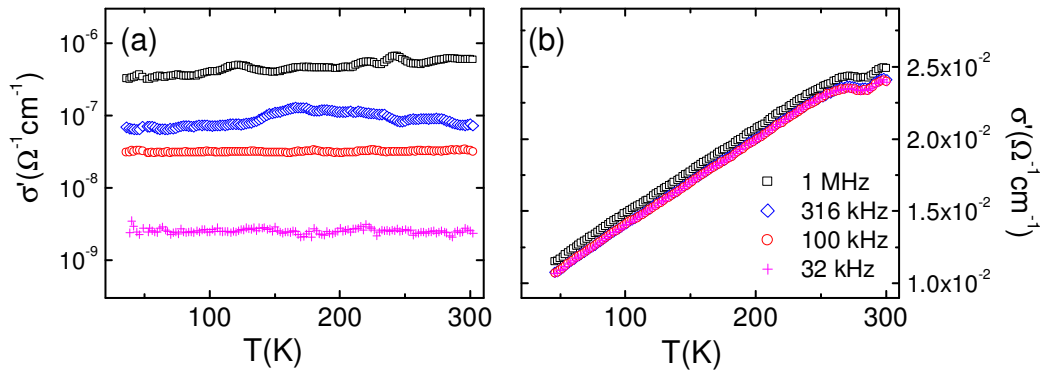


Figure 8.18: Electrical conductivity of a LaTiO_{3.5} single crystal (a) before and (b) after ammonolysis at 1050°C for 120 h. The thickness of the oxynitride layer is 25 μm .

It was not possible to clarify if the increasing of the electrical conductivity with frequency is an intrinsic property of the crystals or not. This shift could be due to hopping conductivity or due to a Maxwell-Wagner relaxation [20]. Studies using higher frequencies are currently performed to better explain the electrical properties of the oxynitride perovskites.

In summary, for many applications and/or investigations it would be desirable to have oxynitride single crystals. To the best of our knowledge, single crystals of oxynitride perovskites have not been synthesized yet. In this chapter we described a new complementary approach to obtain thicker oxynitride films of excellent crystallinity and epitaxial orientation. These films possess a very small mosaic spread, a fixed epitaxial relationship to the oxide material and are well suited for measurements of physical properties like optical absorption and electrical conductivity. The oxynitride thick layers showed colored surfaces with band gap around 2 eV and by several orders of magnitude higher electrical conductivity than the corresponding oxide.

References

- [1] Y. I. Kim, W. Si, P. M. Woodward, E. Sutter, S. Park, T. Vogt, *Chem. Mater.* 19 (2007) 618.
- [2] I. C. Lekshmi, A. Gayen, M. S. Hegde, *Mat. Res. Bull.* 40 (2005) 93.
- [3] L. Le Gendre, C. Le Paven, J. Pinel, D. Fasquelle, J. C. Carru, *Sil. Ind. Special Issue* 69 (2004) 165.
- [4] R. J. Cava, R. S. Roth, *J. Solid State Chem.* 36 (1981) 139.
- [5] R. Marchand, F. Pors, Y. Laurent, *Ann. Chim. Fr.* 16 (1991) 553.
- [6] T. A. Kurova, V. B. Aleksandrov, *Dokl. Akad. Nauk. SSSR* 201 (1971) 1095.
- [7] T. Williams, F. Lichtenberg, D. Widmer, J. G. Bednorz, A. Reller, *J. Solid State Chem.* 103 (1993) 375.
- [8] F. Lichtenberg, A. Herrnberger, K. Wiedenmann, J. Mannhart, *Prog. Solid State Chem.* 29 (2001) 1.
- [9] S. J. Clarke, K. A. Hardstone, C. W. Michie, M. J. Rosseinsky, *Chem. Mater.* 14 (2002) 2664.
- [10] Y.-I. Kim, P. M. Woodward, K. Z. Baba-Kishi, C. W. Tai, *Chem. Mater.* 16 (2004) 1267.
- [11] S. G. Ebbinghaus, A. Weidenkaff, A. Rachel, A. Reller, *Acta Crystallogr. C* 60 (2004) i91-i93.
- [12] F. Pors, P. Bacher, R. Marchand, Y. Laurent, G. Roullet, *Rev. Int. Hautes Tempér. Réfract.*, Fr. 24 (1988) 239.
- [13] E. Günther, R. Hagenmayer, M. Jansen, *Z. Anorg. Allg. Chem.* 626 (2000) 1519.
- [14] S. J. Clarke, B. P. Guinot, C. W. Michie, M. J. C. Calmont, M. J. Rosseinsky, *Chem. Mater.* 14 (2002) 288.
- [15] F. Cheviré, F. Tessier, R. Marchand, *Eur. J. Inorg. Chem.* 2006 (2006) 1223.
- [16] A. Kasahara, K. Nukumizu, G. Hitoki, T. Takata, J. N. Kondo, M. Hara, H. Kobayashi, K. Domen, *J. Phys. Chem. A* 106 (2002) 6750.

- [17] V. Bobnar, P. Lunkenheimer, J. Hemberger, A. Loidl, F. Lichtenberg, J. Mannhart, *Phys. Rev. B* 65 (2002) 155115-155115-8.
- [18] Y. Akishige, M. Kobayashi, K. Ohi, E. Sawaguchi, *J. Phys. Soc. Japan* 55 (1986) 2270.
- [19] Y. Akishige, K. Ohi, *J. Phys. Soc. Japan* 61 (1992) 1351.
- [20] A. K. Jonscher, *IEEE Elect. Inst. Magn.* 6 (1990) 16.

9. Summary and Outlook

Oxynitride perovskites with d^0 electronic configuration and compositional formula ABO_2N are an interesting class of materials. The introduction of nitrogen in the oxide lattice reduces the electronic band gap of the compounds. As a result the oxynitride perovskites show bright colors and have higher electrical conductivities than the respective colorless oxides. The oxynitrides were obtained from oxide precursors by ammonolysis. It was possible to synthesize oxide perovskite in different morphologies ranging from nanoparticles to single crystals of several mm^2 using a variety of synthesis methods such as solid state reaction, Pechini synthesis, spray pyrolysis, polyol assisted coprecipitation, spin coating, pulsed laser deposition and the floating zone technique. Afterwards, the $ABO_{3.5}$ or ABO_4 ($A = \text{Ca}^{2+}$, Ba^{2+} , Sr^{2+} , La^{3+} , Nd^{3+} and $B = \text{Ti}^{4+}$, Nb^{5+} , Ta^{5+}) perovskites were reacted with ammonia at high temperatures to partially substitute oxygen by nitrogen and form the respective ABO_2N oxynitrides. During this work a commercial (house) microwave adapted for ammonolysis of the oxide perovskite precursors was built up. Batches of 1g of single phase oxynitride perovskite could be prepared within 3 hours using the microwave induced ammonia plasma. Compared to a conventional (thermal) ammonolysis furnace the time of reaction is shorted by roughly a factor of 10. The energy and ammonia consumption is thus drastically reduced by using MIP, making this technique far more economic.

Depending on the desired application, the oxynitride samples should have specific morphological and physical properties, which can be achieved by choosing the properly synthesis method and by varying the cationic/anionic stoichiometry. As example, to be applied as pigments one of the requisites is that the color of the oxynitrides should be tailored to the desired shade. In this work it was demonstrated that varying the A and B cations in the ABO_2N structure results in controllable color changes. When an A cation is substituted by a smaller A' cation, e.g. Ba^{2+} (1.75 Å) by Ca^{2+} (1.48 Å), results in a less symmetric unit cell. BaTaO_2N is cubic while CaTaO_2N is orthorhombic. The unit cell distortion decreases the $B-(\text{O/N})-B$ bond angle and the overlap of the atomic orbitals results in a shrinking of the conduction band and consequently increases the band gap. As in the case of BaTaO_2N that is red (band gap of 1.8 eV) while CaTaO_2N is yellow (2.4 eV). On the other hand, when a B cation is

substituted by a more electronegative B' cation, e.g. Nb^{5+} (electronegativity equal to 0.57) by Ta^{5+} (0.61), the symmetry of the unit cell is not modified. CaNbO_2N and CaTaO_2N are both orthorhombic, but CaNbO_2N is ochre (band gap of 2.1 eV) and CaTaO_2N is yellow (2.4 eV). The band gap increasing is due the higher electronegativity of the B' cation, which shifts the conduction band to higher energetic position.

To be applied as pigments it is also required that the oxynitrides are stable at moderate temperatures, since normally they are submitted to heat treatments when incorporated in commodities. The thermal stability of the oxynitrides under different oxygen concentrations, namely between 0-20 %, was studied using thermogravimetry and mass spectrometry. All the studied samples were stable up to 400°C in air. Some samples preserved part of the oxynitride phase even after 30 min at 1200°C under argon atmosphere. During the heating treatment (e.g. waste combustion) the oxynitrides react to harmless indissoluble oxides and the evolved gas was mainly composed of N_2 . When high oxygen contraction was used only around 1% of the total evolved gases was composed of NO and/or NO_2 . The oxynitrides can therefore be considered as non-toxic not only during use but also in their disposal. For these reasons oxynitrides perovskites have good chances to be used as pigments in commodities submitted to intermediate temperatures and to substitute toxic pigments that contain heavy metals.

The oxynitride samples were investigated with respect to a possible photocatalytic activity. Because of their band gap values smaller than 3 eV, the oxynitrides use not only the UV light but also the less energetic visible part of the sun light in the catalytic reactions. Some of them were found to have considerable photocatalytic activities to decompose organic molecules and to form H_2 and O_2 from water solutions. Some ABO_2N compounds, such as LaTiO_2N , NdTaO_2N and CaNbO_2N , showed even better performance than TiO_2 nanoparticles (the most used photocatalyst nowadays) under visible light radiation. Another important characteristic for photocatalysts is a high surface of the particles, because with higher surface area the quantity of reaction sites to promote the redox reactions increases. This morphological requirement was achieved using polyol synthesis for the preparation of oxide precursors and ammonolyzing the samples at lower temperatures for shorter times. Furthermore a layered structure improves the photocatalysis because the interlayer spaces can act as reaction site and the electron-hole pair recombination

process is retarded by physical separation between the slabs. Adjusted nitrogen content is required for a high efficient photocatalyst, because the nitrogen quantity influences both band gap and crystalline structure. While nitrogen introduction decreases the band gap and the sample starts to absorb visible light, a high level of N-doping leads to a collapse of the layered structure. The band gap position of the sample is an extra requirement for water splitting. The bottom of the conduction band should be located more negative than the reduction potential of H^+ to H_2 (0 eV at pH = 0). In addition the top of the valence band should be more positive than the oxidation potential of H_2O to O_2 (1.23 eV at pH = 0). The band gap position of the oxynitride perovskites is not yet known. But the mismatch of the band gap of the oxynitrides could be an explanation for when only hydrogen or oxygen evolves during the photocatalysis measurements. During this work a new experimental set-up was built up for monitor the photocatalytic decomposition of acetone and the formation of the CO_2 and H_2O in real time. It was a quartz reactor built up inside the infrared device for in-situ photocatalysis measurements.

A structural study on the system $Sr_{(1-x)}La_xTi(O,N)_3$ using x-ray and neutron diffraction showed that the crystal structure become less symmetric with increasing La^{3+}/N^{3-} content. Starting with a cubic structure ($Pm\bar{3}m$) for $x = 0$, passing through tetragonal ($I4/mcm$) for $x = 0.25$ and orthorhombic ($Pnma$) for $x = 0.5$ and 0.75 . For the composition $x = 1$ two possible structures were found orthorhombic ($Pnma$) and triclinic ($I\bar{1}$). The $Sr_{(1-x)}La_xTi(O,N)_3$ oxynitrides were also grown as thin films using two different techniques, namely spin coating (SC) and pulsed laser deposition (PLD) of the oxide precursors and subsequently ammonolysis. The use of thin layers is indispensable for many technical applications as in electronics, optoelectronics and solar cells. The spin coated films showed porous layers of randomly oriented crystallites, what makes them suitable for catalytic applications. Another advantage of the spin coating method is that it can be used to cover large surfaces. It is also a cheap technique since water solutions are used. The films grown by PLD were found to be dense and well oriented. Their electrical conductivity was approximately two orders of magnitude higher than the films grown by spin coating, what makes them appropriate to be used in (optic) electronic devices.

Single crystals of $ABO_{3.5}$ were grown by the floating zone technique. The crystals were cleaved in thin slices of roughly 140 μm thickness and area of

several mm². These slices were reacted with NH₃ and thick single crystalline oxynitride layers were formed on the surface of the crystals. With increasing time of ammonolysis, thicker oxynitride layers were obtained. The electrical conductivities of the ammonolyzed slices were found to be around five orders of magnitude higher than the respective oxides. The single crystalline layers are useful for intrinsic physical properties measurements because the influence of non-inherent parameters as grain boundaries and pores can be eliminated.

This thesis shows several innovative studies in the oxynitride perovskite field. Synthesis techniques and measurement set-ups were developed/adapted to date poorly investigated materials. The investigations gave a better understanding of the physical properties of oxynitrides. It was demonstrated that the d⁰ oxynitride perovskites have a diversity of potential applications as pigments and photocatalytic dyes. They show a variety of colors and can be synthesized in very different morphologies. This work thus opens a variety of options for future investigations (some of them already in progress) in the synthesis and application of oxynitride perovskites.

Acknowledgements

I would like to thank all the people who helped me during my PhD:

Prof. Dr. Anke Weidenkaff, for finding me a suitable candidate for the PhD position at the SPP project and financing my interview trip from São Paulo to Zürich.

Prof. Dr. Armin Reller, for giving me the opportunity to work in his solid-state chemistry group, using the laboratory for my experiments. For his so good humor and for the organization (financial support too) of the group excursions and parties as in the Augsburger Christkindlesmarkt.

Prof. Dr. Stefan Ebbinghaus for supervising me during the PhD time. For giving me freedom to try out my ideas about the new experiments and buy the necessary chemicals and tools. For explaining me so many concepts and equations and correcting so patiently the papers, posters, abstracts, this thesis and my horrible English. Thank you, I am happy to have worked with you.

Dr. Rosa Robert for staying with me at HASYLAB and making the days there lighter. Thanks for your hospitality for the so many times that I have been in Zürich.

Dmitry Logvinovich for the discussions about our oxynitrides and the trying to work together.

Dr. Jan Hanss for helping with my computer problems and so many discussions. For showing me that nothing can be perfect there is always an error to be found out and fixed. You make me more self-confident. I should also thank you and your family for the great annually Asparagus evening.

Chem.-Ing. Andreas Kalytta with his two sentences: “You are always welcome” and “Du bist frech!” (I believe it was the first adjective that I have learned in German). I should also thank you for the German lessons: I have learned a lot of useless/meaningless words with you, as “türlich, Bielefeld, Unterhose für den Hals, Du Nase” usw. You have also helped me a lot to build up the experimental devices and in the discussions about my results.

Silke Weigel for the uncountable SEM pictures and for making my workdays funnier. It is good that Fr. Klottilde cannot tell anyone what we have talked about in our office ;-)

My university colleagues and professors from DEMa and LIEC/CMDMC, UFSCar, Brasil, for what I have learned during my graduation and master course.

Priv.-Doz. Dr. Helmut Karl (EPIV) for SIMS analyses and Priv.-Doz. Dr. Christof Schneider (EPVI) for electrical measurements of the thin films.

Dr. Andreas Heinrich and Dipl.-Phys. Timo Körner (EPIV) for the introduction to the PLD technique. Dr. Stefan Gsell (EPIV) for pole figures measurements.

Dr. Myriam Aguirre (EMPA) and M. Sc. Rosaria Brescia (EPIV) for the sample preparations, TEM pictures and phase analyses of the oxynitride single crystals.

M. Sc. Stefan Krohns and Stefan Konrad Kastner (EPV) for the electrical measurements of the single crystalline layers.

Prof. Dr. Kazunari Domen and Dr. Yungi Lee (University of Tokio, Japan) for the photocatalytic measurements (H_2 and O_2 evolution) on the oxynitrides.

Dipl.-Phys. Matthias Hörteis and Dr. Carolien Huisman for the work together on the photocatalysis set-up.

The Werkstatt people (particularly Andreas Sturm and the guy who loves Greece) for working patiently, always trying understand me with my mimics and for building up everything that I needed in reasonable time.

Dr. Javier García-García for the TEM investigations of the polyol samples.

All the “Praktikanten” that have worked with me, special thanks to Michael Weidl for building up the microwave set-up during his practical course.

The financial support from the German Research Foundation DFG within the programs SPP 1136 and SFB 484.

The extra people, who did not work with me, but have an enormous contribution to my PhD thesis:

Meus pais Demetrio e Regina, obrigada pelo amor incondicional de vocês, por ter me ensinado a ter caráter e a respeitar o próximo. Aos meus irmãos Pedro Vitor e Juliana, pela nossa amizade e preocupação mútua. E depois que vim pra Alemanha apareceram duas novas pessoinhas na família Arthur e Gabriela Vitória, vocês renovaram as esperanças! Amo a nossa família.

As minhas amigas augsburgerinnen-brasileiras Lucila, Adriane, Marlice, Patrícia, Nádia, Severina, Solange, Paula e Marival. Obrigada por mostrar coragem e garra, pelo apoio, por fazer da gelada Alemanha um pedacinho do Brasil. Com vocês

aprendi a ser forte e o mais importante sempre ter os braços abertos e um sorriso no rosto.

My foreigner friends Rosaria, Alicia, Pepe and Neus, Giorgos, Cristina and Ivan, Florence, Ali, Mario, Felix, Isabelle and Olivier.

Molta Grazie. Avete messo il colore in mia Germania grigia.

Muchas Gracias. Usted puso color en mi Alemania gris.

Σας ευχαριστούμε. Βάζετε το χρώμα στην γκρίζα Γερμανία μου.

Merci beaucoup. Vous avez mis la couleur en ma Allemagne grise.

Meinen deutschen freuden Oliver, Sabine und Jacob, Melani und Frank, Stuff, Marie, Katrin und Christof. Vielen Dank für die vielen gemeinsamen Abendessen und für die informellen deutschkurse. Es war eine schöne Zeit zusammen mit Euch.

Eduardo Jian Hua Lee por tudo que passamos juntos, por toda a sua dedicação, sempre te amarei.

List of Publications

- Aguiar R., Kalytta A., Weidenkaff A., Reller A. and Ebbinghaus S. G.,
“*Photocatalytic decomposition of acetone using LaTi(O,N)₃ nanoparticles under visible light radiation*”
J. Mater. Chem. 18 (2008) 4260-4265.
- Aguiar R., Logvinovich D., Weidenkaff A., Reller A. and Ebbinghaus S. G.,
“*Thermal oxidation of oxynitride perovskites in different atmospheres*”
Thermochim. Acta 471 (2008) 55-60.
- Aguiar R., Logvinovich D., Weidenkaff A., Raquel A., Reller A. and Ebbinghaus S. G.,
“*The vast colour spectrum of ternary metal oxynitride pigments*”
Dyes Pigm. 76 (2008) 70-75.
- Aguiar R., Logvinovich D., Weidenkaff A., Helmut K., Schneider C. W., Reller A. and Ebbinghaus S. G.,
“*Physical properties of (La,Sr)Ti(O,N)₃ thin films grown by pulsed laser deposition*”
Mat. Res. Bull. 43 (2008) 1376-1383.
- Ebbinghaus S. G., Aguiar R., Weidenkaff A., Gsell S. and Reller A.,
“*Topotactical growth of thick perovskite oxynitride layers by ammonolysis of single crystalline oxides*”
Solid State Sci. 10 (2008) 709-716.
- Aguiar R., Lee Y., Domen K., Kalytta A., Logvinovich D., Weidenkaff A., Reller A. and Ebbinghaus S. G.,
“*Advances in oxynitride perovskites: synthesis and photocatalytic applications*”
Book chapter in Ceramic Materials Research Trends (2007) 111-137. (Nova Science Publishers, Inc. ISBN-13: 978-1-60021-769-2).

- Aguiar R., Weidenkaff A., Schneider C. W., Reller A. and Ebbinghaus S. G.,
“Syntheses and properties of oxynitrides (La,Sr)Ti(O,N)₃ thin films”
Prog. Solid State Chem. 35 (2007) 291-298.
- Logvinovich D., Aguiar R., Robert R., Trottmann M., Ebbinghaus S. G.,
Reller A. and Weidenkaff A.,
“Synthesis, Mo-valence state, thermal stability and thermoelectric properties
of SrMoO_{3-x}N_x (x>1) oxynitride perovskites”
J. Solid State Chem. 180 (2007) 2649-2654.
- Logvinovich D., Aguirre M. H., Hejtmanek J., Aguiar R., Ebbinghaus S. G.,
Reller A. and Weidenkaff A.,
“Phase formation, structural and microstructural characterization of novel
oxynitride-perovskites synthesized by thermal ammonolysis of (Ca,Ba)MoO₄
and (Ca,Ba)MoO₃”
J. Solid State Chem. 181 (2008) 2243-2249.
- Orlandi M. O., Leite E. R., Aguiar R., Bettini J. and Longo E.,
“Growth of SnO nanobelts and dendrites by a self-catalytic VLS process”
J. Phys. Chem. B 110 (2006) 6621-6625.
- Godinho M. Jr., Longo E., Leite E. R. and Aguiar R.,
“In-situ observation of glass particles sintering”
J. Chem. Educ. 83 (2006) 410-413.
- Orlandi M. O., Aguiar R., Lanfredi A.J.C., Longo E., Varela J. A., Leite E. R.,
“Tin-doped indium oxide nanobelts grown by carbothermal reduction
method”
Appl. Phys. A 80 (2005) 23-25.
- Ribeiro C., Lee E. J. H., Giraldo T. R., Aguiar R., Longo E., Leite E. R.,
“In situ oriented crystal growth in a ceramic nanostructured system”
J. Appl. Phys. 97 (2005) 024313.

- Aguiar R., Leite E. R., Longo E., Mauricio M. R. D.,
“Development of a Sb₂O₃-doped SnO₂ conductor pigment and its applications in semiconductor glazes”
 Ceramica 50 (2004) 134-137.
- Orlandi M. O., Aguiar R., Leite E. R., Longo E. and Varela J. A.,
“Tin oxide nanobelts: oxidation state control by the synthesis atmosphere”
 Ceramica 50 (2004) 58-61.
- Leite E. R., Pontes F. M., Lee E. J. H., Aguiar R., Longo E., Pontes, D. S. L.,
 Nunes M. S. J., Macedo H. R., Pizani P. S., Lanciotti F., Boschi T. M., Varela
 J. A. and Paskocimas C. A., Pinheiro C.D., Taft C. A.,
*“An investigation of metal oxides which are photoluminescent at room
 temperature”*
 J. Mol. Struct. (Theochem) 668 (2004) 87-91.
- Bouquet V., Vasconcelos N. S. L. S., Aguiar R., Pinheiro C. D., Leite E. R.,
 Pizani P. S., Varela J. A., Longo E., Boschi T. M., Lanciotti F., Machado M.
 A. C.,
“Ferroelectric materials with photoluminescent properties”
 Ferroelectrics 288 (2003) 315-326.
- Leite E. R., Pontes F. M., Lee E. J. H., Aguiar R., Longo E., Pontes, D. S. L.,
 Nunes M. S. J., Macedo H. R., Pizani P. S., Lanciotti F., Boschi T. M., Varela
 J. A. and Paskocimas C. A.,
“A novel approach for the development of photoluminescent material”
 Appl. Phys. A 74 (2002) 529-532.

Curriculum Vitae

Name: Rosiana Aguiar

Date of birth: 18th March 1980

Place of birth: Caceres, MT - Brazil

Nationality: Brazilian

Education

02/1995-12/1997 High School EPSG Prof. Gumercindo Corrêa de Almeida Moraes
Dracena-SP, Brazil

03/1998-02/2003 **Bachelor in Materials Engineering**
Materials Engineering Department
Universidade Federal de São Carlos – Brazil

03/2003-10/2004 **Master in Materials Science and Engineering**
Thesis: “Synthesis and Characterization of Tin Oxide Nanoribbons”
Advisor: Prof. Dr. Edson Roberto Leite
Materials Engineering Department
Universidade Federal de São Carlos – Brazil

11/2004-11/2008 **PhD in Materials Science**
Thesis: “Synthesis and Properties of Oxynitride Perovskites”
Advisors: Prof. Dr. Armin Reller and Prof. Dr. Stefan G. Ebbinghaus
Solid State Chemistry Laboratory, Physics Department
Universität Augsburg – Germany